Electroweak Baryogenesis with BARYONET: a self-contained review of the WKB approach

Do Not Get Lost: A Survival Guide

Giulio Barni¹

Instituto de Física Teórica IFT-UAM/CSIC, Cantoblanco, E-28049, Madrid, Spain October 28, 2025

Abstract

We present a comprehensive, self-contained pedagogical computation of the baryon asymmetry of the Universe within electroweak baryogenesis (EWBG), from the derivation of the semiclassical, CP-dependent force to the formulation and solution of the transport equations obtained from the Boltzmann equations—all implemented in the open-source code BARYONET². Our analysis follows the semiclassical WKB approach, where spatially varying complex masses across expanding bubble walls feel CP-violating forces that bias plasma transport. Starting from the stationary Boltzmann equation in the wall frame and projecting onto a hierarchy of velocity moments, we derive a compact, fluid-like system of coupled differential equations for chemical potentials and velocity perturbations. After obtaining the solutions, one can define the left-handed baryon chemical potential, which acts as the source term for the weak sphalerons. These processes generate the baryon asymmetry in front of the wall, which is subsequently frozen once it passes through it.

We validate the framework against established formalisms and provide benchmarks in representative scenarios, including singlet extensions of the Standard Model, two-Higgs-doublet models, and Higgs- ϕ^6 constructions. The resulting BARYONET implementation delivers an automated, reproducible pipeline for WKB-based baryogenesis studies, connecting formal derivations with phenomenological applications.

In parallel, we revisit standard EWBG ingredients—diffusion constants, Yukawa/helicity-flip rates, and strong/weak sphaleron rates—to clarify conventions, update numerical inputs, and present a pedagogical derivation, ensuring transparent reproducibility.



¹giulio.barni@ift.csic.es

²electroweak BARYOgenesis with Numerical Evaluation of the Transport equations.

Contents

1	Introduction	2			
2	WKB formalism 2.1 Setup and assumptions	4 5 6 7			
3	3.4 CP projection and identification of sources	$egin{array}{c} 8 \\ 8 \\ 8 \\ 10 \\ 10 \\ 12 \\ 13 \\ 14 \\ 15 \\ 16 \\ 18 \\ 19 \\ \end{array}$			
4		1 9 20			
5	5.1 Weak sphaleron rate profile	21 23 24 25			
6	6.1 Code structure	25 27 27			
7	7.1 ModelIndependent	28 28 29 30 33			
8	Higher-moment analysis	34			
9	Conclusions and outlook	37			
A	Universal kernel 3 A.1 Master integral and choices of V 3				
В	B.1 Linearised out-of-equilibrium contributions	41 42 43			

\mathbf{C}	Diffusion constants	43
	C.1 Expression for the diffusion constants	44
	C.2 Diffusion constant of the Higgs field: D_h	
D	Yukawa-mediated relaxation rates: $\widehat{\Gamma}_y$	50
	D.1 Reconciliation with the literature for $\widehat{\Gamma}_y$	53
${f E}$	Yukawa helicity flipping rate: $\widehat{\Gamma}_M$	5 4
	E.1 Fermionic case for $\widehat{\Gamma}_m^q$	54
	E.2 Reconciliation with the literature for $\widehat{\Gamma}_M$	56
	E.3 Bosonic case for $\widehat{\Gamma}_M^{(h)}$	56
\mathbf{F}	Weak and Strong Sphaleron rates	5 8
	F.1 Reconciliation with the literature for Γ_{ss}	58
	F.2 Reconciliation with the literature for Γ_{ws}	
\mathbf{G}	Numerical Implementation of the Fluid Equations	5 9
	G.1 The role of Lagrange Multipliers	60
н	Chemical vs. kinetic equilibrium	60
	H.1 From cosmology to EWBG timescales	61

1 Introduction

Electroweak baryogenesis (EWBG) is an appealing, testable explanation for the origin of the cosmic matter–antimatter asymmetry at the weak scale. In its modern form it realizes Sakharov's three conditions—baryon number violation, C and CP violation, and departure from equilibrium—within a hot, expanding plasma undergoing the electroweak phase transition (EWPT): anomalous sphaleron transitions violate B, CP–violating interactions bias particle–antiparticle transport across the bubble wall, and the out–of–equilibrium environment provided by a first–order phase transition (FOPT) allows the bias to be converted into net baryon number and subsequently preserved inside the broken phase [1-6].

The Standard Model (SM) by itself falls short on both dynamical fronts. Lattice and perturbative studies show that for $m_h \simeq 125$ GeV the EW symmetry breaking proceed through a smooth crossover rather than first order [7–13], precluding efficient departure from equilibrium; moreover, Cabibbo-Kobayashi–Maskawa CP violation yields sources many orders of magnitude too small to explain the observed baryon asymmetry [14–16]. These facts motivate extensions of the SM that (i) strengthen the EWPT to a FOPT and (ii) supply additional CP–violating phases compatible with laboratory bounds. Representative possibilities include singlet extensions of the Higgs sector, two–Higgs–doublet models (2HDMs), supersymmetric and composite frameworks, and effective descriptions with higher–dimensional operators, dynamical Yukawa values across the phase transition; each provides concrete wall profiles (masses and phases) and interaction rates that feed the transport network [17–22].

From the theory side, two complementary approaches underlie contemporary EWBG computations. One is the real-time Schwinger-Keldysh (Kadanoff-Baym) formalism, from which quantum kinetic equations are derived and then expanded in gradients to obtain semiclassical dispersion relations, force terms, and collision integrals for out-of-equilibrium distribution functions [23–28]. The other is the Wentzel-Kramers-Brillouin(WKB)/semiclassical method, well suited to "thick" walls, in which CP-odd corrections to single-particle dispersion relations generate opposite forces on particles and antiparticles crossing the wall; these forces seed left-handed charge in front of the wall that weak sphalerons partially convert into baryon number [29–34]. Careful comparisons have clarified the correspondence between the two pictures at the level of observable sources, the role of elastic (W) scatterings, and the structure of the fluid closure used to reduce the kinetic equations to a tractable diffusion network [35–42].

Across models, the phenomenological pipeline has crystallised into a sequence of decidedly nontrivial steps. First, one determines the finite-temperature effective potential and constructs—analytically or parametrically—the bubble—wall profiles for the relevant fields. On this foundation, one derives the CP-even and CP-odd sources together with the linearised collision integrals in a boosted, near-equilibrium plasma. The next stage—often the numerically dominant challenge, amounting to a stiff, multiscale boundary-value problem—is to solve the coupled fluid/transport system. Finally, the resulting left-handed baryon chemical potential must be folded with the weak-sphaleron profile to predict the frozen-in asymmetry η_B [29–31, 34, 43–51].

What this review provides. Despite many excellent reviews of EWBG over the past decades [52–60], including very recent overviews [61] (to which we refer for a complete list of references), a practical gap persists: a public, end-to-end, reproducible implementation that unifies transport formalisms and conventions across the literature in the semiclassical approach. This work closes that gap by offering a self-contained account of the semiclassical transport approach and, crucially, by packaging it into a single framework. We assemble the standard ingredients—WKB kinematics, the Liouville operator in the wall frame, CP projection, a controlled moment expansion, and a model-independent closure of collision terms—into a compact fluid network written in terms of dimensionless thermal kernels, cleanly factorised from model inputs. We also provide an operational, precise definition of the left-baryon chemical potential μ_{B_L} that sources weak sphalerons, together with the exact integrating-factor expression used to compute η_B .

Alongside the narrative review, we release BARYONET, an open and modular Python code that delivers a reproducible pipeline from model to η_B : it ingests wall profiles (masses, phases, and their derivatives), assembles the transport system in multiple established frameworks, solves the linear boundary-value problem, and outputs η_B with figure scripts and tests. In contrast to recent reviews that summarise formal developments but do not provide a unified, maintained reference implementation or cross-validated pipeline, our package offers a single workflow with benchmark overlays and documented choices (diffusion sets, thermal masses, sphaleron rates), enabling direct comparison across frameworks. The code and examples are available at github.com/GiulioBarni/BARYONETv1.

Scope and organisation. Section 2 develops the semiclassical (WKB) framework: we set up the background, derive the dispersion relations and group velocities, and obtain the CP-odd semiclassical force. Section 3 builds the stationary Boltzmann equation in the wall frame, performs the CP decomposition and the moment expansion, and introduces the universal thermal kernels together with a model-independent closure of collision terms. Section 4 then specifies the minimal matter content commonly used in EWBG, writes the full fluid network explicitly, and defines the left-baryon chemical potential that sources weak sphalerons. Section 5 derives the weak-sphaleron evolution equation for $n_B(z)$ and the resulting baryon asymmetry η_B . Section 6 outlines the symbolic-to-numeric pipeline implemented in BARYONET and summarises the numerical inputs used for validation, providing updated values recommended by this work. Section 7 presents results and comparisons across representative scenarios (a model-independent benchmark, real-singlet extensions, a Higgs- ϕ^6 setup, and the 2HDM), highlighting agreements and residuals with previous studies. Finally, Section 8 examines the fluid network with an arbitrary number of perturbation modes and highlights the convergence of the moment expansion; we conclude in Section 9 with an outlook on theoretical refinements and planned updates to the code.

Notation for frameworks. Throughout the review, we use the shorthand **FH04** [44], **FH06** [45], **CK** [49], and **KV24** [51] to denote our implementation of the fluid networks as defined in the cited papers. When we say "FH04/FH06/CK/KV24" below, we refer to those concrete implementations (species content, moment structure, and collision closure) as summarised in Table 1.

Additional conventions. Unless stated otherwise, we work in the wall frame. Spatially, the broken phase $(\langle h \rangle \neq 0)$ is on the left and the symmetric EW phase on the right; i.e. z < 0 is broken and z > 0 is symmetric. In the plasma frame, the bubble wall moves to the right (positive z) with velocity v_w ; equivalently, in the wall frame, the plasma and particle flux drift to the left (negative z). The symbol q_3 denotes the third–generation left–handed quark doublet, t_R the right–handed top, and h the Higgs. By "perturbations" we mean velocity moments in the fluid description: chemical potentials

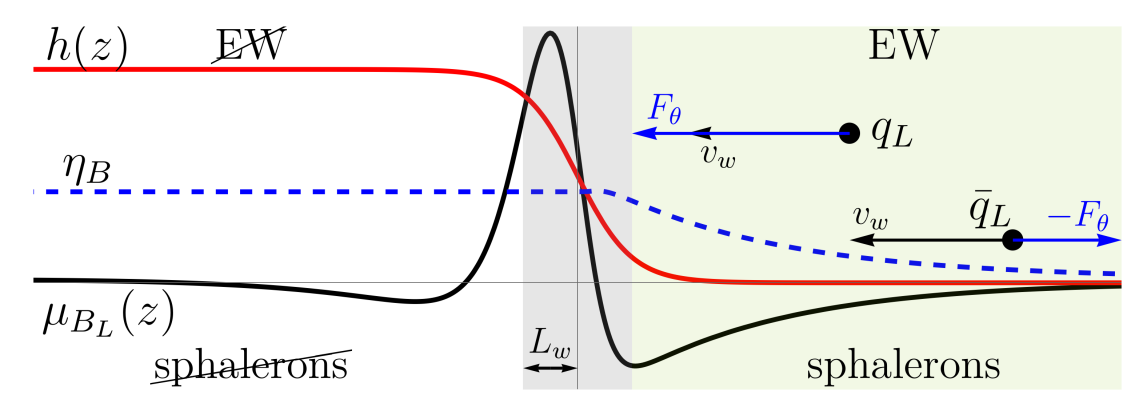


Figure 1: Schematic illustration of EWBG transport across a planar bubble wall. The red curve is the Higgs background h(z), interpolating from the broken phase (left, $\langle h \rangle \neq 0$) to the symmetric EW phase (right, $\langle h \rangle = 0$). The shaded strip marks the wall of width $\pm L_w$; the particles in the wall frame are moving with velocity v_w to the left. CP-violating semiclassical forces F_θ (blue arrows) act with opposite sign on particles and antiparticles, biasing left-handed quarks q_L and antiquarks \bar{q}_L . This generates a left-baryon chemical potential $\mu_{B_L}(z)$ (black), peaked near the wall, which diffuses into the symmetric phase where weak sphalerons are active (grey + green region) and is converted into baryon number. The resulting baryon density η_B (blue dashed) accumulates ahead of the wall and is preserved once the wall passes and sphalerons are quenched in the broken phase. Curves are illustrative and not to scale.

Scheme	Tracked species	Velocity range	Closure	$N_{ m PERT,max}$
FH04 [44]	q_3, t^c	$low-v_w$	constant $R = -v_w$	2
FH06 [45]	t, b, t^c, h +W scattering	$low-v_w$	constant $R = -v_w$	2
CK [49]	t_L, b_L, t_R, h +W scattering	$high-v_w$	constant $R = -v_w$	2
KV24 [51]	t_L, b_L, t_R, h +W scattering +better treatment of the rates	$\mathrm{high}{-v_w}$	constant $R = -v_w$ or variance	≤ 50

Table 1: Summary of the frameworks used as *notation* in this review. The first column lists the frameworks and their original paper. The second column indicates which species is tracked in that implementation. The third column states the range of velocity that is suited for that implementation. The last column gives the maximum number of perturbations (chemical potential + velocity perturbation) retained per species.

 μ_i are always included, while $u_i^{(\ell+1)}$ with $\ell=0,1,\ldots,N_{\text{PERT,max}}-1$ are the retained velocity modes $(N_{\text{PERT,max}}=2\text{ corresponds to }\mu_i\text{ plus a single velocity mode }u_i^{(1)})$. Differences due to diffusion sets, thermal mass choices, and sphaleron profiling are called out explicitly when relevant.

Blue boxes offer concise, pedagogical clarifications of technical points encountered in this review; expert readers may safely skip them without loss of continuity.

2 WKB formalism

In this section, we review the WKB (semiclassical) treatment of a Dirac fermion that crosses a planar bubble wall with a space—dependent complex mass. The guiding idea of WKB is that when the background varies slowly on the scale of the particle's de-Broglie wavelength, the evolution can be organised as an expansion in spatial gradients of the background. One writes the spinor as a locally plane—wave state with a slowly varying amplitude and solves the Dirac equation order by order in

derivatives of the background. At leading order, one recovers a local dispersion relation; at the next orders, one obtains transport equations and small CP-odd shifts that encode how the slowly varying complex phase of the mass biases particle and antiparticle propagation. This is the mechanism behind the semiclassical force used in electroweak baryogenesis, as schematically shown in Fig. 1.

Here, by "background fields" we specifically mean the classical scalar profile across the wall that sources the fermion's complex mass. In practice, the space dependence of the mass is entirely inherited from this scalar background, so it is convenient to phrase the WKB expansion in terms of the slowly varying quantities m(z) and $\theta(z)$ that are proportional to the scalar profile. In what follows, whenever we refer to expanding in the background, we will do so by expanding in spatial gradients and in the slowly varying amplitudes m and θ themselves, which faithfully capture the influence of the scalar background on the fermion dynamics.

We work in the wall rest frame and model the wall as static and planar, with normal along the z-axis. The fermion mass is taken to be

$$m(z) = |m(z)| e^{i\theta(z)}, \qquad (1)$$

so that the only space dependence enters through the modulus |m| and the CP-violating (CPV) phase θ . The calculation is organised as a controlled gradient expansion in $\partial_z |m|$ and $\partial_z \theta$, valid when the wall is thick compared to microscopic wavelengths (equivalently, when $EL_w \gg 1$ for the modes that dominate transport). Unless explicitly stated otherwise, primes denote derivatives with respect to the wall coordinate, $X' \equiv \partial_z X$. All subsequent formulae and checks will be presented for this simple but paradigmatic example, which captures the essential physics of a slowly varying CP-violating background across the bubble wall.

2.1 Setup and assumptions

We consider a single Dirac fermion with a spatially varying complex mass

$$(i\gamma^{\mu}\partial_{\mu} - m P_R - m^*P_L)\psi = 0, \qquad m(z) = |m(z)| e^{i\theta(z)}, \qquad P_{R,L} = \frac{1}{2}(1 \pm \gamma^5).$$
 (2)

We work in the wall frame and, just for simplicity, set the momentum parallel to the wall to zero initially $(p_x = p_y = 0)$, transverse momenta will be reintroduced later. The spin of the fermion is taken along z, $\sigma_3 \chi_s = s \chi_s$, with χ_s the spin eigenstates and $s = \pm 1$ related to helicity by $s = \lambda \operatorname{sign}(p_z)$. We assume a slowly varying background (sometimes called adiabaticity condition)

$$\frac{|m|'}{E^2} \ll 1, \qquad \frac{|\theta'|}{E} \ll 1, \qquad \text{and similarly for higher derivatives,}$$
 (3)

so that a gradient expansion is justified. We emphasise that primes denote spatial derivatives, which therefore carry dimensions of energy. Looking for positive—energy solutions with plane—wave time dependence, we write

$$\Psi_s(t,z) = e^{-iEt} \begin{pmatrix} L_s(z) \\ R_s(z) \end{pmatrix} \otimes \chi_s, \tag{4}$$

which reduces the Dirac equation to

$$(E - is \,\partial_z)L_s = m \,R_s,\tag{5}$$

$$(E + is \,\partial_z)R_s = m^* \,L_s. \tag{6}$$

Eliminating R_s yields a second-order equation for L_s ,

$$\left[(E + is \,\partial_z) \frac{1}{m} (E - is \,\partial_z) - m^* \right] L_s = 0.$$
 (7)

To organise the gradient expansion, we adopt the WKB ansatz

$$L_s(z) = w(z) \exp\left\{i \int^z p_{cz}(z') dz'\right\},\tag{8}$$

Box 2.1: Canonical vs. kinetic momentum

In the WKB/Hamilton–Jacobi picture one writes S(z) so that $\psi \sim a(z) e^{iS(z)}$ and the canonical momentum is $p_{cz} \equiv \partial_z S$. A local phase redefinition $\psi \to e^{i\alpha(z)}\psi$ is a canonical transformation on phase space: it preserves the equations of motion but shifts the canonical coordinate,

$$p_{cz} \rightarrow p_{cz} + \alpha'(z)$$
.

Thus p_{cz} is gauge-/phase-convention dependent.

Physical momentum. Observables must be invariant under canonical rephasings. This selects the *kinetic* momentum

$$p_z \equiv p_{cz} - \alpha'(z),$$

which controls the group velocity, semiclassical force, and enters the Liouville/Boltzmann transport equations. In short: use p_z for dynamics; p_{cz} is a convenient phase-space coordinate. First-order gradient form. In our setup, the phase α includes the CP phase redefinition. To $\mathcal{O}(\partial_z)$, the explicit relation used in the text reads

$$p_z = (p_{cz} - \alpha'_{\rm CP}) \left(1 - s_{\rm CP} s \frac{\theta'}{2E_{0z}}\right),$$

i.e. the pure-gauge subtraction $-\alpha'_{CP}$ plus the standard $\mathcal{O}(\theta')$ misalignment between phase and group propagation.

with slowly varying amplitude w and canonical momentum p_{cz} . Separating real and imaginary parts of Eq. (4), one finds

$$E^{2} - |m|^{2} - p_{cz}^{2} + (sE + p_{cz})\theta' - \frac{|m|'}{|m|}\frac{w'}{w} + \frac{w''}{w} = 0,$$
(9)

$$2p_{cz} w' + p'_{cz} w - \frac{|m|'}{|m|} (sE + p_{cz}) w - \theta' w' = 0.$$
(10)

At zeroth order (dropping gradients) Eq. (9) reproduces the usual dispersion relation,

$$E^2 = p_{cz}^2 + |m|^2. (11)$$

Power counting. We count $\partial_z \sim \mathcal{O}(\epsilon)$, so |m'|, $\theta' \sim \mathcal{O}(\epsilon)$, $w'/w \sim \mathcal{O}(\epsilon)$ and $w''/w \sim \mathcal{O}(\epsilon^2)$. When deriving first-order kinematics, we will consistently drop $\mathcal{O}(\epsilon^2)$ terms like w''/w.

2.2 First-order solution for the canonical momentum

Solving Eq. (9) to first order and using $p_0 \equiv \text{sign}(p_{cz})\sqrt{E^2 - |m|^2}$ from (11), one finds

$$p_{cz} = p_0 + s_{CP} \frac{sE + p_0}{2p_0} \theta' + \alpha', \qquad s_{CP} = \begin{cases} +1 & \text{(particle)} \\ -1 & \text{(antiparticle)} \end{cases}, \tag{12}$$

where $s_{CP} = \pm 1$ labels the two CP-conjugate WKB branches. Under a CP transformation the complex mass phase flips, $\theta \to -\theta$, which maps the $s_{CP} = +1$ branch into the $s_{CP} = -1$ one. It is therefore convenient to keep a fixed phase profile $\theta(z)$ and encode the CP operation entirely through s_{CP} . The additional term $\alpha'(z)$ denotes an arbitrary local rephasing of the spinor field³, and represents a pure gauge contribution to the canonical longitudinal momentum⁴. With this convention, we will always refer to a phase $\theta(z)$ of definite sign and track CPV with s_{CP} .

³Under a local rephasing $\psi \to e^{i\alpha(z)}\psi$ the WKB phase shifts by $\int \alpha' dz$, which is equivalent to $p_{cz} \to p_{cz} + \alpha'$. Hence p_{cz} is not gauge invariant, while observables built from kinetic quantities (below) are.

⁴We can adopt a fixed phase convention (e.g. $\alpha'=0$) and carry the bookkeeping variable s_{CP} ; all physical results are expressed in terms of *kinetic* quantities (group velocity, semiclassical force) that are rephasing–invariant. Or we can also use the "kinetic gauge" $\alpha'=-\frac{1}{2}s_{CP}\theta'$ so that canonical and kinetic momenta coincide at leading order; either choice leaves observables unchanged. In what follows, we will show that the physical quantities will be, of course, gauge invariant.

Inverting Eq. (12), the dispersion relation can be written as

$$E = \sqrt{(p_{cz} - \alpha_{CP})^2 + m^2} - s_{CP} \frac{s \theta'}{2}, \qquad \alpha_{CP} \equiv \alpha' \pm \frac{s_{CP} \theta'}{2}, \tag{13}$$

where the \pm refers to chirality, the difference drops out of kinetic observables. From now on, we write m to mean its modulus |m|. Restoring the conserved momentum parallel to the wall, $p_{\perp}^2 \equiv p_x^2 + p_y^2$, we define⁵

$$E_0 \equiv \sqrt{(p_{cz} - \alpha_{CP})^2 + p_\perp^2 + m^2}, \qquad E_{0z} \equiv \sqrt{(p_{cz} - \alpha_{CP})^2 + m^2},$$
 (14)

so that, to first order in gradients,

$$E = E_0 - s_{CP} s \frac{\theta' E_{0z}}{2E_0}. {15}$$

It is convenient to trade canonical for kinetic variables. Define the kinetic momentum by

$$p_z = (p_{cz} - \alpha_{CP}) \left(1 - s_{CP} \, s \, \frac{\theta'}{2E_{0z}} \right),$$
 (16)

and the corresponding kinetic energies

$$E_0 \equiv \sqrt{p_z^2 + p_\perp^2 + m^2(z)}, \qquad E_{0z} \equiv \sqrt{p_z^2 + m^2(z)}.$$
 (17)

Equation (15) then becomes the familiar shifted dispersion relation

$$E = E_0 \pm \Delta E = E_0 - s_{CP} s \frac{\theta' m^2}{2E_0 E_{0z}},$$
(18)

which is manifestly independent of α' , i.e. gauge invariant. More details on the difference between canonical and kinetic momentum and what is observable are given in Box 2.1.

2.3 Group velocity and semiclassical force

The group velocity along z is defined as

$$v_{gz} \equiv \frac{\partial E}{\partial p_{cz}} \simeq \frac{p_z}{E_0} \left(1 + s_{CP} \, s \, \frac{\theta' m^2}{2E_0^2 E_{0z}} \right). \tag{19}$$

Hamilton's equations, $\dot{z} = v_{gz}$ and $\dot{p}_z = -\partial E/\partial z$, give the semiclassical force

$$F_z \equiv \dot{p}_z \simeq -\frac{(m^2)'}{2E_0} + s_{CP} \, s \, \frac{(m^2 \theta')'}{2E_0 E_{0z}} - s_{CP} \, s \, \frac{m^2 (m^2)' \theta'}{4E_0^3 E_{0z}}, \tag{20}$$

written entirely in kinetic variables. The first term is CP-even and $\mathcal{O}(\partial_z)$, while the last two constitute the CP-odd piece at $\mathcal{O}(\partial_z^2)$, implying opposite forces for particles and antiparticles as they cross the wall.

Several simple limits provide useful cross-checks. If the phase is constant, $\theta' = 0$, all CP-odd terms in Eqs. (18) and (20) vanish, and one recovers the standard dispersion relation and semiclassical force for a real mass background. If the mass is constant, m' = 0, then $(m^2\theta')' = m^2\theta''$; in the adiabatic regime θ'' is suppressed so the CP-odd effects are correspondingly small, as expected. Finally, a local gauge rephasing $\alpha' \to \alpha' + \delta \alpha'$ shifts the canonical momentum p_{cz} but leaves the energy in Eq. (18), the group velocity in Eq. (19), and the force in Eq. (20) unchanged, confirming rephasing invariance of the kinetic observables. Taken together, Eqs. (18)-(20) furnish a gauge-invariant WKB kinematics accurate to first order in gradients, with a clean separation between CP-even and CP-odd pieces; these are the ingredients that enter the Liouville (Boltzmann) operator and the sources used in the transport analysis of electroweak baryogenesis.

⁵The mismatch reported in parts of the literature, see [34, 44], stems from boosting after manipulating the first–order (canonical) dispersion relation. As emphasised in Ref. [45], and confirmed in [26, 27], one should first boost the dispersion relation to the general frame (with finite p_{\perp}) and only then perform the gradient/onshell manipulations.

3 Boltzmann equations and fluid network

In this section, we turn the single—particle WKB kinematics into macroscopic transport equations. The strategy is simple in spirit. We start from the semiclassical equations of motion, which tell us how a WKB wave packet moves through the wall, and use them to build the Liouville operator that appears in the Boltzmann equation. We then expand the phase—space distribution around a local equilibrium appropriate to the moving plasma, separate CP—even from CP—odd pieces, and finally reduce the kinetic equation to a set of ordinary differential equations—the "fluid network"—for a few collective variables, namely the chemical potential and velocity perturbations. Along the way we will make explicit which terms are kept at each order in the gradient expansion, and we will isolate the CP—violating source terms that ultimately seed the baryon asymmetry.

3.1 Assumptions and equilibrium in the wall frame

The first ingredient is the choice of equilibrium about which we linearise. We work in the wall frame, where the background is static and depends only on the coordinate z normal to the wall. In collisions, we assume that the *kinetic* longitudinal momentum is conserved: to leading order in gradients, WKB particles scatter elastically in the slowly varying background, so the relevant on–shell energy entering the equilibrium distribution is the kinetic energy E_0 . This choice is consistent with the WKB Hamiltonian used in the previous section, where all observable quantities were expressed in terms of the kinetic momentum p_z .

With this in mind, the local equilibrium⁶ phase–space distribution for a species i is taken to be the usual Fermi–Dirac (FD) or Bose–Einstein (BE) function, but evaluated at the energy seen by the plasma moving with velocity v_w relative to the wall. In the wall frame, this amounts to boosting the single–particle energy by the factor $\gamma_w = (1 - v_w^2)^{-1/2}$ and replacing E with the kinetic expression $E_0^i = \sqrt{p_z^2 + p_\perp^2 + m_i^2(z)}$. The result is

$$f_{0w}^{i}(z,\mathbf{p}) = \frac{1}{\exp\left[\beta\gamma_{w}\left(E_{0}^{i}(z,\mathbf{p}) + v_{w}p_{z}\right)\right] \pm 1}, \qquad \beta \equiv \frac{1}{T},$$
(21)

where the upper (lower) sign is for fermions (bosons) and $p_{\perp}^2 \equiv p_x^2 + p_y^2$ is the momentum conserved parallel to the wall⁷. For later manipulations, it is convenient to also introduce the unboosted shorthand $f_0(E_0) \equiv [\exp(\beta E_0) \pm 1]^{-1}$, which is recovered smoothly in the limit $v_w \to 0$.

A technical convention will be used repeatedly and is therefore stated here. The derivatives of f_{0w} that appear upon linearisation are taken with respect to its argument $\gamma_w(E_0 + v_w p_z)$; we denote these by primes, e.g. $f'_{0w} \equiv \partial_{\gamma_w}(E_0 + v_w p_z) f_{0w}$ and similarly for f''_{0w} .

This specification of the equilibrium ensemble completes the starting point for our transport analysis. In the next subsection we will describe how small, space–dependent departures from f_{0w} are parametrised by a chemical potential and by an out-of–equilibrium piece δf , and how their CP properties are organised so that the CP–violating sources can be identified unambiguously.

3.2 Fluid ansatz, CP decomposition, and gradient expansion

To turn the single–particle kinematics into transport, we parametrise small departures from local equilibrium by a chemical potential and by a residual distortion of the phase–space shape. The guiding principle is that collisions in the slowly varying wall background drive each species toward a boosted equilibrium characterised by the kinetic energy E_0 , while the wall forces and spatial gradients continuously perturb the distribution.

⁶In the context of EWBG, the term *local equilibrium* is often used loosely, but it specifically refers to *local thermal* equilibrium: elastic scatterings are fast enough to maintain isotropic, thermal momentum distributions characterized by a common local velocity $u^{\mu}(x)$ and temperature T(x), while number–changing processes are slower and allow for small chemical potentials $\mu_a(x)$ between species. In the literature is commonly assume a uniform temperature, T = const., and treat deviations only through $\mu_a(x)$ and $u^{\mu}(x)$. A detailed discussion of the distinction between thermal, kinetic, and chemical equilibrium is provided in Appendix H.

⁷In local equilibrium one writes $f_{0w} = 1/\{\exp[\beta(u \cdot p)] \pm 1\}$. In the wall frame the plasma drifts along -z, so $u^{\mu} = \gamma_w(1, 0, 0, -v_w)$ and, with metric (+, -, -, -), $u \cdot p = \gamma_w(E_0 + v_w p_z)$.

We therefore write, for a given species, its distribution function as⁸

$$f(z, \mathbf{p}) = \frac{1}{\exp[\beta \gamma_w (E_0^i(z, \mathbf{p}) + v_w p_z) - \beta \mu(z)] \pm 1} + \delta f(z, \mathbf{p}), \qquad (22)$$

where μ is the chemical potential associated to the species and δf encodes departures from kinetic equilibrium that cannot be absorbed into a local density shift. Consistently with this interpretation, δf is imposed not to carry particle number,

$$\int d^3p \delta f(z, \mathbf{p}) = 0, \qquad (23)$$

so that number-density deviations are entirely captured by $\mu(z)^9$. In the wall frame, the kinetic WKB dispersion reads $E = E_0 + \Delta E$, with Eqs. (17) and (18), so that CP violation enters linearly through ΔE . It is convenient to expand around the boosted kinetic equilibrium $f_{0w}(z, \mathbf{p})$ and to treat both μ and ΔE as small in the gradient counting. Keeping terms up to second order in gradients, the distribution becomes

$$f \simeq f_{0w} + f'_{0w} \left(\gamma_w \, \Delta E - \mu \right) + \frac{1}{2} f''_{0w} \left(\gamma_w \, \Delta E - \mu \right)^2 + \delta f + \mathcal{O}(\partial_z^3) \,. \tag{24}$$

Now it is natural to split the perturbations into CP-even and CP-odd parts,

$$\mu = \mu_e + \mu_o, \qquad \delta f = \delta f_e + \delta f_o, \tag{25}$$

and to organise the full distribution as 10

$$f \equiv f_e + s_{\rm CP} f_o. \tag{26}$$

Reading off the even and odd pieces from (24) gives, to the stated order,

$$f_e \simeq f_{0w} - f'_{0w}\mu_e + \frac{1}{2}f''_{0w}\gamma_w^2 \Delta E^2 + \delta f_e ,$$
 (27)

$$f_o \simeq f'_{0w} \left(\gamma_w \Delta E - \mu_o \right) - f''_{0w} \gamma_w \Delta E \mu_e + \delta f_o.$$
 (28)

This decomposition makes the subsequent CP projection of the Boltzmann equation transparent: the even part collects the density-like response and the quadratic ΔE^2 correction that survives averaging, while the odd part contains the linear CP-violating response to the wall and the CP-odd chemical potential μ_o . In the next step we will insert $f = f_e + s_{\rm CP} f_o$ into the stationary Boltzmann equation L[f] = C[f], with the Liouville operator built from the WKB group velocity and force, and we will isolate the terms that act as CP-even and CP-odd sources for the fluid variables.

⁸At linear order, hydrodynamic perturbations separate into CP–even and CP–odd components. The temperature and flow distortions (δT , $\delta u^{\mu} \sim v_w$) are CP–even, while the chemical potentials μ_i —which describe particle–antiparticle asymmetries—are CP–odd. This separation explains why, in electroweak baryogenesis, one usually studies only the perturbations in velocity and chemical potentials when computing the CP–odd transport that sources the baryon asymmetry, treating T as fixed by rapid kinetic equilibration. Conversely, when determining the wall velocity and friction—CP–even quantities controlled by energy–momentum flow—one must also include the temperature perturbation δT . Couplings between CP–even and CP–odd sectors appear only beyond leading order.

⁹As pointed out in [62], by a generalised fluid Ansatz we expand the non–equilibrium part of the distribution as a tensor series in momenta, $\delta f = w^{(0)} + p_{\mu}w^{(1)\mu} + p_{\mu}p_{\nu}w^{(2)\mu\nu} + \cdots$, rather than keeping only density and drift (perfect–fluid) modes. This is more general and can encode entropy–producing effects (e.g. shear/bulk–like corrections), but it loosens the direct link to physical observables: the coefficients $w^{(n)}$ are not uniquely interpretable (they mix under boosts, depend on chosen weights/normalisation, and their mapping to hydrodynamic fields is model– and scheme–dependent).

¹⁰For any phase–space quantity X (e.g. energy shift, chemical potential, or a deformation of the distribution) let \bar{X} denote its CP–conjugate evaluated at the same (z, \mathbf{p}) in the wall frame. Define the CP–even/odd projections $X_e \equiv \frac{1}{2} (X + \bar{X})$ and $X_o \equiv \frac{1}{2} (X - \bar{X})$. We then write $X = X_e + s_{\text{CP}} X_o$ with $s_{\text{CP}} = +1$ for particles and $s_{\text{CP}} = -1$ for antiparticles. In practice, we keep a fixed CP sign for all the "o" quantities, i.e. +1, and encode the CP flip entirely in s_{CP} , so we need not track barred quantities explicitly.

3.3 Liouville operator and the stationary Boltzmann equation

With the kinematics in hand, the transport problem starts from the Boltzmann equation 11,

$$L[f] \equiv (\dot{z}\,\partial_z + \dot{p}_z\,\partial_{p_z})\,f = C[f]\,,\tag{29}$$

written in the wall frame and evaluated in a steady state, so that there is no explicit time derivative. The Liouville operator is built from the WKB group velocity and force derived earlier in Eqs. (19) and (20). Two simple chain–rule identities make the action of L transparent once we expand around the boosted kinetic equilibrium $f_{0w}(z, \mathbf{p})$. Since f_{0w} depends on z and p_z only through its argument $\gamma_w(E_0 + v_w p_z)$, differentiation gives

$$\partial_z f_{0w} = \gamma_w f'_{0w} \frac{(m^2)'}{2E_0}, \qquad \partial_{p_z} f_{0w} = \gamma_w f'_{0w} \left(\frac{p_z}{E_0} + v_w\right),$$
 (30)

where we stress that f'_{0w} denotes the derivative of f_{0w} with respect to its argument. Substituting (30) and, at this stage, keeping only the leading pieces $v_{gz} \simeq p_z/E_0$ and $F_z \simeq -(m^2)'/(2E_0)$, one immediately finds

$$L[f_{0w}] = v_{gz} \,\partial_z f_{0w} + F_z \,\partial_{p_z} f_{0w} \simeq \frac{p_z}{E_0} \,\gamma_w f'_{0w} \,\frac{(m^2)'}{2E_0} - \frac{(m^2)'}{2E_0} \,\gamma_w f'_{0w} \left(\frac{p_z}{E_0} + v_w\right)$$

$$= -v_w \,\gamma_w \,\frac{(m^2)'}{2E_0} \,f'_{0w} \,. \tag{31}$$

This is the CP-even driving term that appears later as the source in the fluid equations. It has a simple physical meaning: in the wall frame, a nonzero wall velocity v_w biases the flow in the presence of a spatially varying mass.

Going beyond the leading order is equally systematic. The CP-odd corrections to v_{gz} and F_z , together with the CP-odd piece of the distribution arising from ΔE , generate the familiar structures proportional to $(m^2\theta')'$ and to $m^2(m^2)'\theta'$. They enter through the same two terms, but are suppressed by one extra gradient, as anticipated by the counting. In practice, one now substitutes the expanded distribution $f = f_e + s_{\rm CP} f_o$ into L[f], uses the identities (30), and keeps terms consistently up to first order in gradients for CP-even and up to second order for CP-odd. The result is a linear combination of derivatives of the chemical potentials $\mu_{e,o}$, derivatives of the out-of-equilibrium piece $\delta f_{e,o}$, and a remainder that does not depend on perturbations. We shall refer to this remainder as the source, because it persists even if μ and δf are set to zero and therefore initiates the departure from equilibrium.

The algebra is straightforward but not particularly illuminating, so we postpone the fully expanded expressions to the next subsection, where we project L[f] onto its CP-even and CP-odd parts. There we will see explicitly how the even source (31) sits at $\mathcal{O}(\partial_z)$ while the odd source enters at $\mathcal{O}(\partial_z^2)$, and how the various gradient structures organize themselves in terms that multiply $\mu_{e,o}$, $\delta f_{e,o}$, or no perturbation at all.

3.4 CP projection and identification of sources

Armed with the Liouville operator, the next step is to separate the kinetic equation into its CP-even and CP-odd parts. This is more than a bookkeeping choice: once the distribution is expanded as $f = f_e + s_{\text{CP}} f_o$, with f_e even and f_o odd under CP, the Boltzmann equation L[f] = C[f] cleanly splits into two independent equations at the orders of interest. Operationally, we define the projections by combining the particle equation with its CP conjugate,

$$L[f]\Big|_{\text{CP-odd}} \equiv \tfrac{1}{2} \Big(L[f] - \overline{L[\bar{f}\,]} \Big) \,, \qquad L[f]\Big|_{\text{CP-even}} \equiv \tfrac{1}{2} \Big(L[f] + \overline{L[\bar{f}\,]} \Big) \,,$$

where the overline denotes flipping the CP-odd ingredients ($s_{\text{CP}} \rightarrow -s_{\text{CP}}$). This projection isolates the pieces that must change (or not) sign between particles and antiparticles.

 $^{^{-11}}$ We use a different convention of signs for the collision operator than the one used in [49, 63], where we define the collision operator to have a - in the definition in App. B.

For the CP–odd projection, the result can be written, retaining terms up to $\mathcal{O}(\partial_z^2)$ and linear in the perturbations, as

$$L[f]\Big|_{\text{CP-odd}} = -\frac{p_z}{E_0} f'_{0w} \mu'_o + v_w \gamma_w \frac{(m^2)'}{2E_0} f''_{0w} \mu_o - \frac{(m^2)'}{2E_0} \partial_{p_z} \delta f_o + \frac{p_z}{E_0} \partial_z \delta f_o$$

$$+ s v_w \gamma_w \frac{m^2(m^2)'\theta'}{4E_0^2 E_{0z}} \Big(\frac{f''_{0w}}{E_0} - \gamma_w f'''_{0w} \Big) \mu_e + \gamma_w v_w \frac{s (m^2\theta')'}{2E_0 E_{0z}} f''_{0w} \mu_e$$

$$+ \frac{s p_z m^2 \theta'}{2E_0^2 E_{0z}} \Big(\gamma_w f''_{0w} - \frac{f'_{0w}}{E_0} \Big) \mu'_e + \frac{s}{2E_0 E_{0z}} \Big[(m^2\theta')' - \frac{m^2(m^2)'\theta'}{2E_0^2} \Big] \partial_{p_z} \delta f_e + \frac{s p_z m^2\theta'}{2E_0^3 E_{0z}} \partial_z \delta f_e$$

$$+ \gamma_w v_w \frac{s (m^2\theta')'}{2E_0 E_{0z}} f'_{0w} + s v_w \gamma_w \frac{m^2(m^2)'\theta'}{4E_0^2 E_{0z}} \Big(\gamma_w f'''_{0w} - \frac{f'_{0w}}{E_0} \Big) + \mathcal{O}(\partial_z^3, \mu^2) \,. \tag{32}$$

The final line contains the CP–violating *source* terms, i.e. the pieces independent of μ and δf . Collecting them explicitly,

$$S_o \equiv -\gamma_w v_w \frac{s(m^2 \theta')'}{2E_0 E_{0z}} f'_{0w} - s v_w \gamma_w \frac{m^2 (m^2)' \theta'}{4E_0^2 E_{0z}} \left(\gamma_w f''_{0w} - \frac{f'_{0w}}{E_0} \right). \tag{33}$$

A feature that is worth emphasising is that all CP-odd structures are of order ∂_z^2 , as anticipated by the WKB counting at the end of section 2.1.

The CP-even projection proceeds in the same way, and one finds

$$L[f]\Big|_{\text{CP-even}} = -\frac{p_z}{E_0} f'_{0w} \mu'_e + v_w \gamma_w \frac{(m^2)'}{2E_0} f''_{0w} \mu_e - \frac{(m^2)'}{2E_0} \partial_{p_z} \delta f_e + \frac{p_z}{E_0} \partial_z \delta f_e$$

$$-\frac{s p_z m^2 \theta'}{2E_0^3 E_{0z}} f'_{0w} \mu'_o - \frac{s v_w \gamma_w}{2E_0 E_{0z}} \Big[(m^2 \theta')' \Big(1 + \frac{p_z}{v_w E_0} \Big) - \frac{m^2 (m^2)' \theta'}{2E_0^2} \Big] f''_{0w} \mu_o$$

$$+ \frac{s}{2E_0 E_{0z}} \Big[(m^2 \theta')' - \frac{m^2 (m^2)' \theta'}{2E_0^2} \Big] \partial_{p_z} \delta f_o + \frac{s p_z m^2 \theta'}{2E_0^3 E_{0z}} \partial_z \delta f_o$$

$$- v_w \gamma_w \frac{(m^2)'}{2E_0} f'_{0w} + \mathcal{O}(\partial_z^2, \mu^2) . \tag{34}$$

The CP-even *source* is simply the last term,

$$S_e \equiv v_w \gamma_w \frac{(m^2)'}{2E_0} f'_{0w},$$
 (35)

which already appeared in the warm-up computation $L[f_{0w}]$.

Solving directly for $\delta f_{e,o}(z,\mathbf{p})$ and $\mu(z)$ in Eqs. (32)-(34) is an hard task (see [63–67] for solving the CP even part): the unknown δf depends on the full three–momentum, the collision operator couples angles and energies with nonlocal kernels, and the resulting integro-differential system is stiff across the wall. Here, to obtain a simpler description, we project the kinetic equations onto a small set of macroscopic moments—e.g. density and longitudinal flux—by averaging over momentum with suitable weights. In practice, replacing $\delta f_{e,o}$ by its weighted moments and integrating (32)-(34) yields a closed, first-order linear system in z for a pair of collective variables (μ, u) in each CP sector, at least the considered order in perturbation, where the sources S_o and S_e from (33)-(35) enter as inhomogeneous terms and the interaction rates specify the collision closure. This moment (fluid) reduction retains the physically relevant charges and currents while avoiding the full momentum-resolved kinetics. However, for the CP-even sector it is now well established that low-order moment closures are unreliable: energy-momentum flow is sensitive to the angular structure and high-energy tails of δf , so truncations can violate exact conservation, misestimate friction and wall acceleration, and even produce spurious instabilities near the wall. Consequently, recent analyses abandon the moment projection for the CP-even problem and solve the Boltzmann equation directly for $\delta f_e(z, \mathbf{p})$ using modern numerical techniques, achieving stable and accurate determinations of the friction and wall velocity [63–67].

3.5 Moment expansion and normalisation

As anticipated in the previous subsection, the Boltzmann equation is an integro–differential equation in phase space, and to turn it into a simpler set of ordinary differential equations, we project it onto a few low–order moments in momentum. The idea is to weight the kinetic equation with simple functions of p_z/E_0 , integrate over momentum, and thereby trade the detailed shape of δf for a handful of "fluid" variables that capture the slow evolution driven by the wall. This procedure is effective because collisions quickly relax most angular structures, while the wall sources act coherently on low moments¹².

A convenient choice is to use the longitudinal velocity p_z/E_0 as the building block of the weights. For each non–negative integer ℓ we define a weighted phase–space average of any function $X(z, \mathbf{p})$ by

$$\langle X \rangle \equiv \frac{1}{N_1} \int d^3 p \, X(z, \mathbf{p}) \,, \qquad N_1 \equiv \int d^3 p \, f'_{0w, \text{FD}}(m=0) = -\gamma_w \frac{2\pi^3}{3} T^2 \,,$$
 (36)

where the overall factor N_1 fixes dimensions and is chosen so that the coefficients that appear below are universal functions of $x \equiv m/T$ and v_w (fermions and bosons differ only through the sign in f_{0w} that might appear in $X(z, \mathbf{p})$). With this normalisation in place, the velocity moments of the out-of-equilibrium part are introduced as

$$u_{\ell}(z) \equiv \left\langle \left(\frac{p_z}{E_0}\right)^{\ell} \delta f(z, \mathbf{p}) \right\rangle. \tag{37}$$

The zeroth moment of δf vanishes by construction, because δf does not carry particle number; the first two moments, u_1 and u_2 , will become the protagonists of the two-equation fluid system.

Projecting the stationary Boltzmann equation L[f] = C[f] with the weight $(p_z/E_0)^{\ell}$ produces the ℓ -th moment equation

$$\left\langle \left(\frac{p_z}{E_0}\right)^{\ell} L \right\rangle = \left\langle \left(\frac{p_z}{E_0}\right)^{\ell} \delta C \right\rangle, \tag{38}$$

where δC is the linearised collision term that we will properly define in the next subsections. The left-hand side can be written entirely in terms of μ , u_{ℓ} , and a set of coefficient functions by using the chain-rule identities established earlier for derivatives of f_{0w} and by substituting the WKB expressions for v_{gz} and F_z . After a straightforward manipulation one finds a structure that repeats for each ℓ : a term proportional to the gradient of the chemical potential, a term proportional to μ itself, two terms involving $\partial_z \delta f$ and $\partial_{pz} \delta f$, and, in the CP-odd channel, the source pieces coming from $(m^2 \theta')'$ and $m^2(m^2)'\theta'$. To keep the notation compact and to make the physical content transparent, it is useful to name the two universal kernels that multiply μ' and μ ,

$$D_{\ell} \equiv \left\langle \left(\frac{p_z}{E_0}\right)^{\ell} f'_{0w} \right\rangle, \qquad Q_{\ell} \equiv \left\langle \frac{p_z^{\ell-1}}{2E_0^{\ell}} f''_{0w} \right\rangle. \tag{39}$$

With these definitions, and keeping terms to the same gradient order used in the WKB section, the even part of the ℓ -th moment reads schematically

$$\left\langle \left(\frac{p_z}{E_0}\right)^{\ell} L \right\rangle_{e/o} = -D_{\ell+1} \mu' + v_w \gamma_w (m^2)' Q_{\ell+1} \mu + \left\langle \left(\frac{p_z}{E_0}\right)^{\ell+1} \partial_z \delta f \right\rangle - (m^2)' \left\langle \frac{p_z^{\ell}}{2E_0^{\ell+1}} \partial_{p_z} \delta f \right\rangle - \mathcal{S}_{\ell}. \tag{40}$$

The explicit expressions of $\mathcal{S}_{\ell}^{e/o}$ follow directly from the CP-even and CP-odd sources identified at the distribution level and amount to simple averages of those terms with the same weight $(p_z/E_0)^{\ell}$. At this stage, two remnants still link the moment equations to the detailed shape of δf : the averages of $\partial_z \delta f$ and $\partial_{p_z} \delta f$. In the next subsection we show how they can be rewritten in terms of the velocity moments u_{ℓ} and their derivatives by using a mild factorization assumption together with an integration-by-parts identity. This is the only additional closure needed to arrive at a closed fluid system for μ and the velocity perturbations u_{ℓ} .

¹²Physically, the wall drives a coherent drift mainly along z (building density and flux), while collisions rapidly randomise directions, washing out higher angular distortions. Thus, the slow dynamics are captured by the lowest "fluid–like" moments (chemical potentials and longitudinal flux). A useful image is a stirred coffee cup: the spoon sets a bulk swirl, while molecular collisions kill small eddies. This picture breaks down as $v_w \to 1$, where angular modes are not efficiently damped and one must retain the full moment hierarchy.

3.6 Closure: factorization and truncation

Projecting the Boltzmann equation onto moments has reduced the kinetic problem to a few phase–space averages. Two kinds of terms still prevent the system from closing on a small set of variables: averages that contain derivatives of the shape distortion, such as $\langle (p_z/E_0)^{\ell+1}\partial_z \delta f \rangle$ and $\langle p_z^{\ell}/(2E_0^{\ell+1})\partial_{p_z} \delta f \rangle$, and the tower of higher moments u_{ℓ} generated by the weights $(p_z/E_0)^{\ell}$. The first ingredient is a mild factorisation rule for averages that contain δf . We parametrise the first velocity moment as

$$u_1(z) \equiv u(z) = \left\langle \frac{p_z}{E_0} \, \delta f \right\rangle,$$

and approximate higher moments by pulling out the momentum dependence into a weight built on the equilibrium distribution. Concretely, for any function X we write

$$\langle X\delta f\rangle \simeq \left[X\frac{E_0}{p_z}\right]u, \qquad [X] \equiv \frac{1}{N_0} \int d^3p \, X f_{0w}, \qquad N_0 \equiv \int d^3p \, f_{0w}(m) = \gamma_w \, \hat{N}_0,$$
 (41)

where the square brackets denote a different normalisation from the N_1 -weighted averages used for D_ℓ and Q_ℓ . This factorisation preserves the exact number–sum rule $\int d^3p \, \delta f = 0$ and isolates the single amplitude u as the carrier of the out-of-equilibrium contribution. Applying (41) to the second velocity moment gives

$$u_2 = \left\langle \left(\frac{p_z}{E_0}\right)^2 \delta f \right\rangle \simeq \left[\frac{p_z}{E_0}\right] u \equiv Ru.$$
 (42)

The quantity R has a simple meaning: it is the average longitudinal velocity in the boosted equilibrium. Since f_{0w} is a boost of an isotropic distribution, its average velocity along the boost direction is fixed by kinematics to be the negative of the wall speed. Boosting back to the plasma frame makes this transparent and yields the exact identity

$$R = \left[\frac{p_z}{E_0}\right] = -v_w \,. \tag{43}$$

Thus the two-moment truncation closes the tower at $u_2 = Ru$ with no further modeling¹³.

The second ingredient is an integration-by-parts identity that trades the remaining averages of $\partial_z \delta f$ and $\partial_{p_z} \delta f$ for derivatives of the velocity moments and a single additional coefficient. Using Eq. (18) and keeping the dependence on m(z) explicit, one finds

$$\left\langle \frac{p_z^{\ell+1}}{E_0^{\ell+1}} \partial_z \delta f \right\rangle - (m^2)' \left\langle \frac{p_z^{\ell}}{2E_0^{\ell+1}} \partial_{p_z} \delta f \right\rangle = u_{\ell+1}' + \ell(m^2)' \bar{R} u_{\ell}, \tag{44}$$

where boundary terms vanish because we assume that δf dies off sufficiently fast in momentum space. The new coefficient

$$\bar{R} \equiv \left[\frac{1}{2p_z E_0} \right],$$

is well defined even though the integrand is divided by p_z : instead of taking a principal value, as already considered in the literature, it is easier to evaluate \bar{R} after boosting the integrand to the plasma frame, where f_0 is isotropic and d^3p/E_0 is Lorentz invariant. Performing the angular integral then leads to a one-dimensional representation,

$$\bar{R} = \frac{\pi}{\gamma_w^2 \hat{N}_0} \int_m^\infty dE \ln \left| \frac{p - v_w E}{p + v_w E} \right| f_0(E), \qquad p \equiv \sqrt{E^2 - m^2}, \tag{45}$$

where the statistic is included through f_0 .

Equations (43) and (44) are precisely what is needed to close the moment hierarchy. The factorization fixes the relation $u_2 = R u$, while the integration-by-parts identity eliminates the explicit derivatives

 $^{^{13}}$ A constant-R ("factorization") closure has been used since the early literature, often with R set by the boosted equilibrium, $R = -v_w$ (see e.g. [34], and the discussion in [51]). Other ad hoc choices appear, such as setting the last moment to zero (R = 0) or equal to the previous one (R = 1). All constant-R prescriptions imply the same gradient relation $u'_{\ell} = R u'_{\ell}$, i.e. derivatives propagate down the hierarchy with geometric weight R. The choice $R = -v_w$ is singled out by covariance: it reproduces the exact drift of f_{0w} in the wall frame and introduces no extra parameters.

of δf in favor of u'_{ℓ} and u_{ℓ} with a single extra kernel \bar{R} . Specialising to the lowest two moments $\ell=0,1$ then produces a closed, first-order system for the pair $(\mu(z),u(z))$ in each CP sector. In the next subsection we will write this system explicitly in matrix form, identify the corresponding sources by averaging the CP-even and CP-odd driving terms, and discuss the role of collisions in coupling different species.

Variance truncation. In the moment expansion of the longitudinal Boltzmann equation the hierarchy is unclosed: the equation for $u_{\ell} \equiv \langle (p_z/E_0)^{\ell} \, \delta f \rangle$ contains $u_{\ell+1}$. Besides the constant-R "factorization" (which assumes $u'_{\ell+1} = R \, u'_{\ell}$), a physically motivated closure is to set the ℓ -th central moment of the perturbation to zero,

$$\left\langle \left(\frac{p_z}{E_0} - u_1\right)^{\ell} \delta f \right\rangle = 0. \tag{46}$$

Expanding the binomial gives an algebraic relation that expresses the highest raw moment in terms of lower ones,

$$u_{\ell} = \sum_{k=1}^{\ell-1} {\ell \choose k} (-u_1)^{\ell-k} u_k - (-u_1)^{\ell} u_0, \qquad u_0 \equiv \langle \delta f \rangle, \tag{47}$$

which, in the standard setup where the density mode u_0 is handled by the chemical potential (hence $u_0 = 0$ for δf), simplifies to

$$u_{\ell} = \sum_{k=1}^{\ell-1} {\ell \choose k} (-u_1)^{\ell-k} u_k. \tag{48}$$

Differentiating (48) yields a linear relation for the derivatives,

$$u'_{\ell} = \sum_{i=1}^{\ell-1} R_i u'_i, \qquad R_i = \binom{\ell}{i} (-u_1)^{\ell-i} \quad (i \ge 2), \quad R_1 = \binom{\ell}{1} (-u_1)^{\ell-1} - \sum_{k=1}^{\ell-1} \binom{\ell}{k} (\ell-k)(-u_1)^{\ell-k-1} u_k, \tag{49}$$

so that the closure adapts smoothly to the local drift u_1 and introduces no extra parameters¹⁴.

3.7 From moments to a two-equation fluid network

With these ingredients, the $\ell=0$ and $\ell=1$ moment equations become, respectively,

$$-D_1\mu'(z) + u'(z) + v_w\gamma_w(m^2)'(z)Q_1\mu(z) = S_1(z) + \delta C_1(z), \qquad (50)$$

$$-D_2\mu'(z) + Ru'(z) + v_w\gamma_w(m^2)'(z)Q_2\mu(z) + (m^2)'(z)\bar{R}u(z) = \mathcal{S}_2(z) + \delta\mathcal{C}_2(z),$$
 (51)

where $S_{1,2}$ are the weighted sources obtained by averaging the driving terms identified at the CP-projection stage, and $\delta C_{1,2}$ are the corresponding moments of the linearised collision integral. These two equations are written once and for all; what distinguishes the CP-even and CP-odd sectors is solely the choice of $S_{1,2}$ appropriate to each case. For the even sector, the sources are proportional to $v_w \gamma_w(m^2)'$. For the odd sector, they are proportional to the two gradient structures $(m^2\theta')'$ and $m^2(m^2)'\theta'$ that carry the CP-violating physics of the wall. In both sectors, the coefficients $D_\ell, Q_\ell, R, \bar{R}$ are universal functions of the dimensionless mass x = m/T and of the wall speed v_w , differing only by statistics through the equilibrium distribution.

It is convenient to combine Eqs. (50)-(51) into a compact block–matrix form by introducing the state vector $w(z) \equiv (\mu(z), u(z))^{\mathsf{T}}$. This notation makes it straightforward to extend the system to an arbitrary number of velocity moments, as developed in Sec. 8. The system then reads

¹⁴In [51] a slightly different implementation of the "variance" closure is used (they keep a nonzero right–hand side for the central moment). The authors report that switching between these variants has no visible numerical impact on η_B within their benchmarks. We consider the RHS to be zero since with $\ell = 0$ it has to vanish by construction.

$$A w'(z) + (m^2)'(z) B w(z) = S(z) + \delta C(z),$$
 (52)

with

$$A = \begin{pmatrix} -D_1 & 1 \\ -D_2 & R \end{pmatrix}, \qquad B = \begin{pmatrix} v_w \gamma_w Q_1 & 0 \\ v_w \gamma_w Q_2 & \bar{R} \end{pmatrix}, \qquad \mathcal{S} = \begin{pmatrix} \mathcal{S}_1 \\ \mathcal{S}_2 \end{pmatrix}, \qquad \delta \mathcal{C} = \begin{pmatrix} \delta \mathcal{C}_1 \\ \delta \mathcal{C}_2 \end{pmatrix}.$$

This is a linear, first-order boundary-value problem along z. Physically, one requires the perturbations to vanish far away from the wall, where the background becomes homogeneous and the sources switch off, so $\mu, u \to 0$ as $z \to \pm \infty$. Once these conditions are imposed, the system can be solved independently in the CP-even and CP-odd channels, because the sources do not mix them at the order considered. Hereafter, we restrict to the CP-odd sector, the piece that sources the weak-sphaleron bias and is therefore the component relevant for computing the baryon asymmetry η_B . The chemical potential produced in the CP-odd sector is the quantity that will feed the anomalous baryon number violation in front of the wall and determine the final baryon asymmetry.

3.8 Collision terms and model-independent closure

To close the two–moment fluid system we must specify how interactions relax small departures from boosted kinetic equilibrium. We work with the *linearised* collision operator and separate, at the level of the integrand, inelastic (number/charge– changing) and elastic (momentum–redistributing) contributions. Throughout this subsection, objects *inside* the momentum averages are denoted in plain font by δC ; once averaged, we denote them by calligraphic δC .

For each species, we define the two projected moments

$$\delta C_1 \equiv \langle \delta C \rangle, \qquad \delta C_2 \equiv \left\langle \frac{p_z}{E_0} \delta C \right\rangle.$$
 (53)

We split the linearised collision integrand into inelastic and elastic parts, $\delta C \simeq \delta C^{\text{inel}} + \delta C^{\text{el}}$. Inelastic reactions drive specific linear combinations of the dimensionless chemical potentials $\xi_i \equiv \mu_i/T$ toward zero, whereas elastic scatterings conserve all charges and only relax the momentum–space distortion δf . Let $s_{ij} \in \{-1,0,+1\}$ be the coefficient that specifies how species j enters channel i (negative if it appears in the initial state of i, positive if it appears in the final state, and zero if absent). Then the wall–frame, linearised integrand can be written as

$$\delta C_a^{\text{inel}} \simeq -f_{0w}^a \sum_{i,j} \Gamma_{i\to j}^{\text{wf, inel}} s_{ij} \, \xi_j - \delta f^a(p) \sum_{i,j} \Gamma_{i\to j}^{\text{wf, inel}}, \tag{54}$$

$$\delta C_a^{\rm el} \simeq -\delta f^a(p) \sum_{i,j} \Gamma_{i \to j}^{\rm wf,\,el} \,.$$
 (55)

Here i/j label, respectively, the reaction channel and the participating species; the sums run over all open processes that involve a and over all species that participate in each process. "wf" denotes the wall frame, and Γ is the microscopic rate for that process in that frame. Inelastic channels include both decays $(1 \rightarrow 2)$ and inelastic scatterings $(2 \rightarrow 2)$. For elastic channels the first (chemical-potential) term is absent because no charge is exchanged, while the δf term survives and encodes momentum relaxation.

At this stage the Γ^{wf} retain their full momentum dependence. In the Box 3.1 we explain the difference with the *per-particle* rates. Equations (53)-(54) are therefore the most model–agnostic form of the linearised collision integrand; the only inputs are the list of channels and the coefficients s_{ij} .

3.8.1 Averaged rates.

To match common usage in the literature, we first emphasise that the Γ 's in Eqs. (54) $^{\sim}$ -(55) are not yet averaged: they are momentum-resolved wall-frame kernels that retain full dependence on

Box 3.1: Rates convention

Notation: un-averaged vs. per-particle rates. In Eq. (54)-(55) the symbols Γ denote momentum-dependent collision rate in the wall-frame Boltzmann operator; they still depend on the test particle energy/momentum p and are not per-particle rates. In order to define the per-particle rate, we need to thermally average over initial/final states, then kernels become momentum-independent:

 $\Gamma \equiv \text{un-averaged, momentum-dependent rate,}$

 $\widehat{\Gamma} \equiv \text{thermally averaged (per-particle) rate.}$

From now on, we use a hat to denote averaged rates, reserving Γ for unaveraged kernels.

the test–particle momentum p. To embed them into a fluid description, one trades $\Gamma(p)$ for a single per-particle rate via a thermal average,

$$\Gamma(p) \longrightarrow \frac{T^3/12}{n_X} \frac{12}{T^3} \int \frac{d^3p}{(2\pi)^3} f_{0,X}(p) \Gamma(p) \equiv \kappa^X \widehat{\Gamma} , \qquad (56)$$

where $f_{0,X}$ is the chosen equilibrium weight and $n_X \equiv \int d^3p \, f_{0,X}/(2\pi)^3$ fixes the normalisation. With this convention, $\widehat{\Gamma}$ coincides with the per–particle rates defined in Appendices D and E, and the conversion factor

$$\kappa^{X} = \frac{T^{3}/12}{n_{X}} = \begin{cases} \frac{\pi^{2}}{9\zeta(3)} \simeq 0.912, & \text{FD} \\ \frac{\pi^{2}}{12\zeta(3)} \simeq 0.685, & \text{BE} \\ \frac{\pi^{2}}{12} \simeq 0.822, & \text{MB} \end{cases}$$
 (57)

is the usual per-degree-of-freedom rescaling between the $(12/T^3)$ convention and the $(1/n_X)$ convention¹⁵. By default, we take $f_{0,X}$ to be the Fermi-Dirac/Bose-Einstein distribution of the tracked species; alternatively, some works (explicitly [51]) adopt a Maxwell-Boltzmann (MB) weight to remain statistics-agnostic. In particular, [51] normalise with N_1 instead of the factor $12/T^3$; in that normalisation $\widehat{\Gamma}$ cannot be directly identified with the per-particle rates in the appendices without an additional overall rescaling. The chosen averaging/normalisation coherently fixes the set of universal projection constants that accompany the averaged rates in the moment equations; if one includes spin/colour degeneracies, n_X (and hence κ^X) must be adjusted consistently.

3.8.2 Momentum-space average of the collision operator

Exact collision integrals in Eqs. (54)-(55) retain a residual dependence on the test-particle momentum p. Within the moment projection, we replace each microscopic, momentum-resolved kernel by a momentum-space averaged (per-particle) rate $\hat{\Gamma}_i$, appropriately normalised so as to match the conventions used in the appendices. This quantity captures the weighted impact of the underlying process on the chosen moment and renders the collision terms momentum-independent in the fluid system. Implementing this replacement and performing the two projections produces species-dependent normalisations, which we collect into

$$K^{(\ell)} \equiv \left\langle \left(\frac{p_z}{E_0}\right)^{\ell} f_{0w} \right\rangle. \tag{58}$$

These $K^{(\ell)}$ are universal functions of the dimensionless mass $x_a \equiv m_a/T$ and of the wall velocity v_w . One can further write

$$K^{(\ell)} = -K_0 \left[\left(\frac{p_z}{E_0} \right)^{\ell} \right], \quad \text{with} \quad K_0 = -\langle f_{0w} \rangle , \qquad (59)$$

 $^{^{15}}$ We have verified that including the full mass dependence in n_X does not lead to any qualitative change in the results.

which makes contact with the notation of Ref. [49]: for $\ell = 0$ it reduces to $-K_0$, while for $\ell = 1$ it gives $+v_wK_0$.

With the averaged rate $\hat{\Gamma}$ and the normalisations κ^X and $K^{(\ell)}$ in place, the two averaged collision moments take the compact form

$$\delta \mathcal{C}_1^a \supset -K_a^{(0)} \kappa^X \sum_{i,j} \widehat{\Gamma}_{i \to j}^{\text{inel}} s_{ij} \, \xi_j, \tag{60}$$

$$\delta \mathcal{C}_2^a \supset -K_a^{(1)} \kappa^X \sum_{i,j} \widehat{\Gamma}_{i \to j}^{\text{inel}} s_{ij} \, \xi_j - \kappa_a^X \, \widehat{\Gamma}_{\text{tot}}^a \, u_{1,a}, \qquad \widehat{\Gamma}_{\text{tot}}^a \equiv \sum_{i \in a} \widehat{\Gamma}_i^{\text{el}} + \widehat{\Gamma}_i^{\text{inel}} \,. \tag{61}$$

Thus, inelastic channels relax the appropriate combinations of ξ_j (dimensionless chemical potentials) in both moments, while elastic processes (and the elastic part of inelastic channels) appear only as a flow-damping contribution in the second moment via $\widehat{\Gamma}_{\text{tot}}^a$ and the first velocity mode $u_{1,a}$.

Total rate. We define the momentum–averaged total interaction rate of species a as in (61), which acts as the effective damping of the first velocity moment $u_{1,a}$ in the fluid equations. Physically, $\hat{\Gamma}_{\text{tot}}^a$ quantifies the relaxation of momentum perturbations of species a due to collisions with the plasma. However, in the moment formalism a different definition is used, that is in terms of the moment functions $D_{\ell,i}$ and recast it as

$$\widehat{\Gamma}_{\text{tot},i} = -\frac{D_{2,i}(x, v_w)}{v_w D_{1,i}(x, v_w) D_i} \xrightarrow{v_w \ll 1} \frac{K_{4,i}^{\text{FH06}}}{D_i K_{1,i}^{\text{FH06}}},$$
(62)

where $D_{\ell,i}$ are the moment weights defined in (39), $K_{\ell,i}^{\text{FH06}}$ are the moment weights defined in FH06 and D_i denotes the (species–dependent) diffusion constant. We stress that this identification is formally circular if D_i is itself defined using $\widehat{\Gamma}_{\text{tot},i}$ and then reused to compute it; the microphysically consistent approach is to obtain $\widehat{\Gamma}_{\text{tot},i}$ from the full interaction width of the particle and only subsequently define the diffusion constants¹⁶. In this review we follow the standard conventions adopted in the EWBG literature for these quantities and proceed accordingly.

Strong sphalerons and the quark sector. Since in this review we are interested in EWBG within the SM augmented by new physics that renders the EWPT first order, we necessarily track the evolution of the top/bottom chiral sector together with the Higgs, i.e. (t_L, b_L, t_R, h) . In this setting the QCD strong sphalerons (SS) must be included: they violate axial (chiral) charge in the quark sector while conserving baryon number, and they rapidly drive the combination $\sum_{q}^{n_f} (\xi_{q_L} - \xi_{q_R})$ toward zero in front of the wall. At the moment level, as done in [51], we include the SS contribution as follows

$$\delta C_1^a \big|_{ss} = -K_a^{(0)} c_a^{ss} \, \Gamma_{ss} \, \sum_{q}^{n_f} (\xi_{qL} - \xi_{qR}), \qquad \delta C_{\ell \ge 2}^a \big|_{ss} \simeq 0, \tag{63}$$

where Γ_{ss} is the strong sphaleron rate, $c_a^{ss} = +1$ for left-handed quarks, $c_a^{ss} = -1$ for right-handed quarks of any flavour, and $c_a^{ss} = 0$ for non-quark species (e.g. Higgs, leptons). Reference [51] justify the restriction to the lowest moment following from the fact that SS dynamics is dominated by deep-infrared gauge modes and is known from lattice studies only at the integrated level; any genuine momentum dependence beyond δC_1 is strongly suppressed¹⁷.

¹⁶We thank Enrique Fernandez-Martinez for this clarifying remark, raised during a discussion.

 $^{^{17}}$ Reference [51] checked that allowing a small nonzero SS contribution in $\delta\mathcal{C}_2$ does not affect the results within numerical uncertainties. See App. B for discussion and references. This is important since in all the other references it has been considered in the higher momenta as $\delta\mathcal{C}_2^a = -K_a^{(1)}c_a^{ss}\,\Gamma_{ss}\,\sum_q^{n_f}\left(\xi_{q_L}-\xi_{q_R}\right)$. In BARYONET for all the implementations except KV24, this contribution is considered in $\delta\mathcal{C}_2$, while when implementing KV24 it is not.

Eliminating light quarks. Light flavours enter our fluid network only through QCD strong sphalerons. In the absence of Yukawa mixing, they satisfy $\mu_{q_R} = -\mu_{q_L}$ for each light species q, and—on the transport time scale where electroweak sphalerons are slow—baryon number conservation implies that their net baryon density vanishes. One can then solve the light–quark potentials in terms of the heavy sector,

$$\mu_{qL} = -\mu_{qR} = D_0^t \mu_{tL} + D_0^b \mu_{bL} + D_0^t \mu_{tR}, \tag{64}$$

where D_0^{α} are the $\ell = 0$ thermal kernels introduced earlier. Substituting (64) into the strong–sphaleron functional gives

$$\sum_{q} (\mu_{q_L} - \mu_{q_R}) = (1 + 9D_0^t)\mu_{t_L} + (1 + 9D_0^b)\mu_{b_L} - (1 - 9D_0^t)\mu_{t_R} \equiv \mu_{ss}.$$
 (65)

Summary. We have (i) linearised the microscopic collision integrand δC by separating inelastic, number-/charge-changing channels from purely elastic, momentum-redistributing ones; (ii) compressed the momentum dependence of each channel into a single average $\hat{\Gamma}$ by a thermal average with the proper normalisation; and (iii) projected the result onto the fluid moments that appear in the truncated Boltzmann hierarchy. The second step introduces universal equilibrium averages $K_a^{(\ell)}$ and the species-dependent normalisation κ_a^X . Stacking all species then yields a compact, reusable closure for the linearised, averaged collision operator, reported below.

linearised averaged collision operator

$$\delta \mathcal{C}_{\ell+1}^{a} = -K_{a}^{(\ell)} \kappa_{a}^{X} \sum_{i,j} \widehat{\Gamma}_{i \to j}^{\text{inel}} s_{ij} \, \mu_{j} - K_{a}^{(\ell)} \delta_{\ell 0} \Gamma_{ss} \mu_{ss} - \kappa_{a}^{X} \, \widehat{\Gamma}_{\text{tot}}^{a} \, u_{\ell,a}, \qquad \widehat{\Gamma}_{\text{tot}}^{a} \equiv \sum_{i \in a} \widehat{\Gamma}_{i}^{\text{el}} + \widehat{\Gamma}_{i}^{\text{inel}} \, . \tag{66}$$

3.9 Weighted sources

Once the Boltzmann equation has been projected on moments, the driving terms that remain after setting $\mu = \delta f = 0$ must be averaged with the same weights $(p_z/E_0)^{\ell}$ used to build the fluid variables. This step is purely kinematic and turns the distribution–level sources found in the CP projection into the inhomogeneities that appear on the right–hand side of the moment equations.

In the CP-even sector, the source originates from the term proportional to $(m^2)'$. After the $(p_z/E_0)^{\ell}$ averaging it collapses to a single coefficient,

$$Q_{\ell}^{e} \equiv \left\langle \frac{p_{z}^{\ell-1}}{2E_{0}^{\ell}} f_{0w}^{\prime} \right\rangle, \tag{67}$$

so that the weighted source reads

$$\mathcal{S}_{\ell}^{e}(z) = v_w \, \gamma_w \, (m^2)'(z) \, Q_{\ell}^{e}. \tag{68}$$

This is the same structure that already appeared unweighted at the distribution level; the averaging only replaces bare factors of $1/(2E_0)$ by their thermal expectation values with the appropriate weight.

The CP-odd sector contains two independent gradient structures, $(m^2\theta')'$ and $m^2(m^2)'\theta'$. Their weights involve either E_{0z}^{-1} or an extra power of E_0^{-1} . It is convenient to define

$$Q_{\ell}^{8o} \equiv \left\langle \frac{s \, p_z^{\ell-1}}{2E_0^{\ell} E_{0z}} \, f'_{0w} \right\rangle, \qquad Q_{\ell}^{9o} \equiv \left\langle \frac{s \, p_z^{\ell-1}}{4E_0^{\ell+1} E_{0z}} \left(\frac{f'_{0w}}{E_0} - \gamma_w f''_{0w} \right) \right\rangle, \tag{69}$$

where the spin label $s=\pm 1$ has been retained explicitly to keep track of the helicity dependence that accompanies the CP–violating energy shift. With these definitions the averaged CP–odd source becomes

$$S_{\ell}^{o}(z) = -v_{w}\gamma_{w} \left[(m^{2}\theta')'Q_{\ell}^{8o} - m^{2}(m^{2})'\theta'Q_{\ell}^{9o} \right], \tag{70}$$

which is nothing but the weighted version of the two CP-odd operators identified earlier. Figure 2 visualises the moment-projected CP-odd sources for the top sector, using as a benchmark the xSM model defined below with parameters as in (99).

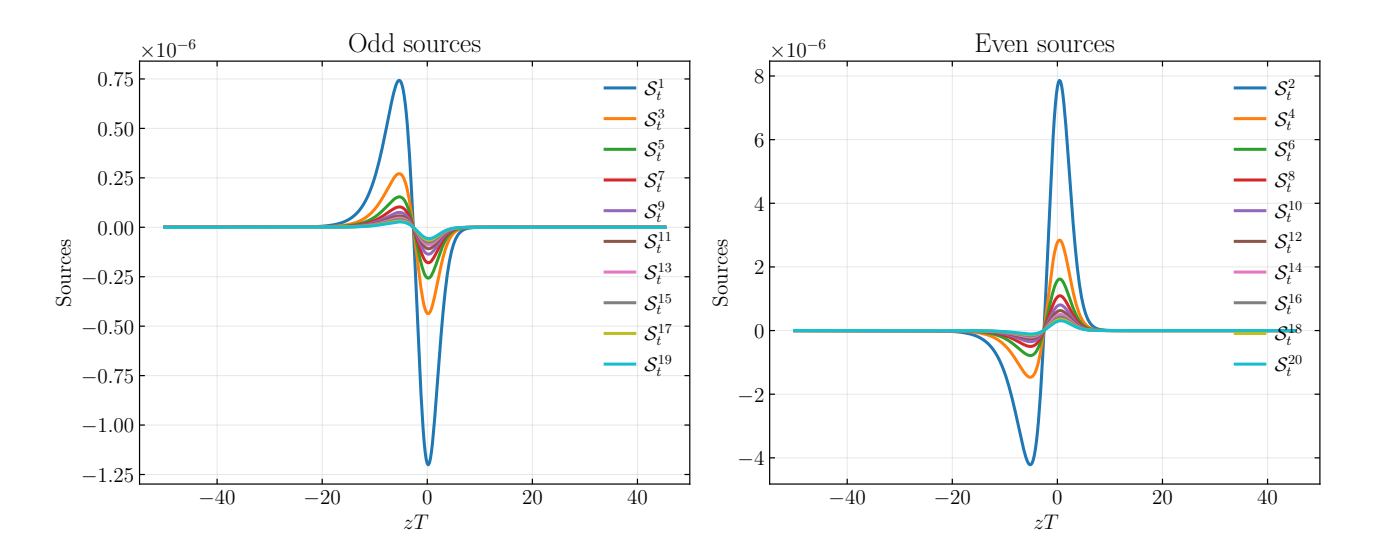


Figure 2: Weighted source multiplets for the top sector as functions of the dimensionless wall coordinate zT. The left panel shows the CP-odd sources \mathcal{S}_{ℓ}^t for odd ℓ , while the right panel shows those for even ℓ . All curves are localised near the interface, and the even sources suffer from velocity suppression in comparison to the odd ones.

3.10 Dimensionless rescaling and universal kernels

To make explicit that the whole framework is temperature—independent—i.e. all quantities can be expressed in units of the temperature—it is useful to track how every object scales with T. We measure dimensions in powers of T and denote this with square brackets $[\cdot]$.

The starting point is the boosted equilibrium distribution f_{0w} , whose full argument is $\beta \gamma_w (E_0 + v_w p_z)$ with $\beta = T^{-1}$. Derivatives with respect to this argument, as in Sec. 3, therefore, bring down inverse powers of T

$$[f_{0w}^{(n)}] = T^{-n} \,. (71)$$

From this, the momentum averages used throughout inherit the scalings

$$[\langle \cdot \rangle] = T, \qquad [[\cdot]] = T^0. \tag{72}$$

Consequently, the thermal kernels and kinematic factors appearing in the fluid equations scale as

$$[D_{\ell}] = T^{0}, \qquad [Q_{\ell}] = T^{-2}, \qquad [R] = T^{0}, \qquad [\bar{R}] = T^{-2},$$
 (73)

$$[D_{\ell}] = T^{0}, [Q_{\ell}] = T^{-2}, [R] = T^{0}, [\bar{R}] = T^{-2}, (73)$$
$$[Q_{\ell}^{e}] = T^{-1}, [Q_{\ell}^{8o}] = T^{-2}, [Q_{\ell}^{9o}] = T^{-4}, [K^{(\ell)}] = T^{1}. (74)$$

The background profiles contribute gradients with the expected dimensions,

$$[(m^2)^{(n)}] = T^{2+n}, \qquad [\theta^{(n)}] = T^n.$$
 (75)

With these assignments, the natural dimensionless variables are the reduced chemical potential $\xi \equiv \mu/T$ and the rescaled wall coordinate $\tilde{z} \equiv zT$. Written in terms of $\xi(\tilde{z})$, $\chi(\tilde{z}) \equiv |m|/T$, and $\theta(\tilde{z})$, both Eqs. (50) and (51) carry an overall and uniform factor T^2 . Dividing through by this factor yields a fully dimensionless system in which all coefficients are universal functions of (x, v_w) , and any explicit temperature–dependence has been scaled out. This normalisation is not only conceptually clean—cleanly separating physics from units—but also numerically advantageous, as the universal kernels can be pre-tabulated once and interpolated across models.

Phenomenological models 4

We adopt a minimal, phenomenological setup that captures the structure of EWBG driven by top-Yukawa dynamics without committing to a specific ultraviolet completion. The goal is to have a concrete yet model—agnostic playground where the collision operator, the choice of tracked species, and the interplay of fast interactions can be displayed transparently.

We keep the four degrees of freedom most tightly coupled by the top Yukawa: left– and right–handed tops (t_L, t_R) , the left–handed bottom b_L , and the Higgs h. Each species is described by the two–component fluid vector $w_i(z) \equiv \begin{pmatrix} \mu_i(z) & u_i(z) \end{pmatrix}$ where $i \in \{t_L, b_L, t_R, h\}$, and μ_i is the chemical potential and u_i the longitudinal velocity moment. With the universal kernels defined earlier, the dynamics is written compactly as the linear, first–order system as in (52) with block 2×2 matrices A, B, source vector S, and linearised collision vector S specified by the physics below.

Interactions that control equilibration. The collision sector includes precisely those processes that efficiently couple $\{t_L, b_L, t_R, h\}$ in the symmetric phase: (i) charged-current W scatterings, which drive $\mu_{t_L} \simeq \mu_{b_L}$; (ii) QCD strong sphalerons, which rapidly equilibrate axial quark charge across flavours; (iii) top helicity flips ("mass insertions"), which damp $\mu_{t_L} - \mu_{t_R}$ and feed the scalar channel; (iv) Higgs-number damping in the scalar sector; and (v) Yukawa exchange among (t_L, b_L, t_R, h) . These ingredients enter only through the components of δC .

For each species i we use the general form as in Eq. (66), but with $\ell = 0, 1$. The first components δC_1^a are linear in the chemical potentials and contain the rates for the fast processes listed above. Explicitly, for the four-species set¹⁸

$$\delta \mathcal{C}_1^{t_L} \propto \widehat{\Gamma}_y^t (\mu_{t_L} - \mu_{t_R} + \mu_h) + 2\widehat{\Gamma}_m^t (\mu_{t_L} - \mu_{t_R}) + \widehat{\Gamma}_W (\mu_{t_L} - \mu_{b_L}) + \widetilde{\Gamma}_{ss}[\mu], \tag{76}$$

$$\delta \mathcal{C}_1^{b_L} \propto \widehat{\Gamma}_y^t (\mu_{b_L} - \mu_{t_R} + \mu_h) + \widehat{\Gamma}_W (\mu_{b_L} - \mu_{t_L}) + \widetilde{\Gamma}_{ss}[\mu], \tag{77}$$

$$\delta \mathcal{C}_1^{t_R} \propto -\widehat{\Gamma}_y^t (\mu_{t_L} + \mu_{b_L} - 2\mu_{t_R} + 2\mu_h) + 2\widehat{\Gamma}_m^t (\mu_{t_R} - \mu_{t_L}) - \widetilde{\Gamma}_{ss}[\mu], \tag{78}$$

$$\delta \mathcal{C}_1^h \propto \frac{3}{2} \widehat{\Gamma}_y \left(\mu_{t_L} + \mu_{b_L} - 2\mu_{t_R} + 2\mu_h \right) + \widehat{\Gamma}_m^h \mu_h, \tag{79}$$

where $\Gamma_{ss}[\mu] \equiv \Gamma_{ss} \mu_{ss}$ with μ_{ss} defined in Eq. (65). We recall that $\widehat{\Gamma}$ are the averaged per-particle rate, and they have dimension T, see appendices D and E for full details. We can now stack the four two-component vectors into a single column $U^T \equiv (w_{t_L}^T, w_{b_L}^T, w_{t_R}^T, w_h^T)$ then Eq. (52) applies with $A = \operatorname{diag}(A_{t_L}, A_{b_L}, A_{t_R}, A_h)$ block-diagonal, while \mathcal{S} collects the CP-even/odd sources and $\delta \mathcal{C}$ the linearised collisions terms just specified. Far from the wall, where profiles are constant and sources vanish, the boundary conditions are $U(\pm \infty) = 0$. This closes a compact four-species, two-moment network that faithfully represents the EWBG physics we aim to test, independent of the ultraviolet details of the CP-violating model.

4.1 Baryon–left chemical potential $\mu_{B_I}(z)$

Electroweak sphalerons couple to the *left-handed* quark number carried by the $SU(2)_L$ doublets. In the fluid description, this enters through a single linear combination of chemical potentials, the *baryon-left* chemical potential $\mu_{B_L}(z)$. It is the object that sources baryon number in the weak–sphaleron sector (see [68, 69]), schematically

$$\frac{d\eta_B}{dz} \propto \Gamma_{ws}(z) \left(\text{const} \times \mu_{B_L}(z) - A \eta_B(z) \right), \tag{80}$$

so once the transport system is solved, $\mu_{B_L}(z)$ is the only input from the charge sector needed by the baryon equation.

¹⁸The numerical prefactors in Eqs. (76)–(79) arise from simple counting arguments. The factor 2 in front of $\widehat{\Gamma}_m$ reflects that helicity–flip processes $t_L \leftrightarrow t_R$ act identically on particles and antiparticles; when written in terms of charge–asymmetry chemical potentials, both contributions add, doubling the effective rate. The factor 3/2 in the Higgs equation originates from the ratio of internal degrees of freedom, $N_c/N_h=3/2$, since three quark colours feed a single Higgs doublet counted as two components. No additional prefactors appear for $\widehat{\Gamma}_y$ or $\widehat{\Gamma}_W$, because those rates are already defined per particle and include all relevant multiplicity and symmetry factors in their averaged definitions.

By definition,

$$\mu_{B_L}(z) \equiv \frac{1}{2} \sum_{\text{all quarks } q} \mu_{q_L}(z). \tag{81}$$

Using the light-quark elimination derived in (64), the sum can be written entirely in terms of third-generation variables with the universal thermal kernels D_0^a , defined in (39),

Baryon-left chemical potential

$$\mu_{B_L}(z) = \frac{1}{2} \left(1 + 4 D_0^t \right) \mu_{t_L}(z) + \frac{1}{2} \left(1 + 4 D_0^b \right) \mu_{b_L}(z) + 2 D_0^t \mu_{t_R}(z). \tag{82}$$

Different conventions in FH04 vs. FH06. The two formalisms define the baryon–left chemical potential in different species bases and with different transport kernels. In **FH04** the diffusion network tracks the third–generation quark doublet q_3 and the right–handed top (denoted by its left–handed conjugate t^c). The baryon–left combination is

FH04:
$$\mu_{B_L}(z) = \frac{1}{2} \left(1 + 2 \kappa_t + \kappa_b \right) \mu_{q_3}(z) - \frac{1}{2} \kappa_t \mu_{t^c}(z) ,$$
 (83)

where the κ_i are the standard transport coefficients of [44].

In **FH06**, the tracked species are the explicit chiral fields t_L , b_L , t_R (written as t^c for the left–handed conjugate), and the Higgs h (the subscript L is omitted in their notation). The corresponding definition reads

FH06:
$$\mu_{B_L}(z) = \frac{1}{2} \left(1 + 4 K_1^t \right) \mu_t(z) + \frac{1}{2} \left(1 + 4 K_1^b \right) \mu_b(z) - 2 K_1^t \mu_{t^c}(z) ,$$
 (84)

with K_1^a the transport kernels of [45]. We remind the reader that $\mu_{t_R} = -\mu_{t^c}$ by definition of the conjugated field. Equations (83) and (84) are equivalent after translating (μ_{q_3}, κ_i) into (μ_t, μ_b, K_1^a) according to the species basis used in each formalism.

5 Baryon asymmetry

During a first-order electroweak phase transition, bubbles of the broken phase nucleate and sweep through the symmetric plasma. We model a single planar wall moving along z with velocity v_w and width L_w , with the broken phase at z < 0 and the symmetric phase at z > 0. CP-violating interactions in the wall background create a chiral excess in front of the wall; weak sphalerons convert the left-handed baryon charge carried by quarks into net baryon number. The quantity that couples to weak sphalerons is the baryon-left chemical potential $\mu_{B_L}(z)$ defined earlier as a thermal-weight combination of the heavy-flavour potentials; only its CP-odd part enters.

We treat weak sphalerons as the slowest process in the problem. Accordingly, we first solve the diffusion/transport network for all non-baryonic species (with Γ_{ws} switched off) to obtain $\mu_{B_L}(z)$, and only in a second step do we evolve the baryon number using the sphaleron evolution equation to compute η_B . The rationale and accuracy of this two–step procedure are summarised in Box 5.1. A convenient starting point is the rate equation written in terms of the Chern–Simons (CS) chemical potentials,

$$\frac{dn_B}{dt} = n_f \Gamma_{ws} \left(-\mu_{\rm CS} + \mu_{\rm CS}^0 \right), \tag{85}$$

with $n_f = 3$ are the fermion families, $\Gamma_{ws} \sim \kappa \alpha_W^5 T$ is the weak sphaleron rate in the symmetric phase, and where $\mu_{\rm CS}$ is the response of the plasma to a change in CS number while $\mu_{\rm CS}^0$ encodes the chiral charge bias produced by transport. Under the standard hierarchy of rates (sphalerons are the slowest processes in the diffusion network) one can relate $\mu_{\rm CS} \propto n_B$ and express $\mu_{\rm CS}^0$ as a linear combination of left-handed quark and lepton chemical potentials; recasting the susceptibilities in terms of μ_{B_L} leads to the compact form used in transport studies,

$$\frac{dn_B}{dt} = -\frac{n_f}{2} \Gamma_{ws} (N_c \,\mu_{B_L} \, T^2 - A \, n_B), \tag{86}$$

Box 5.1: Computation of the baryon asymmetry

The computation of the baryon asymmetry can be approached in two conceptually different ways, depending on how the weak sphaleron processes are treated within the transport system, see [70, 71].

Two-step approach (standard method).

1. Solve the fluid network. One first determines the steady-state profiles of all particle densities (or chemical potentials) by solving the set of drift-diffusion-reaction equations,

$$0 = D_i n_i''(z) - v_w n_i'(z) - \sum_j \Gamma_{ij} [\text{linear combinations of } \mu_j(z)] + S_i(z),$$

with boundary conditions $n_i(\pm \infty) = 0$. In this step, the weak sphaleron processes are neglected under the assumption that they are the slowest reactions in the system.

2. Compute the baryon asymmetry. Once the fluid network is solved, the baryon asymmetry $n_B(z)$ is obtained by solving a separate diffusion equation,

$$0 = D_B n_B''(z) - v_w n_B'(z) - \Gamma_{ws}(z) \left[C_L \frac{\mu_L(z)}{T} + \kappa_B \frac{n_B(z)}{T^2} \right],$$

with $n_B(+\infty) = 0$. The final baryon-to-entropy ratio is extracted in the broken phase as $\eta_B = n_B(z \to -\infty)/s$.

One-step approach (fully coupled method). In this alternative formulation, the baryon density is included as a dynamical variable inside the fluid network itself. The system of equations becomes

$$\begin{cases} 0 = D_i \, n_i'' - v_w \, n_i' - \sum_j \Gamma_{ij}(\mu) \, + \, S_i(z), \\ 0 = D_B \, n_B'' - v_w \, n_B' - \Gamma_{ws}(z) \left(\mathcal{C}_L \frac{\mu_L}{T} + \kappa_B \frac{n_B}{T^2} \right), \end{cases}$$

In this case, the production and diffusion of the baryon asymmetry are solved *simultaneously* with all other species, rather than in a post-processing step. This fully coupled treatment is more demanding numerically but provides a self-consistent picture when the weak sphaleron rate is not hierarchically slower than the other reactions.

In this review, as in most of the literature, we adopt the two-step approach.

with $N_c = 3$ the number of colours and $A = 15/2^{19}$.

Passing to the wall frame and seeking a steady profile, $\partial_t \to -v_w \gamma_w \partial_z$, gives²⁰

$$\frac{dn_B}{dz} = \frac{n_f}{2v_w \gamma_w} \Gamma_{ws}(z) \Big(N_c \,\mu_{B_L}(z) \, T^2 - A \, n_B(z) \Big). \tag{87}$$

¹⁹In the symmetric phase with small chemical potentials and standard fast reactions (gauge interactions equalise components in each SU(2) multiplet and colour; quark Yukawas relate $\mu_u = \mu_q + \mu_h$, $\mu_d = \mu_q - \mu_h$; hypercharge neutrality is imposed), number-density asymmetries are linear in μ : $n_i = \chi_i \, \mu_i$ with SM susceptibilities. One finds three families $n_B = \frac{2n_f}{3} \, T^2 \, \mu_q \Rightarrow \mu_q = \frac{1}{2} \, n_B / T^2$, and, consistently with the same constraints, $\sum_f \mu_{\ell_f} = 3 \, n_B / T^2$. The weak-sphaleron "affinity" is $\sum_f (3\mu_{q_f} + \mu_{\ell_f}) = 9\mu_q + \sum_f \mu_{\ell_f} = \left(\frac{9}{2} + 3\right) n_B / T^2 = \frac{15}{2} \, n_B / T^2$. So then A = 15/2. For other details and the extension in the MSSM, see [34].

 $^{^{20}}$ In the standard EWBG reduction the baryon–left potential $\mu_{B_L}(z)$ is obtained from a genuine diffusion network for the microscopic species (quarks and Higgs), while the baryon density $n_B(z)$ is evolved by local weak–sphaleron kinetics as in (86). A separate diffusion term for n_B (e.g. $-\partial_z[D_B\,\partial_z n_B]$) is omitted because: (i) n_B , in this two step approach, has no independent carrier/current—its spatial transport is already encoded upstream in $\mu_{B_L}(z)$, so adding $D_B\,n_B''$ would double–count; (ii) the regime is reaction–limited—fast interactions set μ_{B_L} on wall scales while weak sphalerons act slowly and locally—so a first–order balance in z is the correct leading description; (iii) inside the broken phase $\Gamma_{ws} \to 0$, hence diffusion only reshuffles n_B without changing the frozen–in asymmetry n_B . If one insists on including diffusion consistently, its effect is higher order and negligible when $\Gamma_{ws} \gg D_B/L^2$ over the active layer of width L.

Sphalerons are suppressed inside the broken phase and active in front of the wall, their profile across the wall is discussed in the next subsection.

5.1 Weak sphaleron rate profile

The weak sphaleron rate, $\Gamma_{ws}(z)$, determines the efficiency of baryon number violation across the electroweak bubble wall. Its spatial dependence reflects the rapid change of the Higgs background h(z) between the symmetric and the broken phase.

Symmetric phase. In front of the wall, where $h(z) \simeq 0$, the sphaleron transitions are unsuppressed and the rate can be taken as a constant,

$$\Gamma_{ws}(z) \simeq \text{const} \times T, \qquad (z \gg 0),$$
 (88)

with $\Gamma_{\rm sph}$ obtained from lattice simulations of hot SU(2) gauge theory, including fermionic effects. The updated value is $\Gamma_{\rm sph} \simeq 8 \times 10^{-7} \, T$ (see Appendix F for details).

Broken phase. Behind the wall, where h(z) grows towards its vacuum expectation value, sphaleron transitions are exponentially suppressed because baryon number violation requires overcoming the sphaleron energy barrier $E_{\rm sph}(T)$. The general expression reads

$$\Gamma_{ws}^{\text{br}}(z) = \kappa T^4 e^{-E_{\text{sph}}(z)/T}, \tag{89}$$

where the exponent is controlled by the classical sphaleron energy [72],

$$E_{\rm sph}(T) = \frac{4\pi}{q} B\left(\frac{\lambda}{q^2}\right) h(z), \tag{90}$$

where $B(\lambda/g^2)$ is a dimensionless coefficient that parametrises the energy of the static SU(2) sphaleron solution, obtained from the classical field equations of the electroweak theory for a given ratio λ/g^2 , see [72]. For Standard Model parameters $(g \simeq 0.65, \lambda/g^2 \simeq 0.3)$, the numerical factor

$$\frac{4\pi}{q} B\left(\frac{\lambda}{q^2}\right) \simeq 36.57 \simeq 37,$$

where we used $B(\lambda/g^2) \simeq 1.89$, and this value has been extracted by interpolating the values that appear in Table II of [72]. The broken-phase suppression, $E_{\rm sph}(z)/T \simeq 37 \, h(z)/T$, thus follows the approximate form $e^{-37 \, h(z)/T}$.

Interpolating profile and normalisation. To connect the two regimes smoothly, it is convenient to define a dimensionless profile function $f_{\rm sph}(z)$ such that

$$\Gamma_{ws}(z) = \Gamma_{\rm sph} f_{\rm sph}(z), \qquad f_{\rm sph}(z) = \min \left[1, \frac{NT}{\Gamma_{\rm sph}} e^{-37h(z)/T} \right].$$
(91)

The prefactor N is fixed phenomenologically by imposing that sphaleron transitions in the broken phase decouple when $v(T_c)/T_c \simeq 1$, i.e. $\Gamma_{ws}^{\rm br}(T_c) \simeq H(T_c)$, with $H(T) = 1.66\sqrt{g_*}\,T^2/M_{\rm Pl}$ the Hubble rate in the radiation era [60]. Taking $g_* \simeq 106.75$, $T_c \simeq 150$ GeV, and $M_{\rm Pl} = 1.22 \times 10^{19}$ GeV gives²¹

$$H(T_c) \simeq 1.4 \times 10^{-18} \, T_c^2 \, \text{GeV}^{-1} \simeq 2.1 \times 10^{-16} T_c \longrightarrow N = \frac{H(T_c)/T_c}{e^{-37}} \simeq 1.7 \; .$$

Equation (91) therefore reproduces the standard phenomenological profile,

$$\Gamma_{ws}(z) = \Gamma_{\rm sph} \, \min\left(1, \frac{1.7 \, T}{\Gamma_{\rm sph}} \, e^{-37 \, h(z)/T}\right),\tag{92}$$

used in baryogenesis transport equations²².

²¹guarda bene le dimensionalità, non tornano

The factor 2.4 advocated in [49] might come from the assumption that $H(T_c)/T_c \simeq 10^{-17}$, as explicitly stated in [60], and taking the exponent to be 40, so that $N \simeq 2.4$.

Box 5.2: On the sign of the baryon asymmetry

The literature rarely states this explicitly, but once conventions are fixed, the sign of the predicted baryon asymmetry is no longer arbitrary. Conventions to fix include: (i) wall orientation (e.g. symmetric phase on the right, broken on the left, wall moving $+\hat{z}$), (ii) particle vs. antiparticle labelling (so that the CP eigenvalue CP = ± 1 refers to what we call "particle" or "antiparticle"), and (iii) the CP-odd vs. CP-even decomposition of the kinetic/transport equations such that the CP-violating phase $\theta_{\rm CP}(z)$ has a definite shape and sign for particles. With these choices set, the signs of all CP-odd sources are fixed, and the predicted baryon asymmetry must be positive to match the observed convention $\eta_B > 0$. If, under the same fixed conventions, a calculation yields $\eta_B < 0$, it describes an "antimatter universe" rather than ours. Flipping a model phase (e.g. $\theta \rightarrow -\theta$) flips the BAU sign and is not equivalent unless one simultaneously flips the baseline conventions (wall direction and particle/antiparticle labelling) everywhere in the pipeline.

5.2 Solving for the BAU

Now we turn in the solution of the Equation (87). Since it is linear, $n_B'(z) + p(z)n_B(z) = q(z)$, with $p(z) = \frac{n_f A}{2v_w \gamma_w} \Gamma_{ws}(z) \ge 0$ and $q(z) = \frac{n_f N_c}{2v_w \gamma_w} \Gamma_{ws}(z) \mu_{B_L}(z) T^2$, introducing the integrating factor $f(z) = \exp\left(\int^z p(z')dz'\right)$, one has $(n_B f)' = qf$. Integrating from z to $+\infty$ yields the exact solution

$$n_B(z) = n_B(+\infty) \exp\left[-\frac{An_f}{2v_w \gamma_w} \int_z^{+\infty} \Gamma_{ws}(z') dz'\right]$$

$$-\int_z^{+\infty} dz' \frac{n_f N_c}{2v_w \gamma_w} \Gamma_{ws}(z') \mu_{B_L}(z') T^2 \exp\left[-\frac{An_f}{2v_w \gamma_w} \int_z^{z'} \Gamma_{ws}(z'') dz''\right].$$
(93)

In EWBG, one imposes $n_B(+\infty) = 0$ (no asymmetry far ahead of the wall), so the first term vanishes and

$$n_B(z) = -\int_z^{+\infty} dz' \frac{n_f N_c}{2v_w \gamma_w} \Gamma_{ws}(z') \mu_{B_L}(z') T^2 \exp\left[-\frac{An_f}{2v_w \gamma_w} \int_z^{z'} \Gamma_{ws}(z'') dz''\right]. \tag{94}$$

The observable baryon asymmetry is the broken–phase value normalised to the entropy density²³ $s = \frac{2\pi^2}{45} g_* T^3$,

Baryon asymmetry generated

$$\eta_B \equiv \frac{n_B(-\infty)}{s} = -\frac{45n_f N_c}{4\pi^2 v_w \gamma_w g_* T} \int_{-\infty}^{+\infty} dz \, \Gamma_{ws}(z) \mu_{B_L}(z) \exp\left[-\frac{An_f}{2v_w \gamma_w} \int_{-\infty}^{z} \Gamma_{ws}(u) du\right], \quad (95)$$

with $g_* = 106.75$ in the SM. The structure of (95) makes the physics transparent: the kernel multiplying μ_{B_L} is the *source* that converts chiral charge into baryon number where sphalerons are active, while the exponential is the *washout* that erases n_B when the wall is too slow. For sufficiently large v_w the washout integral is small and part of the chiral excess diffuses into the broken phase, where $f_{\rm sph} \ll 1$, freezing in as the final η_B .

Note. With the conventions fixed in Box 5.2 phase assignments, spatial orientation (broken phase to the left, symmetric to the right), wall motion to +z in the plasma frame (and particle drift to -z in the wall frame), and the operational definition of μ_{B_L} and charge densities—the sign of the baryon asymmetry η_B is physical and unambiguous. In particular, the overall minus sign in front of Eq. (95), which is not found in general in the literature, follows from the correct solution. The same sign is found, for example, in Eq. (49) of [70].

 $^{^{23}}$ We summarise normalisation conventions used in the literature in Box 5.3.

Box 5.3: Photon vs. entropy normalisation of the baryon asymmetry

What is being compared? Observations often quote the baryon-to-photon ratio $n_B/n_{\gamma} \approx 6 \times 10^{-10}$ (see [73]), while in this work we use the entropy-normalised quantity $\eta_B \equiv n_B/s$ (see Eq. (95)). They are related by

$$\eta_B = \frac{n_{\gamma}}{s} \frac{n_B}{n_{\gamma}}.$$

For a relativistic plasma in kinetic equilibrium,

$$n_{\gamma} = \frac{2\zeta(3)}{\pi^2} T^3, \qquad s = \frac{2\pi^2}{45} g_{*s} T^3, \quad \rightarrow \quad \frac{n_{\gamma}}{s} = \frac{45\zeta(3)}{\pi^4} \frac{1}{g_{*s}} \simeq \frac{0.555}{g_{*s}}.$$

After e^+e^- annihilation (from CMB decoupling to today), the effective entropy degrees of freedom are

$$g_{*s} = 2 + \frac{7}{8} \times 3 \times 2 \left(\frac{T_{\nu}}{T_{\gamma}}\right)^3 = \frac{43}{11} \simeq 3.91,$$

with $T_{\nu}/T_{\gamma}=(4/11)^{1/3}$. Hence $n_{\gamma}/s\simeq 0.555/3.91\simeq 0.142$. Using $n_B/n_{\gamma}\simeq 6.1\times 10^{-10}$ one finds

$$\eta_B \simeq \left(\frac{n_{\gamma}}{s}\right) \frac{n_B}{n_{\gamma}} \simeq 0.142 \times 6.1 \times 10^{-10} \simeq 8.7 \times 10^{-11}.$$

This is the standard conversion between the two conventions; η_B remains conserved under entropy—conserving expansion.

5.3 Beyond a fixed wall velocity: a first-principles view

Although this is not implemented in BARYONET, we wanted to share some thoughts on the fact that the true baryon asymmetry is generally not well represented by $\eta_B(v_w)$ evaluated at a single, fixed wall velocity, as already pointed out in [51]. Since η_B can vary strongly with v_w , inhomogeneities in the system must be taken into account.

First-principles picture. Baryon number is produced locally at the moving wall and then transported or damped in the symmetric phase. If $v_n(\mathbf{x},t)$ is the *local normal velocity* of the wall element at position \mathbf{x} on the instantaneous wall surface $\Sigma(t)$, and $\eta_B^{\text{loc}}(v_n)$ is the 1D yield per unit volume swept by that element, the global asymmetry is

$$\eta_B = \frac{1}{V_{\text{tot}}} \int_{t_{\text{start}}}^{t_{\text{end}}} dt \int_{\Sigma(t)} dA \, v_n(\mathbf{x}, t) \, \eta_B^{\text{loc}}(v_n(\mathbf{x}, t)), \tag{96}$$

where V_{tot} is the total converted volume. Defining the volume-weighted distribution of wall speeds,

$$P(v) = \frac{1}{V_{\text{tot}}} \int_{t_{\text{start}}}^{t_{\text{end}}} dt \int_{\Sigma(t)} dA \, v_n(\mathbf{x}, t) \, \delta(v - v_n(\mathbf{x}, t)), \qquad \int_0^1 dv \, P(v) = 1, \tag{97}$$

Eq. (96) becomes

$$\eta_B = \int_0^1 dv \, P(v) \, \eta_B^{\text{loc}}(v), \tag{98}$$

showing that the relevant average is over the volume swept by the wall.

How to obtain P(v). A first-principles way is to simulate the coupled scalar-fluid system, $\partial_{\mu}T^{\mu\nu} = -\partial^{\nu}h \mathcal{F}(\partial h)$ and $\Box h + \partial V_{\text{eff}}(h,T)/\partial h + \mathcal{F}(\partial h) = 0$, with a chosen equation of state and friction model \mathcal{F} . Tracking the isosurface $h(\mathbf{x},t) = h_{\text{mid}}$ gives $v_n = -\partial_t h/|\nabla h|$; sampling it in spacetime yields P(v) directly.

6 Numerical implementation in BARYONET

Alongside this paper we release BARYONET, a modular Python code that takes a microscopic wall profile (masses and CP phase), solves the transport system, constructs the baryon–left chemical

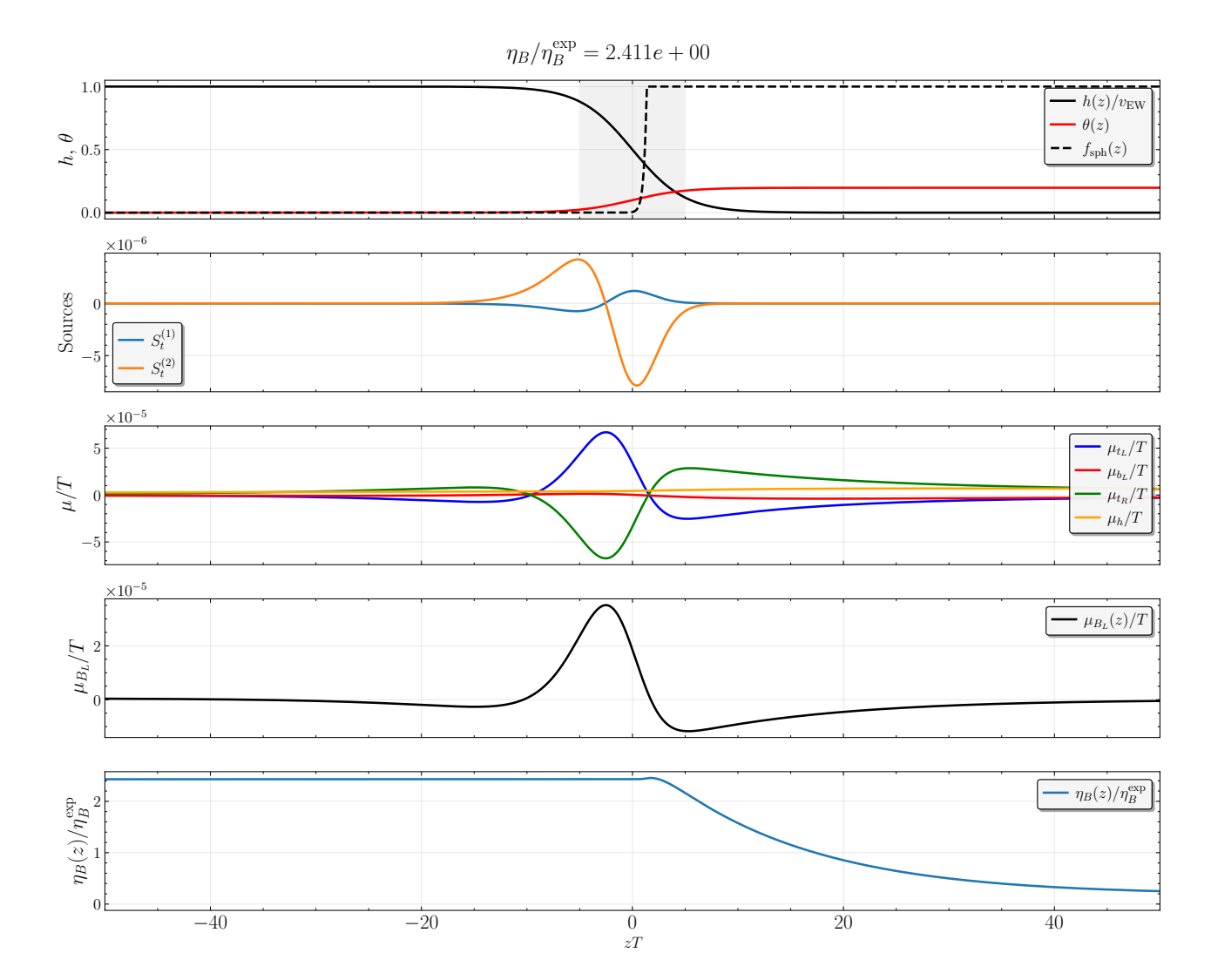


Figure 3: From wall profiles to η_B with BARYONET. Top row: Higgs profile $h(z)/v_{\rm EW}$, CP phase $\theta(z)$, and weak–sphaleron suppression $f_{\rm sph}(z)$. Gray shade region indicate $|z| < L_w$. Second row: CP sources $S_t^{(1)}(z)$ and $S_t^{(2)}(z)$ obtained from the WKB/gradient expansion and thermally averaged with the fluid weights. Third row: transport solution for μ_{t_L}/T , μ_{b_L}/T , μ_{t_R}/T , and μ_h/T . Fourth row: baryon–left chemical potential $\mu_{B_L}(z)/T$ constructed from the heavy-sector potentials with thermal weights. Last row: cumulative $\eta_B(z)/\eta_B^{\rm exp}$ versus zT; the plateau at negative zT is the frozen asymmetry (here $\eta_B/\eta_B^{\rm exp} \simeq 2.4$). Benchmark parameters as in (99).

potential $\mu_{B_L}(z)$, and integrates the weak–sphaleron equation to return the baryon asymmetry η_B . The workflow is purposely factorised: model inputs (profiles and interaction rates) are cleanly separated from universal thermal kernels and linear solvers. In practice one specifies the wall kinematics (v_w, L_w) , the thermal scale via $\xi = v_n/T_n$, the relevant Yukawas, and any model parameter controlling the CP phase; BARYONET then assembles the first–order system, solves it on a finite zT interval, and computes η_B . The package ships with ready–to–run benchmarks, plotting helpers, and scan utilities, and can be downloaded from the project page: BARYONET.

Figure 3 illustrates a representative end–to–end result for a benchmark in the real–singlet extension (xSM) with

BM1:
$$v_w = 0.1$$
, $L_w = 5$, $\xi = v/T = 1.0$, $y_t = 0.7$, $y_b = \lambda_h = 0.0$, $s_n/\Lambda = 0.2$, (99)

that will be a common benchmark point (BM) used in the following sections. Starting from the wall backgrounds, the code can evaluate the CP-odd sources, solves for the set of chemical potentials $\{\mu_{t_L}, \mu_{b_L}, \mu_{t_R}, \mu_h\}$, builds $\mu_{B_L}(z)$ using the thermal weights, and finally computes the cumulative $\eta_B(z)$ and its asymptotic value.

6.1 Code structure

BARYONET is organised to let users run end-to-end electroweak baryogenesis calculations with minimal friction: pick a physics model, choose a transport framework, run an example or notebook, and inspect results. This is the structure inside the main folder:

- models/ Minimal, ready-to-use model definitions (e.g. SM extensions) that expose wall/VEV/mass profiles and parameters through a common interface.
- transport_solver/ Core solvers for the transport network (CK, FH04, FH06, KV24). Each solver reads a model, sources, and interpolated transport functions, then returns profiles and observables.
- function_interpolators/ Pre-tabulated transport coefficients and lightweight loaders; provides consistent interpolants over $(x=m/T, v_w)$.
- Baryon_Asymmetry/ Utilities to compute η_B from solver outputs (two-step formulation).
- working_examples/ Small scripts showing canonical runs (choose model + solver, execute, write plots/tables). Ideal first contact for users.
- notebooks/ Guided, executable notebooks that mirror the examples but with narrative, sanity checks, and optional diagnostic plots.
- results/ Default output sink for profiles, figures, and text dumps.
- Estimates/ Back-of-the-envelope notebooks (rates, diffusion constants, orders of magnitude) used for setup and sanity checks.
- CP_sources_derivation/ Symbolic derivations of CP-violating sources (notebook + notes) underpinning the solver source terms.
- literature/ Reproductions and utilities tied to specific papers (CK_paper2020 [49], FH04_paper2011 [47], FH06_paper2006 [45, 46], KV24_paper2024 [51]) with notebooks and scripts.
- utils/ Shared helpers for plotting, logging, I/O, and configuration to keep user scripts concise and uniform.
- tests/ Quick regression tests covering solvers, interpolators, and BAU assembly; useful to validate local installs.

In practice, a user selects a model from models/, pairs it with a solver in transport_solver/, ensures the required tables are available via function_interpolators/, and runs one of the working_examples/ or notebooks/. Outputs are written to results/, while utils/ and tests/ support reproducible, checkable runs without cluttering user code.

Inside the main folder, the user can find BARYONET_installation_guide.pdf, which provides installation instructions and a brief user manual for navigating BARYONET.

6.2 Numerical values of the parameters

In this review, in order to validate BARYONET, we will use values of the parameters and rates commonly used in the literature, but since we realised that most of them were decades old, we redid all the estimations that has been done, or review the available value that are present in the literature and updated the values. These are presented in Table 2.

Interaction rates							
Interaction name	Rates used in the literature [44, 45, 48, 49]	Previous update from [50]	Last update (this work)				
Top Yukawa rate	$\widehat{\Gamma}_y^t \simeq 4.2 \times 10^{-4} T$	$\widehat{\Gamma}_y^t \simeq 3 \times 10^{-2} T$	$\widehat{\Gamma}_y^t \simeq 10^{-2} T$				
Top Helicity flipping	$\widehat{\Gamma}_m^t \simeq \frac{m_t^2}{63T}$	$\widehat{\Gamma}_m^t \simeq \frac{0.79m_t^2}{T}$	$\widehat{\Gamma}_m^t \simeq \frac{0.26m_t^2}{T}$				
Higgs Yukawa rate	$\widehat{\Gamma}_m^h \simeq \frac{m_W^2}{50T}$	$\widehat{\Gamma}_m^h \simeq rac{m_W^2}{25T}$	$\widehat{\Gamma}_m^h \simeq \frac{1.5m_W^2}{T}$				
W boson rate	$\widehat{\Gamma}_W \simeq \widehat{\Gamma}_{\mathrm{tot}}^h$	"	"				
Strong sphaleron	$\Gamma_{ss} \simeq 4.9 \times 10^{-4} T$	$\Gamma_{ss} \simeq 8.7 \times 10^{-3} T$	$\Gamma_{ss} \simeq 2.7 \times 10^{-3} T$				
Weak sphaleron	$\Gamma_{ws} \simeq 10^{-6} T$	$\Gamma_{ws} \simeq 6.3 \times 10^{-6} T$	$\Gamma_{ws} \simeq 8 \times 10^{-7} T$				
Diffusion constants							
Quarks	$D_q \simeq 6/T$	$D_q \simeq 7.4/T$	$D_{q_L} \simeq \frac{7.1}{T}, D_{q_R} \simeq \frac{7.6}{T}$				
Higgs	$D_h \simeq 20/T$	"	$D_h \simeq 14/T$				
Leptons	(see [29, 30] and App. C)	$D_{l_R} \simeq \frac{490}{T}, D_{l_L} \simeq \frac{90}{T}$	$D_{l_R} \simeq \frac{412}{T}, D_{l_L} \simeq \frac{100}{T}$				
Couplings							
Strong int.	$\alpha_s \simeq 1/7$	$\alpha_s(m_z) \simeq 0.1179$					
Weak int.	$\alpha_w \simeq 1/30$	$\alpha_w(m_z) \simeq 0.0338$					
Weinberg angle	$\tan \theta_W \simeq 0.29$	$\tan \theta_W \simeq 0.302$					

Table 2: Representative quantities used in solving the diffusion network, old and updated values. For details regarding diffusion constants, see App. C, for the Yukawa mediated relaxation rate see App. D and E, and for sphalerons rate see App. F.

7 Results & comparison with the literature

In this section, we present the numerical results obtained with BARYONET and benchmark them against representative calculations in the electroweak baryogenesis literature. Our goal, in this section, is validation, not novelty: we align conventions, match wall profiles and effective rates, and then reproduce published trends and normalisations within the stated frameworks (FH04, FH06, CK/KV24). Unless stated otherwise we report the entropy–normalised asymmetry $\eta_B = n_B(-\infty)/s$ and often show the ratio $\eta_B/\eta_B^{\rm obs}$ (with $\eta_B^{\rm obs} \simeq 8.7 \times 10^{-11}$) to make comparisons robust to unit choices.

Each subsection follows a uniform template: (i) a concise description of the physics setup and inputs (wall profiles, rates, solver options), (ii) the scan strategy and target observables, and (iii) a side-by-side comparison with the literature. For full reproducibility, we provide the exact paths to the result files used in each figure, so plots can be regenerated directly from the repository. The subsection titles coincide with the model names used in the code (e.g. classes under models/), enabling a one-to-one mapping between text and implementation.

7.1 ModelIndependent

A clean way to expose the ingredients of electroweak baryogenesis without committing to a specific ultraviolet completion is to work with a *model-independent* ansatz for the top quark mass across the wall, long used in the EWBG literature (see, e.g., [44, 47, 48]). We take

$$m_t(z) = y_t \,\phi(z) \,e^{i\Theta_t(z)} \,, \tag{100}$$

where the real background $\phi(z)$ and the CP-violating phase $\Theta_t(z)$ are smooth kinks of width L_w that interpolate between the symmetric and broken phases²⁴

$$\phi(z) = \frac{\phi_c}{2} \left(1 - \tanh \frac{z}{L_w} \right), \tag{101}$$

$$\Theta_t(z) = \frac{\Delta\Theta_t}{2} \left(1 - \tanh\frac{z}{L_w} \right),\tag{102}$$

controlled by the wall width L_w and the total phase excursion $\Delta\Theta_t$. This choice isolates the two macroscopic sources that matter for charge transport—gradients of the mass modulus and of the CP phase—while keeping the rest of the computation agnostic about how Θ_t arises (two-doublet, singlet, higher-dimensional operators, etc.). In practice one scans over the wall parameters (v_w, L_w) and the thermodynamic strength, and for each point determines the minimal phase excursion $\Delta\Theta_t$ that reproduces the observed baryon asymmetry. The transport sector delivers $\mu_{B_L}(z)$, the weak-sphaleron kernel converts it into $n_B(z)$, and the freeze-in value gives η_B ; this pipeline is the same that will be used for all concrete models later on.

Figure 4 illustrates a typical outcome in the FH04 closure: for several wall thicknesses (quoted as L_wT_c) one obtains the required $\Delta\Theta_t$ as a function of $\xi=\phi_c/T_c$. The plot is best read as a "response curve" of the charge–transport engine: thicker walls and weaker transitions demand larger CP–phase excursions, while thinner walls (or stronger transitions) reduce the burden on CP violation. The main virtue of this benchmark is pedagogical: it makes explicit which microscopic inputs the code uses (wall kinematics, scalar and phase profiles) and how they flow into the final observable η_B , independently of any detailed microphysics. This plot can be reproduced from the notebook literature/FH04_paper2011/FH04_scans_minimal.ipynb.

7.2 xSM

In the real-singlet extension of the SM (xSM), a concrete realisation of a space-dependent complex top mass is provided by the dimension-five operator $i(s/\Lambda) \bar{Q}_3 H t_R$, which induces a phase wherever the singlet s acquires a wall profile. In the wall background the effective top mass term reads

$$y_t h(z) \bar{t}_L \left(1 + i \frac{s(z)}{\Lambda} \right) t_R + \text{h.c.}, \tag{103}$$

implying the magnitude-phase decomposition

$$m_t(z) = y_t h(z) \sqrt{1 + \frac{s^2(z)}{\Lambda^2}},$$
 (104)

$$\Theta_t(z) = \arctan\left(\frac{s(z)}{\Lambda}\right).$$
(105)

We model the background with opposite–kink profiles for Higgs and singlet²⁵,

$$h(z) = \frac{v_n}{2} \left(1 - \tanh \frac{z}{L_w} \right), \tag{106}$$

$$s(z) = \frac{w_n}{2} \left(1 + \tanh \frac{z}{L_m} \right),\tag{107}$$

so that $\Theta_t(z)$ interpolates smoothly across the wall. Given $(v_w, L_w, v_n, w_n, \Lambda)$, the transport system yields $\mu_{B_L}(z)$, which feeds the baryon equation for η_B .

²⁴Throughout this work we adopt the convention that the symmetric phase lies to the right of the wall (z > 0) and the broken phase to the left (z < 0). This orientation differs from that used in parts of the literature; physical results are unaffected as long as boundary conditions and sign conventions are implemented consistently.

 $^{^{25}}$ In a genuine two–field background (e.g. Higgs h and singlet s) the wall profiles need not share the same thickness: one should in principle allow for $L_h \neq L_s$, possible relative shifts in the wall centres, (see, e.g., [66] for an explicit treatment). These differences modify the spatial gradients that source CP violation and can quantitatively affect transport. To simplify the analysis here, we adopt the assumption $L_h = L_s \equiv L_w$ and take the induced mass phase to follow a single smooth profile $\Theta_t(z)$.

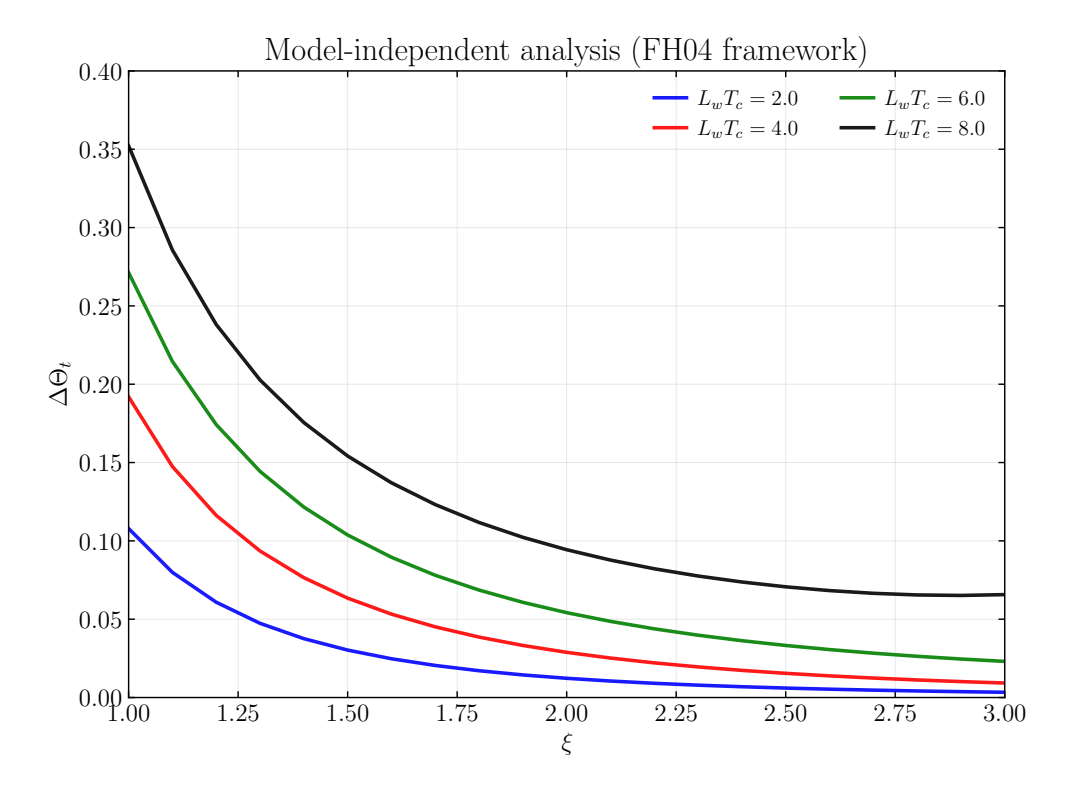


Figure 4: Model-independent benchmark in the FH04 framework: minimal CP-phase excursion $\Delta\Theta_t$ required to match the observed η_B as a function of ξ , shown for several wall thicknesses $L_wT_c \in \{2,4,6,8\}$. Curves are generated by solving the transport equations for each (ξ, L_wT_c) , constructing $\mu_{B_L}(z)$, and using an overshoot method to find the phase reproducing the BAU's observed value. Benchmark parameters: $v_w = 0.01$, $y_t = 0.7$, $y_b = 0.0$.

Following [49], we use this setup to benchmark frameworks and sources. In Fig. 5, we compare (i) CK fluid scheme versus the FH06 equations, and (ii) two closely related CPV sources: the spin-s source (identifying chirality with the spin eigenstate along \hat{z}) and the helicity-h source (identifying chirality with helicity), as you can see in Appendix A.1. For small wall velocities, all curves agree—as expected from the common small- v_w limit. At larger v_w , FH06 exhibits a strong suppression as v_w approaches the sound speed $c_s = 1/\sqrt{3}$, while the improved scheme degrades smoothly toward $v_w \to 1$. The difference between spin- and helicity-based sources is modest because the two bases coincide in the massless limit relevant ahead of the wall. We believe that in [49] the "h" curve appears to have been drawn with $k_0 \to 1$; to disentangle these effects we show both source choices with the full k_0 and with $k_0 \to 1$ for reference.

7.3 xSMv2

In this subsection, we introduce a refined version of the xSM setup that makes the link between $microscopic\ couplings$ and $macroscopic\ wall\ properties$ explicit—most notably the wall width L_w -in the spirit of Ref. [47]. Concretely, we consider the SM augmented by a real scalar singlet with a Z_2 -symmetric potential, and we follow the finite-temperature dynamics (effective potential, phase structure, nucleation, and bubble-wall profiles) closely along the lines of Ref. [47]. This construction provides a transparent mapping from the portal and singlet self-couplings to thermal parameters such

 $^{^{26}}$ In the FH06 setup, the transport is treated as a small- v_w diffusion problem in a nearly static plasma. As the wall approaches the sound speed $c_s=1/\sqrt{3}$ from below (deflagration regime), hydrodynamics predicts the build-up of a compressed "sonic layer" (a sonic boom) in front of the wall. In that layer, the effective diffusion length ahead of the wall shrinks to zero, so the CP-odd left charge cannot outrun the interface and μ_{B_L} (hence the BAU) is strongly suppressed. Because FH06 linearises in v_w and neglects the boosted background flow, this physical suppression manifests as a sharp drop near $v_w \simeq c_s$. The CK implementation uses boosted formulations to keep a smooth v_w dependence and show a gradual decrease instead of a spurious cusp. For a hydrodynamic discussion of the sonic layer and its impact on charge transport, see [62].

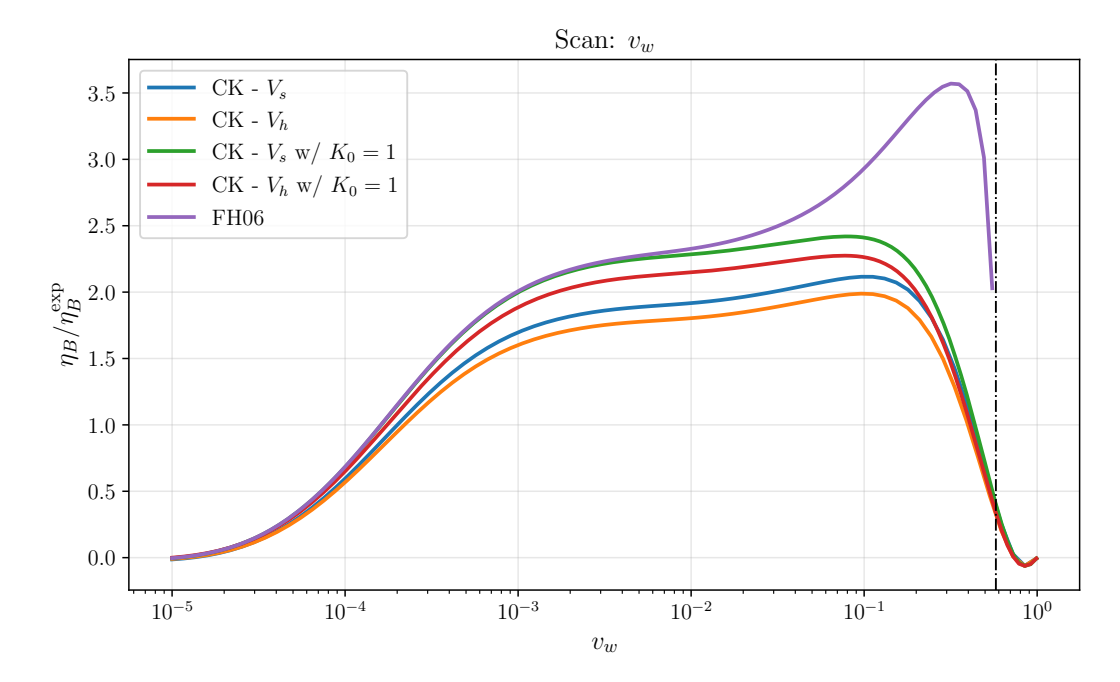


Figure 5: xSM benchmark, $\eta_B/\eta_B^{\text{obs}}$ versus v_w . Blue: scheme with spin-s source (CK- V_s); Orange: scheme with helicity-h source (CK- V_h); Green: CK- V_s with $K_0 = 1$; Red: CK- V_h with $K_0 = 1$; Purple: FH06 with the spin-s source. Curves coincide at small v_w , while FH06 drops near c_s and the scheme remains smooth; the s-vs-h difference is small.

as T_c , $\xi \equiv v(T)/T$, and, crucially for transport, the wall thickness L_w that enters the semiclassical sources and diffusion network. At mean–field level, and around the critical temperature, the scalar potential can be written as

$$V(h, s, T) = \frac{\lambda_h}{4} \left[h^2 - v_c^2 + \frac{v_c^2}{w_c^2} s^2 \right]^2 + \frac{\kappa}{4} s^2 h^2 + \frac{1}{2} (T^2 - T_c^2) (c_h h^2 + c_s s^2), \tag{108}$$

with $\kappa \equiv \lambda_m - 2\lambda_h v_c^2/w_c^2$. For $\kappa > 0$ the potential exhibits a tree-level barrier and, at $T = T_c$, degenerate minima at $(h, s) = (v_c, 0)$ and $(0, \pm w_c)$. The thermal coefficients are

$$c_h = \frac{1}{48} \left(9g^2 + 3g'^2 + 12y_t^2 + \lambda_h (24 + 4v_c^2/w_c^2) + 2\kappa \right), \tag{109}$$

$$c_s = \frac{1}{12} \left(\lambda_h \left(3(v_c^2/w_c^2)^2 + 4v_c^2/w_c^2 \right) + 2\kappa \right), \tag{110}$$

and electroweak breaking below T_c is ensured when

$$\frac{c_h}{c_s} > \frac{w_c^2}{v_c^2}. (111)$$

Standard relations then follow

$$T_c^2 = \frac{\lambda_h}{c_h} (v_0^2 - v_c^2), \qquad m_h^2 = 2\lambda_h v_0^2, \qquad m_s^2 = \frac{1}{2} \kappa v_0^2 + \lambda_h (v_0^2 - v_c^2) \left(\frac{v_c^2}{w_c^2} - \frac{c_s}{c_h} \right). \tag{112}$$

Across the wall, we use kink profiles of common thickness L_w ,

$$h(z) = \frac{v_c}{2} \left[1 + \tanh\left(\frac{z}{L_w}\right) \right], \qquad s(z) = \frac{w_c}{2} \left[1 - \tanh\left(\frac{z}{L_w}\right) \right], \tag{113}$$

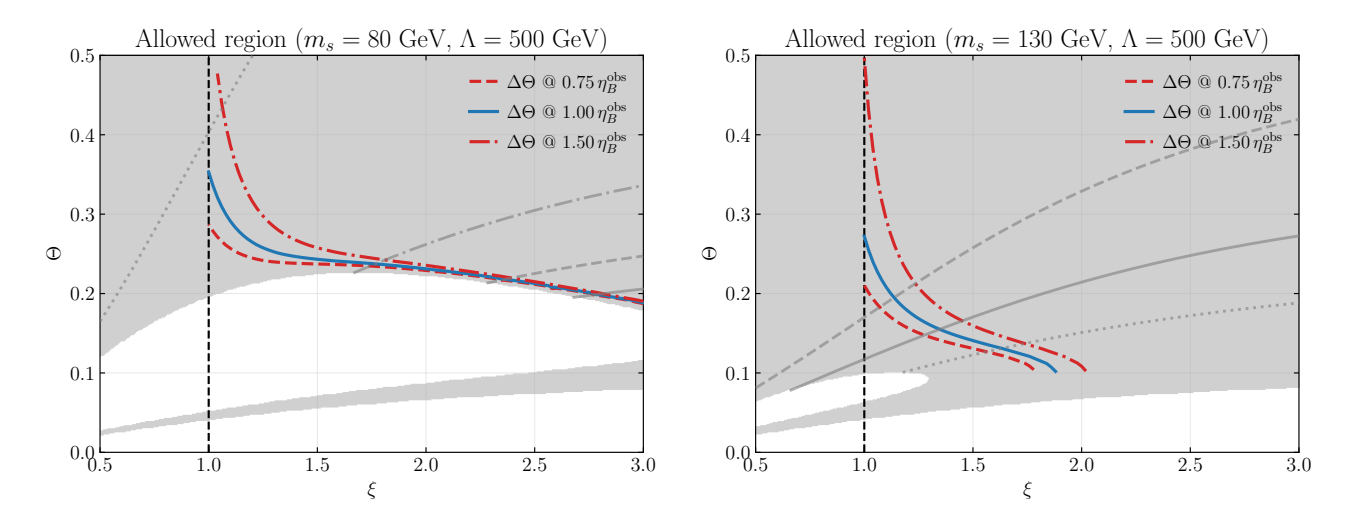


Figure 6: xSMv2 benchmark scans ($m_h = 120 \text{ GeV}$, $\Lambda = 500 \text{ GeV}$). Curves show the CP-phase excursion $\Delta\Theta_t$ required to obtain $0.75\eta_B^{\text{obs}}$ (dash-dotted), η_B^{obs} (solid), and $1.5\eta_B^{\text{obs}}$ (dashed) as a function of $\xi = v_c/T_c$. Left: $m_s = 80 \text{ GeV}$. Right: $m_s = 130 \text{ GeV}$. The shaded band indicates the region required for the FOPT ($L_w T_c > 0$ and $\lambda_m < 2\pi$); the vertical line marks $\xi = 1$, below which active sphalerons would erase the asymmetry. The grey lines (dotted above left, dot-dashed, dashed, solid, dotted below right) correspond to lines with fixed $\lambda_m = 0.25, 0.5, 0.75, 1, 1.5$, respectively.

interpolating between $(0, w_c)$ and $(v_c, 0)$. A thin–wall estimate obtained by minimising the one–dimensional action gives²⁷

$$L_w^2 \simeq \frac{2.7}{\kappa} \frac{v_c^2 + w_c^2}{v_c^2 w_c^2} \left(1 + \frac{\kappa w_c^2}{4\lambda_h v_c^2} \right). \tag{115}$$

CP violation is communicated to the top sector by the dimension–five operator

$$\frac{s}{f} H \bar{Q}_3 \left(a + ib \gamma_5 \right) t + \text{h.c.}, \tag{116}$$

which induces a space-dependent complex top mass,

$$m_t(z) = |m_t(z)| e^{i\Theta_t(z)}, \qquad \Theta_t(z) \simeq \frac{\Delta\Theta_t}{2} \left[1 + \tanh\left(\frac{z}{L_w}\right) \right], \qquad \Delta\Theta_t \simeq \frac{b}{y_t} \frac{\Delta s}{f},$$
 (117)

with $\Delta s \approx w_c$ for the profiles above. Larger $\Delta \Theta_t$ and stronger transitions (larger $\xi \equiv v_c/T_c$) enhance the CP-odd source, whereas thicker walls reduce gradients and suppress transport.

$$h(z) = \frac{v_c}{\sqrt{2}} \sin\left(\frac{\pi}{4} \left(1 + \tanh\left(\frac{z}{L_w}\right)\right)\right), \qquad s(z) = \frac{w_c}{\sqrt{2}} \cos\left(\frac{\pi}{4} \left(1 + \tanh\left(\frac{z}{L_w}\right)\right)\right), \tag{114}$$

where, at the critical temperature, one can see that the wall tension splits into a kinetic piece and a potential piece and can be computed exactly

$$S_E(L_w) = S_{E, \text{kin}}(L_w) + S_{E, \text{pot}}(L_w), \qquad S_{E, \text{kin}} = \frac{\alpha}{L_w} (v_c^2 + w_c^2), \quad S_{E, \text{pot}} = \beta \kappa v_c^2 w_c^2 L_w,$$

with

$$\alpha = \frac{\pi^2}{48}, \qquad \beta = \frac{1}{32} \Big(\gamma_E - \operatorname{Ci}(2\pi) + \ln(2\pi) \Big),$$

where γ_E is the Euler-Mascheroni constant and Ci the cosine integral. Minimizing S_E gives the thin-wall estimate

$$L_w^2 = \frac{\alpha}{\beta} \frac{v_c^2 + w_c^2}{\kappa v_c^2 w_c^2} \simeq 2.7 \frac{v_c^2 + w_c^2}{\kappa v_c^2 w_c^2},$$

so the numerical prefactor $\alpha/\beta \simeq 2.699$. Compared with the formula in the main text, the parametric dependence is not identical. For completeness and reproducibility, however, our analysis implements the wall–width expression exactly as written in [47] when benchmarking their figures, even though our rederivation indicates a likely typo/inconsistency in its parametric scaling.

²⁷Using the kink profiles h(z), s(z) modelled as

In BARYONET one fixes $(v_w, L_w, v_c, w_c, \lambda_h, \kappa)$ and the spurion parameters (b/f), builds $h(z), s(z), \Theta_t(z)$, evaluates the CP sources and collision blocks, solves the transport system to obtain $\mu_{B_L}(z)$, and finally computes η_B . We present scans in $\Delta\Theta_t$, and ξ comparing $\eta_B/\eta_B^{\rm obs}$ to the qualitative trends in Ref. [47]: increasing ξ or m_s lowers the $\Delta\Theta_t$ needed for successful baryogenesis (until washout reappears near $\xi \simeq 1$); thicker walls v_w demand larger phases.

7.4 Higgs6Model

As a minimal one-field benchmark, we follow Ref. [45] and augment the SM Higgs potential with a stabilising dimension-six operator. At finite temperature, the background is captured by

$$V(\phi) = -\frac{\mu^2}{2}\phi^2 + \frac{\lambda}{4}\phi^4 + \frac{1}{8L^2}\phi^6, \qquad (118)$$

where the ϕ^6 term allows $\lambda < 0$ while keeping the potential bounded, yielding a tree-level barrier and a strong first-order transition over broad regions of parameter space. Typical walls are thick in the WKB sense, $3 \lesssim L_w T_c \lesssim 16$, and we model the profile by a kink,

$$\phi(z) = \frac{v_c}{2} \left(1 - \tanh \frac{z}{L_{co}} \right), \tag{119}$$

interpolating from the symmetric to the broken phase. CP violation is introduced by dressing the top Yukawa through the lowest–dimensional operator,

$$\frac{x_t}{M^2} (\Phi^{\dagger} \Phi) \Phi \, \bar{t}_R Q_3 + y_t \Phi \, \bar{t}_R Q_3 + \text{h.c.}, \tag{120}$$

so that inside the wall, the top mass is complex,

$$m_t(z) = |m_t(z)| e^{i\Theta_t(z)}, \qquad \tan\Theta_t(z) \simeq \sin\varphi_t \frac{\phi^2(z)}{2M^2} \left| \frac{x_t}{y_t} \right|,$$
 (121)

and the total phase excursion $\Delta\Theta_t$ controls the CP-odd source. For transport, we implement the diffusion network of Ref. [45] and keep the standard four species $\{t,b,t_c,h\}$ with the baryon-left potential built as in FH06, see Eq. (84). We then solve the FH06 moment equations with the full z-dependence of the thermal averages and finite W scatterings, and convert $\mu_{B_L}(z)$ into η_B through the weak-sphaleron equation. The left panel of Fig. 7 reproduces the qualitative behaviour of line (a) in Fig. 6 of Ref. [45]: for fixed (ξ, L_w) the asymmetry grows from very small v_w , flattens for intermediate speeds, and eventually decreases as transport becomes inefficient.

Parameter choice. Following Ref. [45], the parameters of the Higgs6Model potential are selected to ensure a strong first-order electroweak phase transition. The effective operator scale L controls the ϕ^6 deformation and the height of the tree-level barrier: smaller L values strengthen the transition but eventually spoil perturbativity or EFT validity. For each (m_h, L) pair, the critical temperature T_c and the corresponding Higgs expectation value v_c are computed, and the ratio $\xi \equiv v_c/T_c$ is required to exceed unity (typically $\xi \gtrsim 1.1$) to avoid baryon washout in the broken phase. Viable regions are found for $5 \lesssim L/T_c \lesssim 8.5$ with $\lambda < 0$, where a stable, bounded potential and $\xi > 1$ coexist.

7.5 TwoHDM

The two-Higgs-doublet model (2HDM) augments the SM with two $SU(2)_L$ doublets H_1 , H_2 and allows for a soft, explicitly CP-violating mixing. Following Ref. [46], we start from the neutral-field potential (soft Z_2 breaking by $\mu_3^2 e^{i\phi} H_1^{\dagger} H_2$) and include the one-loop Coleman-Weinberg and thermal pieces,

$$V_{\text{eff}}(h_1, h_2, \theta; T) = V_0 + V_1 + V_{\text{CT}} + V_1^T, \tag{122}$$

where $H_1^0 = h_1 e^{-i\theta_1}$, $H_2^0 = h_2 e^{+i\theta_2}$ and $\theta \equiv \theta_1 + \theta_2$. Minimizing $V_{\rm eff}$ at the critical temperature T_c gives the broken–phase vevs $v_1 \equiv \langle h_1 \rangle_{T_c}$, $v_2 \equiv \langle h_2 \rangle_{T_c}$ and the CP phase $\theta_{\rm brk}$, degenerate with the symmetric minimum $(0,0,\theta_{\rm sym})$. The standard strength parameter and valley direction are

$$\xi \equiv \frac{v_c}{T_c}, \qquad v_c \equiv \sqrt{2(v_1^2 + v_2^2)}, \qquad \tan \beta_T \equiv \frac{v_2}{v_1}\Big|_{T_c}.$$
 (123)

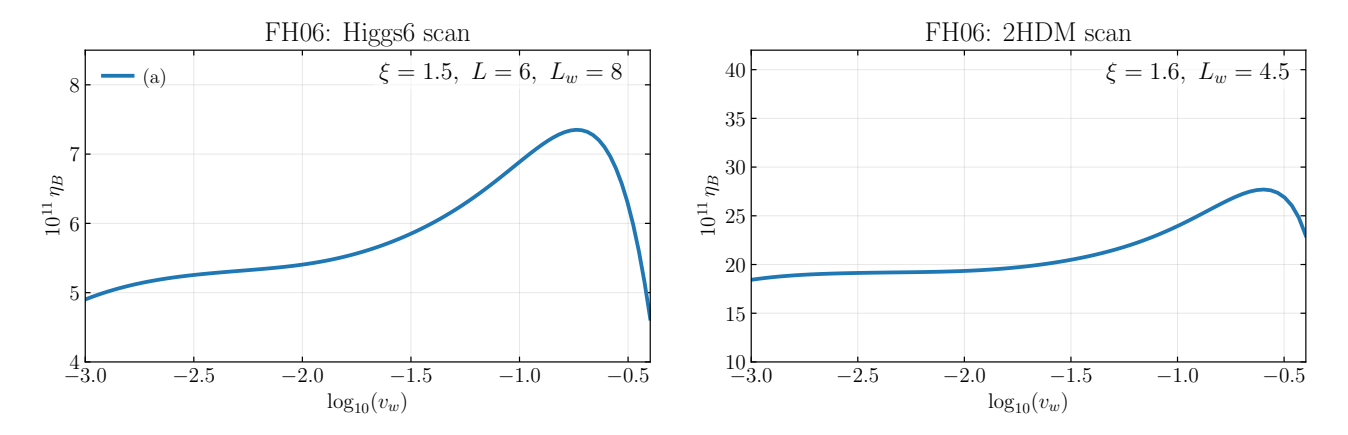


Figure 7: FH06 scans. Left—Higgs6Model (based on [45]): baryon asymmetry η_B versus wall velocity v_w for representative (ξ, L_w) , obtained with the FH06 diffusion network and full z-dependent thermal averages; the curve corresponds to the "no approximations" case (line (a) in Fig. 6 of [45]). Right—2HDM (next subsection, based on [46]): analogous scan using the FH06 implementation and the two-doublet wall/phase profiles of Ref. [46]. Quantities in the top right corner are in units of T_c .

Along the light "valley" direction h the wall is well approximated by a kink of thickness L_w determined by the barrier height V_b at T_c

$$h(z) \simeq \frac{v_c}{2} \left[1 - \tanh\left(\frac{z}{L_w}\right) \right], \qquad L_w \simeq \sqrt{\frac{v_c^2}{8 V_b}}.$$
 (124)

Projecting the vevs onto the two doublets along the valley gives $h_1(z) = h(z) \cos \beta_T$ and $h_2(z) = h(z) \sin \beta_T$. The top and bottom mass moduli (the only quantities the transport tables need) follow directly

$$m_t(z) = y_t h_2(z) = \frac{y_t}{\sqrt{2}} h(z) \sin \beta_T, \qquad m_b(z) = y_b h_1(z) = \frac{y_b}{\sqrt{2}} h(z) \cos \beta_T,$$
 (125)

so $m_{t,b}^2(z)$ and their first/second z-derivatives are fixed once (v_c, T_c, L_w, β_T) are known. The relative CP phase varies across the wall; we use the kink ansatz

$$\theta(z) = \theta_{\rm brk} - \frac{\Delta \theta}{2} \left[1 + \tanh\left(\frac{z}{L_w}\right) \right], \qquad \Delta \theta \equiv \theta_{\rm brk} - \theta_{\rm sym}.$$
 (126)

The phase that actually sources the transport is the top phase

$$\Theta(z) \equiv \theta_t(z) = \frac{\theta(z)}{1 + \tan^2 \beta_T}.$$
 (127)

For the diffusion network, we implement the moment equations of Ref. [46]; in the code, this option is labelled FH06for2HDM. A representative result is shown in the right panel of Fig. 7: we reproduce the qualitative trends reported in Fig. 6 of [46]—larger ξ (stronger transitions) and moderate v_w enhance the signal, while thicker walls reduce it.

8 Higher-moment analysis

In this subsection, we streamline the higher–moment system into a compact, *inverted* form that is convenient for both analysis and numerics. We follow the structure of Sec. 3.2 in Ref. [51], adapting the notation to our conventions. For each species, we assemble the CP-odd moment variables into $w(z) = (\mu, u_1, u_2, \dots, u_{\ell-1})^{\top}$. Stacking the ℓ equations (one for μ and $\ell-1$ for moments), the system

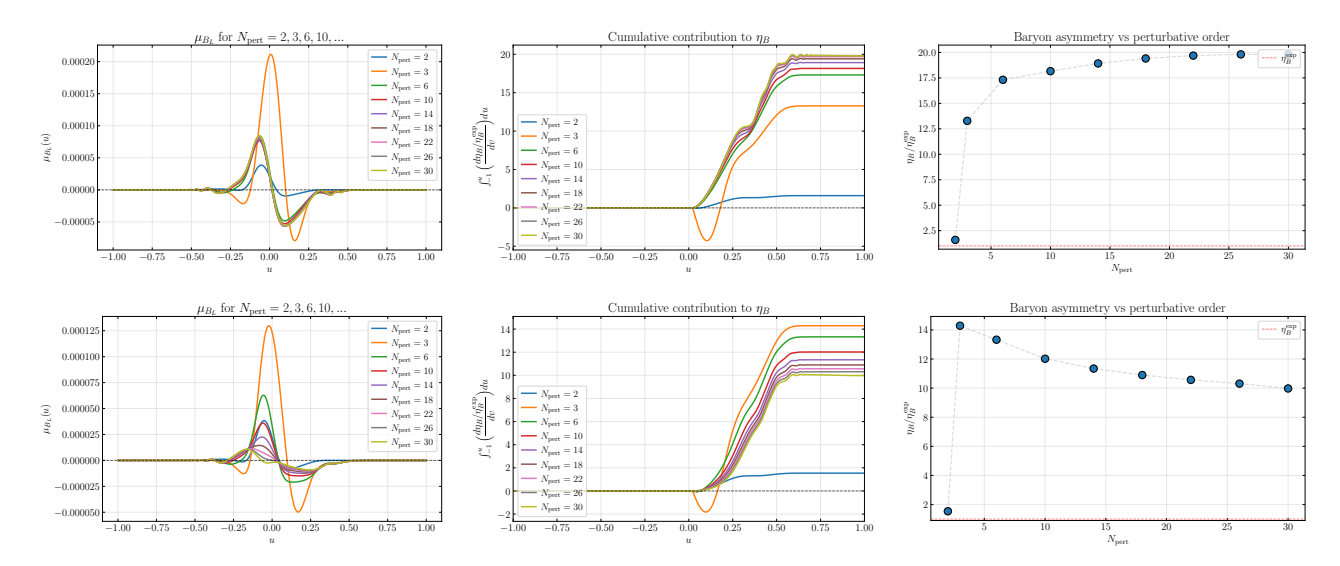


Figure 8: Higher-moment convergence and truncation effects. Top row (constant-R closure): (left) $\mu_{B_L}(u)$ for $N_{\text{PERT}} = 2, 6, \ldots, 30$; (middle) cumulative BAU $\int_{-1}^{u} (d\eta_B/\eta_B^{\text{exp}}) dv$; (right) $\eta_B/\eta_B^{\text{exp}}$ versus N_{PERT} . Bottom row (variance truncation): same panels, demonstrating earlier stabilisation and reduced spread. The stronger drop when going from $N_{\text{PERT}} = 2$ to $N_{\text{PERT}} \geq 6$ is evident in our data, while the overall convergence pattern and the stability of the 2+4k sequence agree with the findings of Ref. [51].

takes the form as in Eq. (52) with A and B now $\ell \times \ell$ matrices of the following form²⁸

$$A = \begin{pmatrix} -D_{1} & 1 & 0 & \cdots & 0 \\ -D_{2} & 0 & 1 & \cdots & 0 \\ \vdots & \vdots & \ddots & \ddots & \vdots \\ -D_{\ell-1} & 0 & \cdots & 0 & 1 \\ -D_{\ell} & R_{1} & \cdots & R_{\ell-2} & R_{\ell-1} \end{pmatrix}, \qquad B = (\partial_{z}m^{2}) \begin{pmatrix} Q_{1}v_{w}\gamma_{w} & 0 & 0 & \cdots & 0 \\ Q_{2}v_{w}\gamma_{w} & \bar{R} & 0 & \cdots & 0 \\ Q_{3}v_{w}\gamma_{w} & 0 & 2\bar{R} & \cdots & 0 \\ \vdots & \vdots & \ddots & \ddots & \vdots \\ Q_{\ell}v_{w}\gamma_{w} & 0 & 0 & \cdots & (\ell-1)\bar{R} \end{pmatrix},$$

$$(128)$$

and vector sources/collisions \mathcal{S}_{ℓ} , $\delta \mathcal{C}_{\ell}$ given component—wise by the CP-odd semiclassical source (built from $Q_{\ell}^{\infty}, Q_{\ell}^{9}$) and by the moment—reduced collision integrals.

It is useful, especially numerically, to write explicitly the inverse matrix of the matrix A, which reads

$$A^{-1} = \frac{1}{D_{\ell}} \begin{pmatrix} R_{1} & R_{2} & \cdots & R_{\ell-1} & -1 \\ R_{1}D_{1} & R_{2}D_{1} & \cdots & R_{\ell-1}D_{1} & -D_{1} \\ \vdots & \vdots & \ddots & \vdots & \vdots \\ R_{1}D_{\ell-1} & R_{2}D_{\ell-1} & \cdots & R_{\ell-1}D_{\ell-1} & -D_{\ell-1} \end{pmatrix} + \begin{pmatrix} 0 & 0 & \cdots & 0 \\ 1 & 0 & \cdots & 0 \\ \vdots & \ddots & \ddots & \vdots \\ 0 & \cdots & 1 & 0 \end{pmatrix}, \quad (129)$$

where we defined

$$D_{\ell} \equiv (-1)^{\ell} \det A = D_{\ell} - \sum_{i=1}^{\ell-1} R_i D_i.$$
 (130)

Therefore, we can write the full diffusion system in the following compact form

$$w' = A^{-1}(\mathcal{S} + \delta \mathcal{C} - Bw). \tag{131}$$

Following the strategy of Ref. [51] (their Sec. 8), we performed a systematic moment expansion to assess both convergence and truncation—scheme systematics of our transport network. Concretely, we solved the longitudinal hierarchy up to $N_{\text{PERT}} = \ell_{\text{max}} = 30$ using the same two closures considered in [51]—a constant—R closure and the variance truncation—and we monitored (i) the baryon—left chemical potential $\mu_{B_L}(z)$, (ii) the cumulative build—up of the BAU as a function of the compactified

 $^{^{28}}$ We believe that the 1/2 in the definition of the B matrix in [51] is a typo and should not be there.

coordinate $u \in [-1, 1]$, and (iii) the final η_B versus N_{PERT} . Our qualitative trends mirror those reported in [51]: increasing N_{PERT} reduces μ_{B_L} and stabilises η_B , with the variance truncation systematically more robust. Quantitatively, however, the transition from the canonical two-moment system to multi-moment truncations is more pronounced in our setup, leading to a sharper suppression of μ_{B_L} as N_{PERT} increases. This is visible in the variance-closure profiles of $\mu_{B_L}(u)$ (top-right panel of Fig. 8), where the $N_{\text{PERT}} = 2$ curve lies noticeably above the $N_{\text{PERT}} \ge 6$ family and the separation persists across the wall region. The same pattern appears in the cumulative integral for $\eta_B(u)$ and in η_B versus N_{PERT} , for both closures, with the variance scheme exhibiting earlier saturation and smaller spread (top row and bottom-middle/right panels of Fig. 8).

A second point of agreement with Ref. [51] concerns the spectrum of the asymptotic evolution matrix \mathcal{X} . Recall that, from (131), the far–from–wall limit (constant background, vanishing sources) yields the autonomous system

$$w'(z) = \mathcal{X} w(z), \qquad \mathcal{X} = \mathcal{X}(x \equiv m/T, v_w; \text{closure}),$$

with \mathcal{X} a sparse matrix fixed by the chosen truncation/closure. The large-|z| behaviour is $w(z) \propto e^{\lambda z}$ with $\lambda \in \operatorname{spec}(\mathcal{X})$, and physical boundary conditions select the decaying eigenmodes (the sign of $\Re \lambda$ required for decay is set by the wall orientation). We find the most stable truncation sequence to be $N_{\text{PERT}} = 2 + 4k$ ($k \in \mathbb{N}$): along $2, 6, 10, \ldots$ the eigenvalues cluster away from the imaginary axis, as can be seen from Fig. 9, so $\Re \lambda$ remains safely negative and oscillatory tails are strongly damped. Numerically, this manifests as monotonic profiles and smooth convergence of the BAU. In the complementary sequences, one encounters more conjugate pairs with $|\Re \lambda| \ll |\Im \lambda|$. This makes the computation numerically unstable, and every prediction does not make much sense, so we are reporting the results only from the stable sequence.

Despite the positive convergence diagnostics, we encountered practical difficulties when integrating the full diffusion network at large N_{PERT} . In our implementation, the boundary conditions at $z = \pm NL_w$ are enforced by introducing constant-in-z Lagrange multiplier fields, λ_{μ_i} and λ_{v_i} , obeying $\partial_{\bar{z}}\lambda_{\mu_i} = \partial_{\bar{z}}\lambda_{v_i} = 0$ and entering the flow equations as linear "boundary sources," e.g.

$$\partial_{\tilde{z}}\tilde{\mu}_{i} = \cdots + \lambda_{u_{i}}(\tilde{z} + N\tilde{L}_{w}), \qquad \partial_{\tilde{z}}u_{i} = \cdots + \lambda_{u_{i}}(\tilde{z} - N\tilde{L}_{w}),$$

with $\tilde{L}_w = L_w/T$ and the sign choice in the v_i -equation made for stability, see Appendix G for more details. This augmentation effectively doubles the state dimension and inserts blocks with vanishing characteristic speeds, which amplifies stiffness and degrades the condition number of the discretised operator as N_{PERT} grows. In practice, sporadic instabilities can be traced to the interplay between this doubling and nearly defective sub-blocks associated with eigenmodes having small $|\Re\lambda|$ in the asymptotic evolution matrix, so that the multiplier-coupled rows/columns render the overall system close to singular. A robust cure is to eliminate the multipliers analytically, or to replace them with constraint imposition strategies that do not enlarge the dynamical state. Implementing these improvements is feasible but beyond the scope of the present release. A refined convergence study and a cross-validation of reliable bands against the moment methodology of Ref. [51] will be presented in the updated version BARYONETv2.



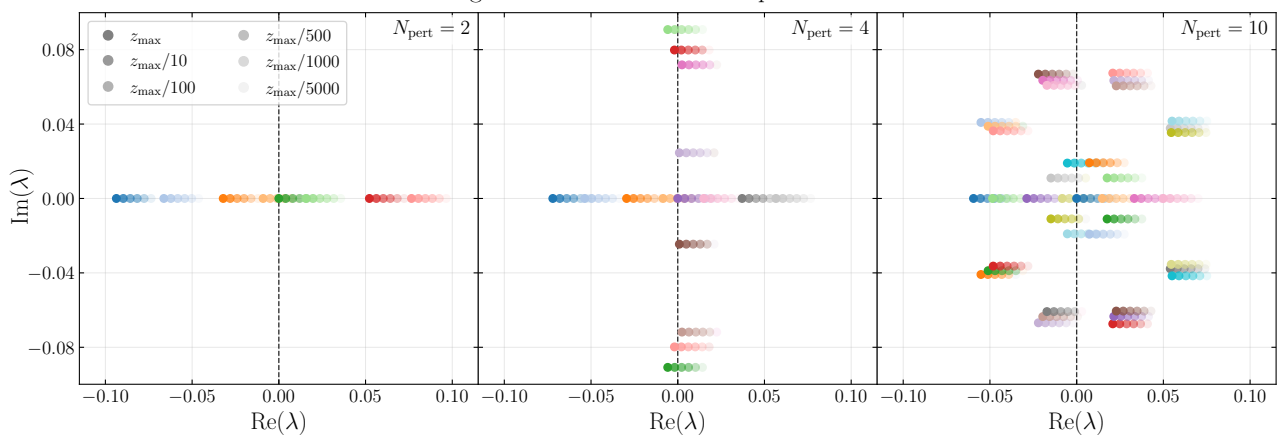


Figure 9: Eigenvalues λ of the far–from–wall propagation matrix \mathcal{X} in the complex plane for three truncations: $\ell_{\text{max}} = 2$ (left), 4 (middle), and 10 (right). The $\ell_{\text{max}} = 4$ spectrum exhibits conjugate pairs with $|\Re \lambda| \ll |\Im \lambda|$, which produce oscillatory spatial behaviour, while $\ell_{\text{max}} = 2$ and 10 are dominated by real, more strongly damped modes. Opacity illustrates changes in the eigenvalues across the wall.

9 Conclusions and outlook

In this work we have delivered a self-contained and pedagogical review of electroweak baryogenesis in the semiclassical WKB framework and turned it into a reproducible, public pipeline. Starting from first principles, we derived the gauge-invariant WKB kinematics (shifted dispersion relations, group velocities, and semiclassical forces) for fields with space-dependent complex masses across a planar bubble wall, and built the stationary Boltzmann equation in the wall frame. We then performed the CP projection and a controlled moment reduction to obtain a compact fluid network for chemical potentials and velocity perturbations, expressed entirely in terms of universal thermal kernels. A key outcome is a uniform notation and set of conventions that reconcile and organise three decades of approaches (FH04, FH06, CK, KV24) within a single language, including a precise operational definition of the final baryon asymmetry η_B with a transparent weak–sphaleron profiling.

On the phenomenology side, we implemented these results in the open-source code BARYONET, providing an end-to-end, automated pipeline from wall profiles (masses, phases, derivatives) to η_B . The collision sector is closed in a model-independent way via thermally averaged rates, enabling consistent applications across a broad class of electroweak-scale extensions. We validated the framework by reproducing representative results from the literature and by supplying benchmark overlays for widely studied scenarios—singlet extensions of the SM (including variants), two-Higgs-doublet models, and Higgs- ϕ^6 setups—thereby establishing both correctness and portability of the implementation.

A central technical contribution of this work lies in the appendices, where we clarify and, where necessary, rederive, the present literature, the ingredients that have long underpinned EWBG computations—diffusion constants, Yukawa-mediated relaxation rates and helicity-flip rates, as well as strong and weak sphaleron rates—clarifying conventions, reconciling formulae scattered across the literature, and, importantly, updating all numerical inputs to current parameter values. These updated, ready-to-use quantities are provided with clear normalisation choices and are wired into BARYONET so that phenomenological studies can rely on a consistent and modern baseline.

Taken together, the self-contained derivation, the unification of the approaches, the public and reproducible code, the explicit validation against prior results, and the systematic update of transport inputs advance EWBG studies from a collection of heterogeneous formalisms to a coherent, documented standard. We hope BARYONET will serve as a reliable reference implementation and a platform for extensions, thereby tightening the connection between microscopic model building and cosmological predictions.

Outlook. Several directions can further improve both the numerical robustness and the physical reach of the present framework:

- Numerical methods. The current enforcement of boundary conditions via constant Lagrange
 multipliers becomes unstable at large perturbation order. Replacing this scheme with direct
 constraint elimination or implicit boundary enforcement methods would substantially improve
 stability and scalability.
- 2. **Flavour-source mixing.** The inclusion of models featuring CP-violating flavour mixing, see [74], is a natural and essential extension, as such scenarios can enhance the generated baryon asymmetry and probe qualitatively new physical effects.
- 3. **EDMs constraints.** An important future direction will be the inclusion of electric dipole moment (EDM) constraints in our analysis. EDM measurements provide extremely sensitive tests of CP violation, directly connected to the sources responsible for baryogenesis, see [61] for a review. Implementing these bounds will be essential to identify regions of parameter space that are simultaneously compatible with successful electroweak baryogenesis and current experimental limits.
- 4. **Beyond the fluid network.** A more ambitious direction is to rethink the approach entirely by abandoning the moment-truncated Boltzmann hierarchy and solving directly for the full out-of-equilibrium distribution (or its perturbation). This can follow the strategy already successful in the CP-even sector—e.g. spectral discretisations in z and momentum using Chebyshev polynomials (see [75]) or finding the eigenfunctions of the kinetic operator (cf. [65–67]). Such methods would bypass closure ambiguities, capture nonlocal angular structure, and offer systematically improvable accuracy with well-understood convergence diagnostics.
- 5. **Spatial dependence of** η_B . Computing the full spatial profile of the baryon asymmetry $\eta_B(z)$ across and ahead of the wall would provide valuable insight into the inhomogeneities imprinted by bubble propagation, with potential implications for baryon-number diffusion, baryogenesis efficiency, and subsequent cosmological observables.

Taken together, these improvements would elevate BARYONET from a state-of-the-art WKB solver to a comprehensive numerical laboratory for baryogenesis and transport phenomena in the early Universe. Future releases will incorporate these developments, providing a benchmark for cross-framework validation and a bridge between microscopic particle physics and cosmological phenomenology.

Acknowledgment This project grew out of a long journey through the literature, during which I benefited from the insight and generosity of many colleagues. I am profoundly and gratefully indebted to **Carlo Branchina**, **Luigi Delle Rose**, and **Salvador Rosauro-Alcaraz**. Their sharp understanding, perseverance in grasping every aspect, and patience in discussing them with me were not merely helpful but truly decisive—shaping my comprehension of the subject and resolving pivotal technical issues without which this work (and the code that implements it) would simply not exist.

I thank Thomas Biekötter, Francesco Costa, and Miguel Vanlasselaer for thoughtful comments on the draft and for their help during the code's beta testing phase. I am indebted to Enrique Fernández-Martínez, Toshihiko Ota, and Salvador Rosauro-Alcaraz for illuminating discussions that helped me clarify several foundational aspects of the theory and for pointing me to parts of the literature I had missed. For early advice at the outset of this project, I warmly thank Benoît Laurent and Mateusz Zych. Finally, I would like to acknowledge José Miguel No and Javi Serra: this work originated from a joint project with them, without which it would not have been possible.

The author acknowledges support from the Spanish Research Agency (Agencia Estatal de Investigación, MCIN/AEI/10.13039/501100011033) via the IFT Severo Ochoa Center of Excellence grant CEX2020-001007-S. In addition, the author is supported by the grant CNS2023-145069 funded by MICIU/AEI/10.13039/501100011033 and by the European Union NextGenerationEU/PRTR.

A Universal kernel

All coefficient functions entering the moment equations are Lorentz-invariant integrals over the equilibrium distribution in the wall frame. They depend only on the local ratio $x \equiv m/T$ and on the wall velocity v_w . We use dimensionless plasma-frame variables $w \equiv E/T$, $\tilde{p}_w = \sqrt{w^2 - x^2}$, and $y \equiv \cos \theta = p_z/|\mathbf{p}| \in [-1, 1]$. A boost with speed v_w along \hat{z} gives

$$\tilde{E} = \gamma_w (w - v_w y \, \tilde{p}_w), \qquad \tilde{p}_z = \gamma_w (y \, \tilde{p}_w - v_w w), \qquad \tilde{E}_{0z} = \sqrt{\tilde{p}_z^2 + x^2}.$$
 (132)

The boosted equilibrium is $f_{0w}(\tilde{E})$, with derivatives $f'_{0w} \equiv \partial_{\tilde{E}} f_{0w}$ and $f''_{0w} \equiv \partial_{\tilde{E}}^2 f_{0w}$. Angle brackets $\langle \cdot \rangle$ denote the moment averages used in the main text, normalised by N_1 .

A.1 Master integral and choices of V

All coefficient functions can then be written as a two-dimensional integral of a generic form²⁹

$$\left\langle \frac{p_z^n}{E^m} V \mathcal{F}_{0w}^{(k)} \right\rangle = T^{n-m-k-1} K(\mathcal{F}_0; V; n, m)$$
(133)

where k = 0, 1, 2 for $\mathcal{F}_{0w}^{(k)} = f_{0w}^{(k)}$, and the dimensionless master integral

$$K(\mathcal{F}_{0}^{(k)}; V; n, m) = -\frac{3}{\pi^{2} \gamma_{w}} \int_{x}^{\infty} dw \int_{-1}^{1} dy \, \frac{\tilde{p}_{w} \tilde{p}_{z}^{n}}{E^{m-1}} \, V(w, y; v_{w}, x) \, \mathcal{F}_{0}^{(k)}(\tilde{E}). \tag{134}$$

For the CP—odd source one may use the spin–s or helicity basis, defined by

$$V_s = \frac{|\tilde{p}_z|}{E_{0z}} = \frac{|\tilde{p}_z|}{\sqrt{\tilde{p}_z^2 + x^2}},\tag{135}$$

$$V_h = V_s^2 \left(1 - \frac{x^2}{w^2} \right)^{-1/2}. \tag{136}$$

When no extra structure is needed, one simply takes V = 1. The other functions defined in the main text can be expressed in term of the master integral as follows

$$D_{\ell}(x, v_w) = K(f'_{0w}; 1; \ell, \ell), \qquad (137)$$

$$T^{2}Q_{\ell}(x, v_{w}) = \frac{1}{2}K(f_{0w}^{"}; 1; \ell - 1, \ell).$$
(138)

$$T^{2}Q_{\ell}^{e}(x,v_{w}) = \frac{1}{2}K(f_{0w}'; 1; \ell-1, \ell).$$
(139)

$$T^{2}Q_{\ell}^{8o}(x,v_{w}) = \frac{1}{2}K(f_{0w}';V;\ell-2,\ell), \qquad (140)$$

$$T^{4}Q_{\ell}^{9o}(x,v_{w}) = \frac{1}{4} \left[K(f_{0w}'; V; \ell - 2, \ell + 2) - \gamma_{w} K(f_{0w}''; V; \ell - 2, \ell + 1) \right], \tag{141}$$

where V is chosen as in (135) or (136). For fixed (x, v_w) the kernels (137)-(141) are universal and can be tabulated once on a grid.

Figure 10 collects the dimensionless functions that enter the two-moment fluid equations: the equilibrium kernels $D_{\ell}(x, v_w)$ and $Q_{\ell}(x, v_w)$, the function $\bar{R}(x, v_w)$, and the source kernels $Q_{\ell}^{8o}(x, v_w; V)$ and $Q_{\ell}^{9o}(x, v_w; V)$ for the two standard weights $V \in \{V_s, V_h\}$ (spin and helicity choices). The example shown fixes $v_w = 0.5$ and scans the mass-to-temperature ratio x = m/T over many decades; changing v_w smoothly deforms the curves without altering their qualitative behaviour. These kernels are universal (model-independent) and are computed once, tabulated, and then interpolated along the wall. In BARYONET, they can be generated with function_interpolators/function_high_vw/ComputeTransportFunctio which produces the tables used by all solvers.

²⁹In [49, 51] they consider $f_{0w}^{(k)}$ as the k-th derivative with respect to its argument, but not considering the temperature. This brings down the power of the temperature for each derivative.

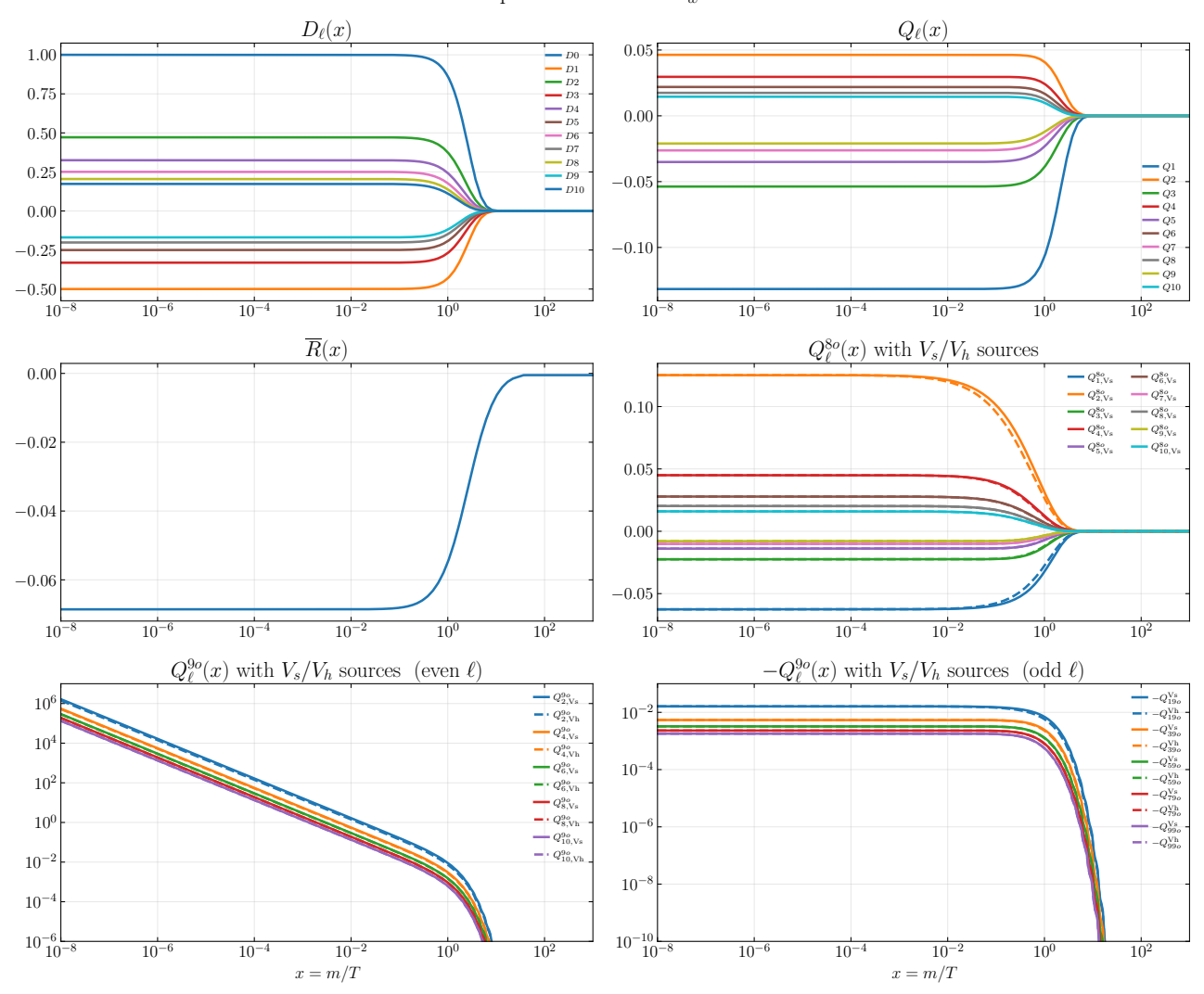


Figure 10: Universal transport kernels at fixed wall velocity $v_w = 0.5$ as functions of x = m/T. Top left: D_{ℓ} for $\ell = 0, ..., 10$. Top right: Q_{ℓ} for $\ell = 1, ..., 10$. Middle left: $\bar{R}(x)$. Middle right: CP-odd source kernels Q_{ℓ}^{8o} for spin/helicity weights V_s, V_h ; Bottom (two panels): CP-odd source kernels Q_{ℓ}^{9o} for spin/helicity weights V_s, V_h ; functions with even/odd ℓ are shown separately to highlight the alternating sign pattern and the large difference in value. These curves are model-independent inputs that depend only on x and v_w and are reused across all scenarios.

B Linearised collision operators

In this appendix, we derive, step by step and in a model-independent way, the linearised collision terms that enter the transport equations. We closely follow the approximations and derivations of Refs. [34, 49, 51, 76].

We consider a generic $2 \to 2$ process, $i_1 i_2 \to f_1 f_2$, in order to be explicit, and we track the evolution of the distribution of species i_1 . The corresponding collision operator can be written as

$$C[f_j] = -\frac{1}{2E_{i_1}} \int_{\{p_{i_2}, p_{f_1}, p_{f_2}\}} |\mathcal{M}|^2 (2\pi)^4 \delta^{(4)}(p_{i_1} + p_{i_2} - p_{f_1} - p_{f_2}) \mathcal{P}[f_{i_{1,2}}, f_{f_{1,2}}], \qquad (142)$$

where f_j denotes the distribution function of species j, where $\int_{\{p\}} = \int \frac{d^3p}{2p_0(2\pi)^3}$, and the statistical factor is

$$\mathcal{P}[f_{i_{1,2}}, f_{f_{1,2}}] \equiv f_{i_1} f_{i_2} (1 \mp f_{f_1}) (1 \mp f_{f_2}) - f_{f_1} f_{f_2} (1 \mp f_{i_1}) (1 \mp f_{i_2}). \tag{143}$$

The upper (lower) signs correspond to fermions (bosons). Equation (143) simply encodes detailed balance with quantum-statistical blocking (for fermions) or enhancement (for bosons).

To perform a systematic gradient expansion, we split each distribution into an equilibrium piece—allowing for a small chemical potential in the wall frame—and a perturbation

$$f_i \equiv f_i(\mu_i) + \delta f_i = \frac{1}{\exp\left[\gamma_w(E_i + v_w p_{j,z})/T - \mu_i/T\right]} + \delta f_i.$$
 (144)

For a generic $2 \rightarrow 2$ process with incoming legs In = $\{i_1, i_2\}$ and outgoing legs Out = $\{f_1, f_2\}$, we linearize around equilibrium $f = f(\mu) + \delta f$ and write

$$\mathcal{P}[f_{i_{1,2}}, f_{f_{1,2}}] \simeq \mathcal{P}[f_{i_{1,2}}(\mu_{i_{1,2}}), f_{f_{1,2}}(\mu_{f_{1,2}})] + \sum_{k \in \{i_1, i_2, f_1, f_2\}} c_k \, \delta f_k, \qquad c_k \equiv \left. \frac{\partial \mathcal{P}}{\partial f_k} \right|_{f = f^0}, \tag{145}$$

where $f^0 = f(\mu = 0)$. Each coefficient c_k is the sum of a loss term and a gain term and, keeping the upper/lower sign for Fermi-Dirac/Bose-Einstein statistics, is given by

$$c_{k} = \begin{cases} \underbrace{\prod_{\ell \in \text{In} \setminus \{k\}} f_{\ell}^{0} \prod_{\ell \in \text{Out}} (1 \mp f_{\ell}^{0})}_{\text{loss}} \pm \underbrace{\prod_{\ell \in \text{Out}} f_{\ell}^{0} \prod_{\ell \in \text{In} \setminus \{k\}} (1 \mp f_{\ell}^{0})}_{\text{gain}}, \quad k \in \text{In}, \\ -\underbrace{\prod_{\ell \in \text{Out} \setminus \{k\}} f_{\ell}^{0} \prod_{\ell \in \text{In}} (1 \mp f_{\ell}^{0})}_{\text{loss}} \mp \underbrace{\prod_{\ell \in \text{In}} f_{\ell}^{0} \prod_{\ell \in \text{Out} \setminus \{k\}} (1 \mp f_{\ell}^{0})}_{\text{gain}}, \quad k \in \text{Out}. \end{cases}$$

$$(146)$$

For $k = i_1$ and $k = i_2$, Eq. (146) gives, for example

$$c_{i_1} = f_{i_2}^0 \left(1 \mp f_{f_1}^0 \right) \left(1 \mp f_{f_2}^0 \right) \pm f_{f_1}^0 f_{f_2}^0 \left(1 \mp f_{i_2}^0 \right), \tag{147}$$

$$c_{i_2} = f_{i_1}^0 \left(1 \mp f_{f_1}^0 \right) \left(1 \mp f_{f_2}^0 \right) \pm f_{f_1}^0 f_{f_2}^0 \left(1 \mp f_{i_1}^0 \right). \tag{148}$$

To make the structure more explicit, we use the statistical identity $1 \mp f = f \exp[\gamma_w(E + v_w p_z)/T]$, together with energy–momentum conservation, $E_{i_1} + E_{i_2} = E_{f_1} + E_{f_2}$, $\mathbf{p}_{i_1} + \mathbf{p}_{i_2} = \mathbf{p}_{f_1} + \mathbf{p}_{f_2}$. After a straightforward rearrangement, the result can be cast as

$$\mathcal{P}[f_{i_{1,2}}, f_{f_{1,2}}] \simeq \mathcal{P}[f_{i_{1,2}}(\mu_{i_{1,2}}), f_{f_{1,2}}(\mu_{f_{1,2}})] + f_{i_1}^0 f_{i_2}^0 \left(\frac{\delta f_{i_1}}{f_{i_1}^0} + \frac{\delta f_{i_2}}{f_{i_2}^0} - \frac{\delta f_{f_1}}{f_{f_2}^0} - \frac{\delta f_{f_2}}{f_{f_2}^0} \right), \tag{149}$$

where we used the fact that in the Maxwell–Boltzmann (MB) limit and using energy conservation, one finds $f_{f_1}^0 f_{f_2}^0 \exp \left[\gamma_w (E_{i_1} + E_{i_2} + v_w (p_{i_1,z} + p_{i_2,z})) \right] = 1$, and exponentially Boltzmann suppressed terms have been dropped, as they are subleading at this order.

B.1 Linearised out-of-equilibrium contributions

To describe departures from equilibrium, we expand the collision operator to first order in the perturbations δf_j . Starting from Eq. (143), only terms containing a single δf are retained. These contributions naturally split into two parts: one proportional to the deviation of the species under consideration, δf_{i_1} , and another proportional to the perturbations of its interaction partners, weighted by the equilibrium distribution of i_1 . The collision term can then be expressed as

$$C[f_{i}, f_{j}] \simeq -\frac{\delta f_{i_{1}}}{2E_{i_{1}}} \int_{\{p_{i_{2}}, p_{f_{1}}, p_{f_{2}}\}} |\mathcal{M}|^{2} f_{i_{2}}^{0} (2\pi)^{4} \delta^{(4)} \left(\sum p_{k}\right)$$

$$+ f_{i_{1}}^{0} \left[\int_{\{p_{i_{2}}\}} \delta f_{i_{2}} \mathcal{A}(p_{i_{1}}, p_{i_{2}}) - \sum_{n} \int_{\{p_{f_{n}}\}} \delta f_{f_{n}} \mathcal{G}_{f_{n}}(p_{i_{1}}, p_{f_{n}}) \right]$$

$$\equiv -\Gamma(p_{i_{1}}) \delta f_{i_{1}} + \Delta \mathcal{F},$$

$$(150)$$

where the first term represents the direct relaxation of i_1 toward equilibrium, and ΔF collects the influence of the perturbations of the other species involved in the reaction. The functions $\mathcal{A}(p_{i_1}, p_{i_2})$

and $\mathcal{G}_{f_n}(p_{i_1}, p_{f_n})$ are phase-space kernels built from the squared matrix element $|\mathcal{M}|^2$ and equilibrium distributions. They are obtained by taking the derivative of the statistical factor $\mathcal{P}[f_j]$ with respect to f_{i_2} or f_{f_n} and then evaluating at equilibrium. The kernel functions appearing in Eq. (150) take the standard forms

$$\mathcal{A}(p_{i_1}, p_{i_2}) = \frac{1}{2E_{i_1}} \int_{\{p_{f_1}, p_{f_2}\}} (2\pi)^4 \delta^{(4)} \left(\sum p_k\right) |\mathcal{M}|^2 (1 \mp f_{f_1}^0) (1 \mp f_{f_2}^0),$$

$$\mathcal{G}_{f_n}(p_{i_1}, p_{f_n}) = \frac{1}{2E_{i_1}} \int_{\{p_{i_2}, p_{f_m \neq f_n}\}} (2\pi)^4 \delta^{(4)} \left(\sum p_k\right) |\mathcal{M}|^2 f_{i_2}^0 (1 \mp f_{f_n}^0).$$
(151)

The first kernel, \mathcal{A} , encodes the effect of the incoming partner i_2 on the relaxation of i_1 , while \mathcal{G}_{f_n} describes the feedback from the final-state particles f_n . In the following, we neglect the kernel functions \mathcal{A} and \mathcal{G} altogether; only the effective interaction rates Γ_{ij} are retained in the subsequent analysis.

The relaxation rate $\Gamma(p_{i_1})$ appearing in Eq. (150) corresponds to the familiar thermal scattering rate of the process $i_1i_2 \rightarrow f_1f_2$:

$$\Gamma_{i_1, i_2 \to f_1, f_2} = \frac{1}{2E_{i_1}} \int_{\{p_{i_2}\}} f_{i_2}^0 \langle \sigma v \rangle
= \frac{1}{2E_{i_1}} \int_{\{p_{i_2}\}} f_{i_2}^0 \int_{\{p_{f_1}, p_{f_2}\}} (2\pi)^4 \, \delta^{(4)} \Big(\sum p_k \Big) |\mathcal{M}|^2,$$
(152)

where $\langle \sigma v \rangle$ is the standard thermal average of the cross section times relative velocity. As usual, $|\mathcal{M}|^2$ is summed or averaged over internal degrees of freedom. The same reasoning applies to processes with any number of external particles.

Moment of the linearised collision operator. When computing the velocity moments of the collision operator (see Sec. 3.8), a standard and consistent procedure is to replace the momentum–dependent $\Gamma(p)$ that appear in the linearised operator with their thermally averaged, per–particle counterparts $\widehat{\Gamma}$ —the so–called relaxation–time approximation (RTA). Invoking detailed balance for the equilibrium pieces (so that the collision term vanishes on equilibrium), for the first two moments, one obtains

$$\langle \delta C \rangle \simeq 0, \qquad \left\langle \frac{p_z}{E_{i_1}} \, \delta C \right\rangle \simeq -\left\langle \frac{p_z}{E_{i_1}} \, \delta f_{i_1} \right\rangle \kappa^X \, \widehat{\Gamma} = -u_1 \kappa^X \, \widehat{\Gamma}, \qquad (153)$$

where $\langle \cdot \rangle$ denotes the thermal average as in the main text and, in the last equality, we used the definition of the velocity perturbation $u_1 \equiv \langle (p_z/E_0) \, \delta f \rangle$. For the definition of the coefficient κ^X see Sec 3.8. The first relation reflects particle-number conservation in elastic $2 \to 2$ scatterings (no source in the zeroth moment at linear order), while the second encodes the relaxation of the momentum perturbation at a rate set by $\widehat{\Gamma}$.

B.2 Linearised chemical potential contributions

We now turn to the contribution proportional to $\mathcal{P}[f_{i_{1,2}}(\mu_{i_{1,2}}), f_{f_{1,2}}(\mu_{f_{1,2}})]$ in Eq. (143). As in the previous subsection, we expand the distributions to first order in gradients. Writing $\xi_i \equiv \mu_i/T$, one finds

$$f_i(\mu_i) \simeq f_i^0 \left[1 + (1 \mp f_i^0) \xi_i \right],$$
 (154)

where the factor $(1 \mp f_i^0)$ encodes the fermionic blocking or bosonic enhancement. Using again Maxwell–Boltzmann statistics for the equilibrium pieces (so that $1 \mp f_i^0 \to 1$ in the linearised expansion) and energy conservation, the statistical factor reduces to

$$\mathcal{P}[f_{i_{1,2}}(\mu_{i_{1,2}}), f_{f_{1,2}}(\mu_{f_{1,2}})] \simeq f_{i_1}^0 f_{i_2}^0 \left[\xi_{i_1} + \xi_{i_2} - \xi_{f_1} - \xi_{f_2}\right], \tag{155}$$

which is the familiar driving combination of chemical potentials dictated by detailed balance. Inserting this into the collision integral and using the same steps as for the δf_i piece yields

$$\delta C[\xi_{i_{1,2}}, \xi_{f_{1,2}}] \simeq -f_{i_1}^0 \sum_{i,j} \Gamma_{i \to j} s_{ij} \xi_j , \qquad (156)$$

with $s_{ij} = \pm 1$ for initial (final) state particles, respectively. This term provides the number-changing (source/sink) component of the collision operator induced by departures from chemical equilibrium.

B.3 Thermal averaging

Collecting the contributions proportional to δf_i and to the chemical potentials μ_i , the collision operator for species a—including both number–changing channels and elastic scatterings—can be organized as in Eqs. (54) and (55), where the sum runs over all relevant processes and $\Gamma^{\rm wf}$ denotes the wall–frame rate for $1 \to 2$ or $2 \to 2$ reactions. Following Ref. [34], we drop the $\Delta \mathcal{F}$ term from Eq. (150): in the linearised moment expansion and under our working assumptions, it does not contribute to the first two moments

We replace the momentum–dependent rates by their thermally averaged, per–particle counterparts $\hat{\Gamma}$ (see Sec. 3.8 for the averaging conventions and normalisation κ^X). Projecting onto the first two velocity moments then gives

$$\delta C_{1} = \langle \delta C \rangle \simeq -\langle f_{0w} \rangle \kappa^{X} \sum_{i,j} \widehat{\Gamma}_{i \to j} s_{ij} \xi_{j} = -K^{(0)} \kappa^{X} \sum_{i,j} \widehat{\Gamma}_{i \to j} s_{ij} \xi_{j} ,$$

$$\delta C_{2} = \left\langle \frac{p_{z}}{E_{0}} \delta C \right\rangle \simeq -\left\langle \frac{p_{z}}{E_{0}} f_{0w} \right\rangle \kappa^{X} \sum_{i,j} \widehat{\Gamma}_{i \to j} s_{ij} \xi_{j} - \kappa^{X} \widehat{\Gamma}_{tot} \left\langle \frac{p_{z}}{E_{0}} \delta f \right\rangle$$

$$= -K^{(1)} \kappa^{X} \sum_{i,j} \widehat{\Gamma}_{i \to j} s_{ij} \xi_{j} - \kappa^{X} \widehat{\Gamma}_{tot} u_{1} ,$$
(157)

and similarly for higher moments. Here $K^{(0)} \equiv \langle f_{0w} \rangle$ and $K^{(1)} \equiv \langle (p_z/E_0) f_{0w} \rangle$ are the universal projection weights; $u_1 \equiv \langle (p_z/E_0) \delta f \rangle$ is the first velocity moment; s_{ij} keeps track of the sign/stoichiometry of species j in channel i; and $\hat{\Gamma}_a^{\text{tot}} = \sum_{i \in a} (\hat{\Gamma}_i^{\text{el}} + \hat{\Gamma}_i^{\text{inel}})$ is the total (per–particle) scattering rate for species a. Inelastic processes relax the appropriate linear combinations of ξ_j in both moments, while the elastic (and elastic part of inelastic) contribution appears as a flow–damping term in the second moment through $\hat{\Gamma}_a^{\text{tot}} u_{1,a}$.

Remark on conventions. The compact form above can look different from the presentation in Ref. [51]. Apparent discrepancies typically trace back to (i) whether wall— or rest–frame rates are inserted before averaging, (ii) the precise normalisation (κ^X vs. $12/T^3$ or $1/N_1$) and averaging measure, (iii) the sign and assignment of s_{ij} , (iv) whether the δF term is retained, and (v) MB versus quantum (FD/BE) weights in the linearisation. Accounting for these choices reconciles the formulas without affecting the underlying physics.

We are grateful to Salvador Rosauro-Alcaraz for incisive clarifications on the derivation of the linearised collision integrals and for guidance on aligning our conventions and averaging prescriptions with the existing literature.

C Diffusion constants

In this appendix, we revisit in detail the calculation of diffusion constants for relativistic particles in a hot plasma. These quantities were computed systematically for the first time in [29] and [31], and here we provide a pedagogical rederivation. We follow a linear-response approach starting from the Boltzmann equation, clarifying how the transport rate is defined, how scattering amplitudes enter the calculation, and how thermal masses regulate the infrared divergences arising from soft gauge-boson exchange.

We consider the relation between a particle–number current and a small spatial gradient of its density. Let $n(\mathbf{x},t)$ be the (particle minus antiparticle) number density of the species, and let $\mathbf{J}(\mathbf{x},t)$

be its spatial number current density. Decomposing the current into a convective part carried by the bulk flow **u** and a diffusive part, $\mathbf{J} = n \mathbf{u} + \mathbf{J}_d$, the diffusion constant D is defined by Fick's law

$$\mathbf{J}_d = -D\,\mathbf{\nabla}n\,. \tag{158}$$

In kinetic theory, the evolution of the distribution function f(x,p) is governed by the Boltzmann equation

$$\frac{p^{\mu}}{p^{0}} \partial_{\mu} f(x, p) = -C[f](x, p), \tag{159}$$

where C[f] is the collision integral³⁰. We assume a slowly varying local chemical potential $\xi(x) = \beta \mu(x)$, with $\beta = 1/T$, so that the equilibrium distribution takes the form

$$f_0(p,x) = \frac{1}{e^{\beta p^0 + \xi(x)} + 1} \qquad \text{for fermions.}$$
 (160)

We now linearise around the equilibrium

$$f(p,x) = f_0(p,x) + \delta f(p,x), \qquad |\delta f| \ll f_0.$$
 (161)

Because the perturbation is induced by a spatial gradient in $\xi(x)$ (say, in the x-direction), the most general ansatz consistent with rotational symmetry in the transverse plane is

$$\delta f_{\mathbf{p}} = g(p) \frac{p_x}{p^0},\tag{162}$$

where g(p) is an unknown function of the momentum magnitude. Inserting this ansatz and linearising the Boltzmann equation gives

$$f_0'(p^0) \partial_x \xi \simeq -g(p) \Gamma_t(p),$$
 (163)

which defines the transport rate $\Gamma_t(p)$. It characterises the relaxation of the anisotropic part of the distribution.

C.1 Expression for the diffusion constants

The number density is related to the chemical potential by

$$n \simeq n_0 - \frac{T^3}{12} \xi$$
 (relativistic fermions). (164)

The associated current in the z-direction is

$$J_z = \int \frac{d^3p}{(2\pi)^3} \, \delta f(p) \, \frac{p_z}{p^0}. \tag{165}$$

Combining these expressions yields the master formula

$$D = \frac{12}{T^3} \int \frac{d^3p}{(2\pi)^3} \frac{-f_0'(p^0)}{\Gamma_t(p)} \left(\frac{p_z}{p^0}\right)^2.$$
 (166)

Equation (166) shows that D is essentially the momentum-space average of the inverse transport rate, weighted by the thermal distribution.

For a generic $2 \to 2$ scattering process with incoming states $\{p, k\}$ and outgoing states $\{p', k'\}$, the collision integral is

$$C[f] = \frac{1}{2p_0} \int_{\{p',k,k'\}} \delta^{(4)}(p+k-p'-k') |\mathcal{M}|^2 \mathcal{P}[f], \tag{167}$$

 $^{^{30}}$ In this subsection only we adopt the sign convention used in much of the literature: we factor the overall minus sign out of the collision integral and define the (linearised) collision operator with the opposite sign. This is purely notational—the minus sign simply migrates from the explicit definition of the diffusion coefficient D to the total relaxation rate Γ_t —so all physical results are unchanged.

where $\int_{\{p\}} = \int \frac{d^3p}{2p_0(2\pi)^3}$, and where the statistical factor has been defined in Eq. (143). Linearising and projecting onto the perturbation ansatz leads to

$$\Gamma_t(p) = \frac{1}{2p_0^3} \int_{\{p',k,k'\}} (2\pi)^4 \delta^{(4)} \left(\sum p_i\right) |\mathcal{M}|^2 \left(-f_0'\right) (p \cdot p'). \tag{168}$$

We now evaluate this expression in the centre–of–mass (CM) frame, where the kinematics simplify. Throughout, the subscript t indicates that we are considering the t-channel contribution.

The dominant contribution arises from t-channel exchange of gauge bosons. After performing spin and colour sums, one obtains, for massless external fermions,

$$|\mathcal{M}_B|^2 = \frac{80 Y^2 g_1^4 s^2}{(t - M_B^2)^2},\tag{169}$$

$$|\mathcal{M}_W|^2 = \frac{36 g_2^4 s^2}{(t - M_W^2)^2},\tag{170}$$

$$|\mathcal{M}_g|^2 = \frac{32 g_3^4 (s^2 + u^2)}{(t - M_g^2)^2}.$$
 (171)

Here $s = (p + k)^2$, $t = (p - p')^2$, $u = (p - k')^2$, Y is the hypercharge of the external fermion, and $g_{1,2,3}$ are the gauge couplings for $U(1)_Y$, $SU(2)_L$, and $SU(3)_c$. The denominators contain the *Debye masses* $M_{B,W,q}$ which regulate the infrared divergence at t = 0.

In computing the transport rate, it is convenient to work in the centre-of-mass (CM) frame of the $2 \to 2$ process, since the integrand of the k' and p' phase-space integrals is Lorentz invariant. In the CM frame, one has

$$\vec{p} + \vec{k} = 0 = \vec{p}' + \vec{k}', \qquad p^0 = k^0 \equiv E, \qquad p'^0 = k'^0 \equiv E,$$

and the linearised collision operator projected onto the transport harmonic yields

$$\Gamma_t(E) = \frac{1}{2E^3} \int_{\vec{k}} \frac{(-f_0'(k^0))}{2k^0} \cdot \frac{1}{32\pi^2} \int d\Omega |\mathcal{M}|^2 (p \cdot p'), \tag{179}$$

where f_0 is the equilibrium distribution and $f'_0(x) \equiv \partial f_0/\partial x$. Approximating all external legs as massless wherever permitted (masses only enter as IR regulators), one finds

$$p \cdot p' = p^0 p'^0 - \vec{p} \cdot \vec{p}' \simeq E^2 - |\vec{p}|^2 \cos \theta \simeq p^2 (1 - \cos \theta),$$
 (180)

with $p \equiv |\vec{p}| = E$. In the CM frame $s \simeq 4p^2$ and for small-angle scattering

$$t \simeq -2p^2(1-\cos\theta) \equiv -2p^2y, \qquad y \equiv 1-\cos\theta \in [0,2].$$
 (181)

For t-channel gauge exchange the squared matrix element has the universal near-forward structure

$$|\mathcal{M}|^2 \propto \frac{\text{(couplings)} \times \text{(kinematics)}}{(t - M^2)^2} \longrightarrow \frac{Ag^4}{(t - M^2)^2},$$
 (182)

where M^2 is the appropriate Debye mass and A collects group and spinor factors. Using $d\Omega = 2\pi d(\cos \theta) = -2\pi dy$ and $p \cdot p' = p^2 y$, the angular integral in (179) reduces to

$$\int d\Omega \frac{p^2 y}{(t - M^2)^2} = 2\pi \int_0^2 dy \frac{p^2 y}{(-2p^2 y - M^2)^2} = \frac{\pi}{2p^2} \int_0^2 dy \frac{y}{(y + a)^2},$$
(183)

where we defined the dimensionless IR regulator $a\equiv \frac{M^2}{2pk}$. The remaining elementary integral can be done in closed form³¹

³¹Screening by a Debye mass $M \equiv m_D$ is implemented by excluding $|t| < m_D^2$. In the CM parametrisation t = -(s/2) y this corresponds to $y_{\min} = a \simeq M^2/(2pk)$. Evaluating $\mathcal{I}(a)$ from y_{\min} to 2, gives $\mathcal{I}(a) = \ln(1/a) + \mathcal{O}(1)$ for $a \ll 1$. Thus the Debye cutoff replaces $\ln(2/a) \to \ln(1/a)$, i.e. reduces the result by a constant $\ln 2$. Below, we follow the standard leading-log convention.

Box C.1: Debye screening masses in the SM-symmetric phase

The Debye (electric screening) mass is defined from the longitudinal self-energy in the static, soft limit

$$m_D^2 \equiv -\Pi_{00}(\omega = 0, \mathbf{k} \to 0). \tag{172}$$

At leading order (hard-thermal-loop) for a gauge coupling g,

$$m_D^2 = g^2 T^2 \left[\frac{C_A}{3} + \frac{1}{12} \sum_{\text{Wevl}} T(R_f) + \frac{1}{3} \sum_{\text{complex scalars}} T(R_s) \right],$$
 (173)

with C_A the adjoint Casimir $(C_A = N \text{ for } SU(N))$ and T(R) the index of representation (T(F) = 1/2 for the fundamental). Counting shortcut: 1 Dirac = 2 Weyl so $\frac{1}{6} \sum_{\text{Dirac}} T(R_f)$ is equivalent; 1 complex scalar = 2 real so $\frac{1}{6} \sum_{\text{real}} T(R_s)$ is equivalent. For $U(1)_Y$, replace $T(R) \to Y^2$ in the chosen normalisation.

(1) Masses for $SU(2)_L$. Gauge: $C_A/3 = 2/3$. Fermions: only LH doublets; per generation 6 Weyl quarks + 2 Weyl leptons \Rightarrow 24 Weyl over 3 generations, each with T(F) = 1/2, giving $\frac{1}{12} \sum T = 1$. Scalars: one complex Higgs doublet, $\frac{1}{3} \sum T = 1/6$. Therefore

$$m_{D,2}^2 = g_2^2 T^2 \left(\frac{2}{3} + 1 + \frac{1}{6}\right) = \frac{11}{6} g_2^2 T^2 = \frac{22\pi}{3} \alpha_w T^2.$$
 (174)

The author's choice in [29] (used as IR regulator inside logs) drops the scalar +1/6 piece:

$$M_W^2 = \frac{5}{3}g_2^2T^2 = \frac{20\pi}{3}\alpha_w T^2. \tag{175}$$

(2) Masses for $SU(3)_c$. Gauge: $C_A/3=1$. Fermions: $N_f=6$ Dirac flavours in F, so $\frac{1}{6}\sum_{\text{Dirac}}T(F)=\frac{1}{6}\cdot 6\cdot \frac{1}{2}=1/2$. No coloured scalars in the SM:

$$m_{D,3}^2 = 2g_3^2 T^2 = 8\pi \alpha_s T^2 \quad (N_f = 6).$$
 (176)

At EW temperatures all six quark flavours are active, matching the paper's $M_q^2 = 8\pi\alpha_s T^2$.

(3) Masses for $U(1)_Y$. Full HTL sum in the SM symmetric phase yields

$$m_{D,Y}^2 = \frac{11}{6}g'^2T^2. (177)$$

The Ref. [29] instead uses the simpler effective regulator $M_B^2 = \frac{1}{3}g'^2T^2 = \frac{4\pi}{3}\alpha_w \tan^2\theta_W T^2$, which differs from the full HTL by a factor (1/3)/(11/6) = 2/11.

SM values adopted. With $\alpha_w = g_2^2/(4\pi)$, $\alpha_s = g_3^2/(4\pi)$, $\tan \theta_W = g_1/g_2$

$$M_B^2 = \frac{4\pi}{3} \alpha_w \tan^2 \theta_W T^2, \quad M_W^2 = \frac{20\pi}{3} \alpha_w T^2, \quad M_g^2 = 8\pi \alpha_s T^2.$$
 (178)

Note on magnetic screening. Only longitudinal (electric) modes are Debye screened at one loop. Transverse (magnetic) modes lack perturbative screening; a magnetic mass $m_M \sim g^2 T$ arises nonperturbatively and is not included in leading-log transport estimates.

$$\mathcal{I}(a) = \int_0^2 dy \, \frac{y}{(y+a)^2} = \left[\ln(y+a) + \frac{a}{y+a}\right]_0^2 = \ln\left(\frac{2+a}{a}\right) + \frac{a}{2+a} - 1$$

$$= \ln\left(\frac{2}{a}\right) + \mathcal{O}(1) \quad (a \ll 1).$$
(184)

Keeping only the leading logarithm and restoring the overall prefactors one obtains the characteristic CM-frame kernel

$$\Gamma_t(E) \propto \int_{\vec{k}} \frac{-f_0'(k^0)}{2k^0} \frac{1}{p^2} \ln\left(\frac{2}{a}\right) = \int_{\vec{k}} \frac{-f_0'(k^0)}{2k^0} \frac{1}{p^2} \ln\left(\frac{4pk}{M^2}\right).$$
 (185)

Thermal averaging over the hard momentum $k^0 \sim T$ and using the standard "slow-log" approximation

$$\int dx \, x^n f_0'(x) \ln(1/x)^{-1} \simeq \ln(1/x_n)^{-1} \int dx \, x^n f_0'(x), \qquad x_n \simeq n, \tag{186}$$

leads to the compact leading-log estimate

$$\Gamma_t \approx \frac{A}{32} g^4 \frac{T^3}{6\pi \, p^2} \ln\left(\frac{4pTx_2}{M^2}\right),\tag{187}$$

where $x_2 \simeq 2.399$ encodes the precise thermal averaging convention and M^2 is the Debye mass of the exchanged gauge boson, and A distinguishes between the different vector bosons exchange.

From Γ_t to D^{-1} . Inserting this result in the master formula (166) and using $\langle (p_z/p)^2 \rangle = 1/3$ together with the exact Fermi–Dirac moment $\int \frac{d^3p}{(2\pi)^3} (-f_0'(p)) \, p^2 = \frac{7\pi^2}{60} T^4$, we arrive at the compact leading–log expression

$$D^{-1} = \frac{5}{448\pi^3} A g^4 T \ln\left(\frac{2x_2 x_4 T^2}{M^2}\right),\tag{188}$$

which makes all phase–space and thermal factors explicit, and where $x_4 \simeq 4.131$.

Writing $g^4 = (4\pi\alpha)^2$ and inserting the group-theory weights $A_{B,W,g} = \{80 \, Y^2, 36, 32 \times 2\}$, Eq. (188) gives, channel by channel,

$$D_B^{-1} \simeq \frac{100}{7\pi} \,\alpha_w^2 \tan^4 \theta_W \, Y^2 \, T \, \ln \left(\frac{2 \, x_2 x_4 \, T^2}{M_B^2} \right),$$

$$D_W^{-1} \simeq \frac{45}{7\pi} \,\alpha_w^2 \, T \, \ln \left(\frac{2 \, x_2 x_4 \, T^2}{M_W^2} \right),$$

$$D_G^{-1} \simeq \frac{80}{7\pi} \,\alpha_s^2 \, T \, \ln \left(\frac{2 \, x_2 x_4 \, T^2}{M_g^2} \right).$$
(189)

The authors in [29] absorb the product $2x_2x_4$ into the reference choice $\ln(32T^2/M^2)$, yielding the familiar forms quoted in their paper. The total diffusion inverse for a given species is the sum over the channels it couples to³²,

$$D_{\ell_R}^{-1} = D_B^{-1},$$

$$D_{\ell_L}^{-1} = D_W^{-1} + Y_{\ell_L}^2 D_B^{-1}, \qquad \epsilon_L = 1, \ \epsilon_R = 0.$$

$$D_{q_{L,R}}^{-1} = Y_{q_{L,R}}^2 D_B^{-1} + \epsilon_{L,R} D_W^{-1} + D_G^{-1},$$
(190)

Adopting the benchmark couplings $\alpha_w \simeq 1/30$, $\alpha_s \simeq 1/7$, $\alpha_w \tan^2 \theta_W \simeq 1/103$ and the paper's Debye regulators, Eqs. (188)-(189) with $4x_2x_4 = 32$ numerically give

$$D_B \simeq \frac{350}{TY^2}, \qquad D_W \simeq \frac{115}{T}, \qquad D_G \simeq \frac{6}{T},$$

³²The exact derivation of these combinations is presented in the Box C.2.

Box C.2: How the channel combination is built.

In the linearised Boltzmann equation, the momentum–relaxation (transport) rate is additive over independent interaction channels: $\Gamma_t = \sum_{X \in \{B,W,g\}} \Gamma_t^{(X)}$. Since D follows from Eq. (166) as a thermal average of $1/\Gamma_t$, the leading–log (LL) evaluation—where each $\Gamma_t^{(X)}$ is dominated by the same near–forward region and differs only by its coupling/group factor—allows one to write the inverse diffusion constant as a sum of channel contributions,

$$D^{-1}(\psi) \simeq D_B^{-1}(\psi) + D_W^{-1}(\psi) + D_G^{-1}(\psi).$$

For hypercharge exchange, the squared matrix element carries $g_1^4\,Y_\psi^2\,Y_{\rm bath}^2$; after summing/averaging over the bath, the probe's factor Y_ψ^2 remains explicit. It is thus convenient to define a reference B-channel kernel D_B^{-1} and then scale it by the probe hypercharge,

$$D_B^{-1}(\psi) = Y_{\psi}^2 D_{B, Y^2=1}^{-1},$$

so that, e.g., for leptons $Y_{\ell_R}^2 = 1$ and $Y_{\ell_L}^2 = 1/4$, implying the familiar quarter relation for the B piece of ℓ_L compared to ℓ_R . The W-channel contributes only for $SU(2)_L$ doublets, captured by $\epsilon_{\psi} = 1$ (LH doublets) or 0 (RH singlets):

$$D_W^{-1}(\psi) = \epsilon_{\psi} D_W^{-1}, \qquad \epsilon_{\ell_L, q_L} = 1, \quad \epsilon_{\ell_R, u_R, d_R} = 0.$$

The gluon piece is universal for colored probes: $D_G^{-1}(\psi) = D_G^{-1}$ for all quarks, and vanishes for leptons. Altogether,

$$D^{-1}(\psi) = Y_{\psi}^2 D_{B,Y^2=1}^{-1} + \epsilon_{\psi} D_W^{-1} + \delta_{\psi} D_G^{-1},$$

with $\delta_{\psi} = 1$ for quarks and 0 for leptons. In the compact notation used in the text, this is equivalently written as

$$D_{\ell_R}^{-1} = D_B^{-1}, \quad D_{\ell_L}^{-1} = D_W^{-1} + \tfrac{1}{4}D_B^{-1}, \quad D_{q_{L,R}}^{-1} = Y_{q_{L,R}}^2 D_B^{-1} + \epsilon_{L,R} D_W^{-1} + D_G^{-1}.$$

and, combining channels as above,

$$D_{\ell_R} \simeq \frac{350}{T}, \quad D_{\ell_L} \simeq \frac{106}{T}, \quad D_{q_L} \simeq \frac{5.8}{T}, \quad D_{q_R} \simeq \frac{6.1}{T}.$$

If instead one uses the full HTL screening masses for the SM (e.g. $M_W^2 = \frac{22\pi}{3}\alpha_w T^2$ and $M_B^2 = \frac{11}{6}g'^2T^2 = \frac{11\pi}{3}\alpha_w\tan^2\theta_W T^2$), the updated values $\alpha_s(m_Z) \simeq 0.1179$, $\alpha_w(m_z) \simeq 0.0338$, $\alpha_w(\tan\theta_w)^2 \simeq 0.0102$, and the true values for $x_{2,4}$, then the logs become smaller and the corresponding numbers shift mildly

$$D_B \simeq \frac{410}{T \, Y^2}, \quad D_W \simeq \frac{110}{T}, \quad D_G \simeq \frac{7.6}{T}, \quad D_{\ell_L} \simeq \frac{100}{T}, \quad D_{q_L} \simeq \frac{7.2}{T}, \quad D_{q_R} \simeq \frac{7.6}{T}.$$

These slight differences relative to the compact literature values trace back to two deliberate choices: (i) the precise IR regulator used inside the leading logarithm, and (ii) keeping the explicit $2x_2x_4$ from CM kinematics and thermal averaging rather than setting it to 32. Both effects only enter the argument of the log and therefore produce $\mathcal{O}(10\%)$ variations without changing the characteristic LL scaling or the channel hierarchy.

C.2 Diffusion constant of the Higgs field: D_h

The leading—log derivation of the diffusion constant for the Higgs, proceeds as in the fermionic case (linearised Boltzmann equation, near-forward t-channel exchange, regulated by Debye screening slow—log thermal averaging), but three inputs are different for a relativistic scalar: The rate uses the Bose–Einstein derivative

$$-f'_B(E) = \frac{e^{E/T}}{(e^{E/T} - 1)^2},$$

instead of the Fermi–Dirac one. Consequently all thermal moments entering the collision integral are bosonic,

$$I_m^{(B)} \equiv \int_0^\infty dx \, x^m (-f_B'(x)) = \Gamma(m+1) \, \zeta(m) \qquad (m>1),$$
 (191)

while for fermions $I_m^{(F)} = \Gamma(m+1)(1-2^{1-m})\zeta(m)$. In particular, $I_2^{(B)}/I_2^{(F)} = 2$ and $I_4^{(B)}/I_4^{(F)} = 8/7$, so the bosonic prefactor is larger by the factor $(I_2^{(B)}I_4^{(B)})/(I_2^{(F)}I_4^{(F)}) = 16/7$. For a complex scalar in representation R the gauge–scalar–scalar vertex is $ig_V(p+p')^\mu T_R^a$. The

For a complex scalar in representation R the gauge–scalar–scalar vertex is $ig_V(p+p')^{\mu}T_R^a$. The squared matrix element therefore carries the kinematic numerator $(s-u)^2$, in contrast to the s^2 coming from the spinor current $\bar{u}\gamma^{\mu}u$.

When factoring out the slowly varying logarithm, the effective points are the *bosonic* ones (denoted $x_m^{(B)}$), not the fermionic ones; see below.

Master formula. Starting from the linearised Boltzmann equation and the standard anisotropy ansatz for a scalar perturbation, one obtains

$$D_h = \frac{12}{T^3} \int \frac{d^3p}{(2\pi)^3} \frac{-f_B'(p)}{\Gamma_t^{(h)}(p)} \left(\frac{p_z}{p}\right)^2, \tag{192}$$

where $\Gamma_t^{(h)}$ is the transport (momentum–relaxation) rate of the Higgs mode, to be computed at leading log from small–angle t-channel exchange.

For $2 \rightarrow 2$ scattering mediated by a gauge boson V = B, W between the Higgs H and a plasma constituent X, the scalar–gauge vertices yield

$$|\mathcal{M}_B(HX)|^2 = 16 g'^4 Y_H^2 Y_X^2 \frac{(s-u)^2}{(t-M_R^2)^2},$$
(193)

$$|\mathcal{M}_W(HX)|^2 = 16 g_2^4 C_2(H) C_2(X) \frac{(s-u)^2}{(t-M_W^2)^2},$$
 (194)

with Y the hypercharge and $C_2(R)$ the quadratic Casimir in representation R ($C_2(H) = 3/4$ for the SM Higgs doublet). The overall factor 16 is the familiar kinematic factor from two scalar vertices $(p+p')^{\mu}$ and their contraction. In the near-forward (small-angle) region relevant for the leading logarithm,

$$(s-u)^2 \xrightarrow{\text{forward}} 4s^2, \tag{195}$$

which changes the transport weight relative to a pure s^2 numerator, prior to the angular average.

Leading-log expression and bosonic slow-log points. Summing over all scattering partners X present in the plasma (with degeneracies d_X : spin/polarisations, colour, isospin, particle/antiparticle) and performing the same transport-weight angular average as in the fermionic derivation, the small-angle contribution gives

$$D_h^{-1} \simeq \sum_{V=B,W} \frac{5\mathcal{A}_V^{(h)}}{49\pi^3} g_V^4 T \ln\left(\frac{2\bar{x}_2^{(B)} x_4^{(B)} T^2}{M_V^2}\right), \qquad g_B \equiv g', \quad g_W \equiv g_2, \tag{196}$$

where M_V^2 are the longitudinal Debye screening masses that regulate the IR. Here the prefactor $1/(49\pi^3)$ is the bosonic one, obtained from the fermionic $1/(448\pi^3)$ by multiplying by the moment ratio 16/7 and by 4 that is coming from the forward–limit enhancement (195), and $\bar{x}_2^{(B)}$, $x_4^{(B)}$ are the bosonic "slow–log" evaluation points determined by the replacements

$$\int_0^\infty dx \, x^m f_B'(x) \frac{1}{\ln(1/x)} \approx \frac{1}{\ln(1/x_m^{(B)})} \int_0^\infty dx \, x^m f_B'(x) \,, \qquad x_m^{(B)} \simeq m \,. \tag{197}$$

Strictly speaking, this approximation is trustworthy only for m > 2, and it becomes accurate for $m \gtrsim 4$. In practice, it is convenient to adopt effective values $\bar{x}_m^{(B)}$, for m < 2, that reproduce the full numerical

integral, and the one from the above expression for $m \ge 4$. We will use $\bar{x}_2^{(B)} \simeq 1.593$ and $x_4^{(B)} \simeq 3.83$, which retain the same functional form as in the fermionic case while matching the bosonic integrals.³³

The other difference in the bosonic case is encoded in the following coefficients

$$\mathcal{A}_{B}^{(h)} = 16 Y_{H}^{2} \sum_{X} d_{X} Y_{X}^{2}, \qquad \mathcal{A}_{W}^{(h)} = 16 C_{2}(H) \sum_{X \in SU(2)} d_{X} C_{2}(X) . \tag{198}$$

For Higgs-Higgs scattering one simply inserts X = H, so the hypercharge factor becomes Y_H^4 , with $Y_H = 1/2$ and $d_H = 4$ (two isospin components and particle/antiparticle), and for SU(2) one has $C_2(H)^2 = (3/4)^2$. If X is a fermion, replace Y_X^2 or $C_2(X)$ accordingly and include its spin and colour degeneracies in d_X .

As a concrete benchmark, keeping only X=H (and H^{\dagger}) in the plasma sums above yields the simple estimate

$$D_h \simeq \frac{14}{T},\tag{199}$$

obtained by inserting the Higgs quantum numbers and degeneracy into Eqs. (196)–(198) together with the bosonic slow–log points quoted above. Adding the abundant light fermions (and gauge bosons) in the thermal bath increase the total transport rate $\Gamma_t^{(h)}$ and correspondingly reduces D_h .

D Yukawa-mediated relaxation rates: $\hat{\Gamma}_y$

In this appendix we derive, from first principles and in a self-contained way, the leading-log expressions for the per-particle relaxation rates induced by Yukawa interactions in a hot plasma. We keep all phase–space and group/Yukawa factors explicit and regulate the forward (t-channel) singularity with thermal masses. The notation and normalisations (distribution functions, measures, and the overall $12/T^3$ factor converting volume rates to per-particle rates) follow the conventions already fixed in the previous section; we do not repeat them here.

The rate per particle per unit time can be defined as

$$\widehat{\Gamma} = \frac{12}{T^3} \int_{\{p,p',k,k'\}} f_p \widetilde{f}_k (1 + \widetilde{f}_{p'}) (1 - f_{k'}) \delta^4(p + k - p' - k') |\mathcal{M}|^2 , \qquad (200)$$

where f_p and \tilde{f}_k and the distribution functions for the ingoing fermion and boson, while $(1 + \tilde{f}_{p'})$ and $(1 - f_{k'})$ are the spin blocking for the outgoing particles.

The chirality–changing (or flavour–relaxing) $2 \to 2$ reactions driven by a Yukawa coupling y_{ψ} are dominated, at weak coupling, by near–forward t–channel exchange of a gauge boson $X \in \{B, W, g\}$ in the thermal bath:

$$\psi + X \longleftrightarrow \psi' + \phi$$

where ϕ is the Higgs doublet and ψ, ψ' the appropriate chiral components. After spin/colour sums, the squared matrix element has the universal small–angle form

$$|\mathcal{M}_X|^2 = \frac{A_X y_\psi^2 s(-t)}{(t - M^2)^2}, \qquad A_X \equiv c_X (4\pi\alpha_X),$$
 (201)

with $s = (p + k)^2$, $t = (p - p')^2$, α_X the gauge fine–structure constant, and M an asymptotic thermal mass acting as an IR regulator listed earlier. The channel–dependent coefficients c_X encode group

³³The "slow-log" replacement assumes that the weight $w_m(x) = x^m \left(-f_0'(x) \right)$ is sharply peaked at some scale x_* , so a slowly varying factor g(x) can be evaluated at x_* and factored out. For fermions, w_m is well peaked already at small m, but for bosons the IR behaviour $-f_B'(x) \sim x^{-2}$ pushes weight toward small x. As a result, the integrand has no interior maximum for m=2, and for m=3,4 the peak is broad. Only for $m\gtrsim 5$ does the approximation become parametrically good. In practice, one may (i) introduce a physical IR regulator (thermal mass) or (ii) define $\bar{x}_m^{(B)}$ by matching the exact integral to the slow-log ansatz; we follow (ii) here just for the case of $\bar{x}_2^{(B)}$.

theory and bath-species sums; a convenient and widely-used choice is³⁴

$$c_B = 4Y_{\psi}^2, \qquad c_W = 6, \qquad c_g = \frac{32}{3},$$
 (202)

so that $A_B = 16\pi\alpha_w \tan^2\theta_W Y_{\psi}^2$, $A_W = 24\pi\alpha_w$, and $A_g = \frac{128}{3}\pi\alpha_s$. Now, ignoring the spin blocking terms, where this amounts to overestimating the rate by a factor 1-4, we arrive at

$$\widehat{\Gamma} = \frac{12}{T^3} \int_{\{p,k\}} f_p \widetilde{f}_k \mathcal{J},\tag{203}$$

$$\mathcal{J} = \int_{\{p',k'\}} \delta^4(p+k-p'-k') A_X y_{\psi}^2 \frac{-ts}{(t-M^2)^2} = \frac{A_X y_{\psi}^2}{8\pi} \mathcal{I}\left(\frac{M^2}{4pk}\right) , \qquad (204)$$

where $\mathcal{I}(a)$ has already been defined in Eq. (184). In order to perform the integral over p and k we use the following relations

$$\eta_m(n) = \int dx x^m e^{-nx} \ln x = \frac{m!}{n^{m+1}} [H_m - \gamma_E - \ln n], \qquad (205)$$

$$\int dx x^m f_x \ln \frac{1}{x} \approx \ln \frac{1}{x_{m+1}} \int dx x^m f_x , \qquad (206)$$

where $H_m = \sum_{\ell=1}^m \frac{1}{\ell}$ is the harmonic m-number. The integral expressed in the full form is

$$\widehat{\Gamma} = \frac{3Ay_{\psi}^2 T}{32\pi^5} \int_0^{\infty} dx \frac{x}{e^x + 1} \frac{x}{E_p/T} \int_0^{\infty} dy \frac{y}{e^y + 1} \frac{y}{E_k/T} \left[\ln\left(1 + \lambda xy\right) - 1 + \frac{1}{1 + \lambda xy} \right] , \qquad (207)$$

where $\lambda = 4T^2/M^2$, x = p/T and y = k/T. Looking for LL contributions, we are considering the limit $\lambda \gg 1$. We explicitly wrote the energy appearing in the normalisation of the integral so that for massless particles E = p and a different power of x or y appears. In order to reproduce the result in [29] (their App. D), one needs to consider the fermion to be massless and the boson to be massive³⁵. In order to fully perform the integral it is useful to introduce the following quantities

$$J_m^{(F)} = \int_0^\infty dx \, \frac{x^m}{e^x + 1} = (1 - 2^{-m}) \, \Gamma(m+1) \zeta(m+1), \quad J_m^{(B)} = \int_0^\infty dx \, \frac{x^m}{e^x - 1} = \Gamma(m+1) \zeta(m+1), \quad (208)$$

$$\mathcal{M}_X \sim y_{\psi} g_X \frac{1}{t - M^2} \left[\bar{u}(p') \Gamma_Y u(p) \right] \left[\varepsilon_{\mu}^{a}(k) J_a^{\mu} \right],$$

where: y_{ψ} is the Yukawa coupling; g_X is the gauge coupling ($g_Y \equiv g'$ for B, g for W, g_s for g); $t \equiv (p-p')^2$ is the momentum transfer; M is the (asymptotic/screening) thermal mass of the exchanged gauge boson regulating the IR; u, \bar{u} are Dirac spinors; Γ_Y denotes the chiral Yukawa vertex (projector $P_{L/R}$ as appropriate); $\varepsilon_{\mu}^a(k)$ is the polarisation vector of the external bath gauge boson with adjoint index a; and $J_a^{\mu} \equiv \bar{u}(p) \gamma^{\mu} T_R^a u(p)$ is the gauge current of the fermion in representation R (T_R^a are the generators, with tr $T_R^a T_R^b = \frac{1}{2} \delta^{ab}$). After summing/averaging over spins and polarisations and using the small-angle limit $|t| \ll s$ with $s \equiv (p+k)^2$, one obtains the universal kernel

$$\sum_{\text{spins, pols}} \left| \mathcal{M}_X \right|^2 = y_{\psi}^2 g_X^2 \frac{s(-t)}{(t - M^2)^2} \underbrace{\left[8 C_2(R) \right]}_{\text{spin/pol kernel x group}},$$

with $C_2(R)$ the quadratic Casimir of ψ under the exchanged gauge group $(C_2(F)_{SU(2)} = \frac{3}{4}, C_2(F)_{SU(3)} = \frac{4}{3}$; for $U(1)_Y$, replace $T^a \to Y_{\psi}$ so $C_2 \to Y_{\psi}^2$). For the Abelian case, there is an extra factor 1/2 from the initial-state polarisation average not compensated by adjoint sums, yielding

$$c_W = 8 C_2(F)_{SU(2)} = 8 \times \frac{3}{4} = 6,$$
 $c_g = 8 C_2(F)_{SU(3)} = 8 \times \frac{4}{3} = \frac{32}{3},$ $c_B = \frac{8}{2} Y_{\psi}^2 = 4 Y_{\psi}^2.$

³⁴At weak coupling, the chirality–changing $2 \to 2$ process is dominated by near-forward t–channel exchange of a bath gauge boson $X \in \{B, W, g\}$: $\psi(p) + X(k) \to \psi'(p') + \phi(q)$. The tree amplitude with one Yukawa and one gauge vertex can be written schematically as

³⁵In the leading-log approximation, the dominant infrared divergence is regulated by the mass of the exchanged boson, not the fermion. Thus, treating the fermion as massless while keeping the boson massive is sufficient and captures the main effect. Other approaches, see [31] include small fermion masses, but this only adds subleading corrections.

$$L_m^{(F)} = \int_0^\infty dx \, \frac{x^m \ln x}{e^x + 1} = \sum_{n=1}^\infty (-1)^{m+1} \eta_m(n), \qquad L_m^{(B)} = \int_0^\infty dx \, \frac{x^m \ln x}{e^x - 1} = \sum_{n=1}^\infty \eta_m(n) \qquad (209)$$

So in the end writing $\ln(1 + \lambda xy) \approx \ln \lambda xy$ and forgetting about the last term in the $\mathcal{I}(a)$ function the final result is

$$\widehat{\Gamma} \approx \frac{3Ay_{\psi}^2 T}{32\pi^5} \left[\left(\ln(\lambda x_2) - 1 \right) J_2^{(B)} J_1^{(F)} + J_1^{(F)} L_2^{(B)} \right] , \qquad (210)$$

$$= \frac{\zeta(3)Ay_{\psi}^2}{64\pi^3}T\left[\ln\left(\frac{4x_2T^2}{M^2}\right) - 1 + \frac{1}{2\zeta(3)}\sum_{n=1}^{\infty}\eta_2(n)\right].$$
 (211)

In order to see if the LL approximation makes sense, we need to compare the last two terms in the bracket with the LL containing the thermal masses for the fermions appearing in the diagrams. For a relativistic chiral fermion ψ in a hot gauge plasma, the one-loop HTL self-energy gives the asymptotic (large-momentum) thermal mass

$$m_{\psi}^{2} = \frac{T^{2}}{8} \left[\sum_{a \in \{SU(3)_{c}, SU(2)_{L}\}} g_{a}^{2} C_{2}^{(a)}(\psi) + g'^{2} Y_{\psi}^{2} \right]. \tag{212}$$

Here $C_2^{(a)}(\psi)$ is the quadratic Casimir of the representation of ψ under the gauge group a:

$$C_F(SU(3)) = \frac{4}{3}, \qquad C_F(SU(2)) = \frac{3}{4},$$

and Y is the hypercharge in the convention $Q = T_3 + Y$. Writing $g_a^2 = 4\pi\alpha_a$ and $g'^2 = 4\pi\alpha_w \tan^2\theta_W$, one finds for each SM chiral multiplet the chirality-resolved HTL (asymptotic) thermal masses are

$$M_{q_L}^2 = \frac{2}{3}\pi \,\alpha_s \, T^2 + \frac{3}{8}\pi \,\alpha_w \, T^2 + \frac{1}{72}\pi \,\alpha_w \, \tan^2 \theta_W \, T^2,$$

$$M_{u_R}^2 = \frac{2}{3}\pi \,\alpha_s \, T^2 + \frac{2}{9}\pi \,\alpha_w \, \tan^2 \theta_W \, T^2,$$

$$M_{d_R}^2 = \frac{2}{3}\pi \,\alpha_s \, T^2 + \frac{1}{18}\pi \,\alpha_w \, \tan^2 \theta_W \, T^2,$$

$$M_{\ell_L}^2 = \frac{3}{8}\pi \,\alpha_w \, T^2 + \frac{1}{8}\pi \,\alpha_w \, \tan^2 \theta_W \, T^2,$$

$$M_{\ell_R}^2 = \frac{1}{2}\pi \,\alpha_w \, \tan^2 \theta_W \, T^2.$$

$$(213)$$

Here q_L denotes any left-handed quark doublet, u_R and d_R the right-handed up- and down-type singlets, ℓ_L a left-handed lepton doublet, and ℓ_R a right-handed charged-lepton singlet. These masses enter dispersion relations and the regulation of soft regions in rates where appropriate; in the diffusion constants at leading log, the dominant regulators are the Debye masses of the exchanged gauge bosons above. What we get (using the updated value of the couplings) is

$$M_{q_L} \simeq 0.58T$$
, $M_{u_R} \simeq 0.28T$, $M_{d_R} \simeq 0.27T$, $M_{\ell_L}^2 \simeq 0.21T$, $M_{\ell_R} \simeq 0.12T$, (214)

and so the LL are

$$LL_{q_L} \simeq 3.3$$
, $LL_{u_R} \simeq 4.8$, $LL_{d_R} \simeq 4.9$, $LL_{\ell_L} \simeq 5.4$, $LL_{\ell_R} \simeq 6.4$. (215)

where $LL_i = \ln\left(\frac{4x_2T^2}{M_i^2}\right)$ and these has to be compared with $\frac{1}{2\zeta(3)}\sum_{n=1}^{\infty}\eta_2(n) - 1 \simeq -0.24$. The final answer is

$$\widehat{\Gamma}_{\ell_R} = 2 \,\widehat{\Gamma}_{l_L} = \frac{3\zeta(3)}{8\pi^2} \,\alpha_w \, y_\ell^2 \, T \left[\left(1 + \frac{1}{6} \tan^2 \theta_W \right) L L_{\ell_L} + \frac{2}{3} \tan^2 \theta_W \, L L_{\ell_R} \right],
\simeq 0.32 \alpha_w y_\ell^2 T ,
\widehat{\Gamma}_{q_L} = \frac{2\zeta(3)}{3\pi^2} \,\alpha_s \, y_{q_L}^2 \, T \, L L_{q_L} \simeq 0.27 \alpha_s y_{q_L}^2 T ,
\widehat{\Gamma}_{q_R} = \frac{2\zeta(3)}{3\pi^2} \,\alpha_s \, y_{q_R}^2 \, T \, L L_{q_R} \simeq 0.4 \alpha_s y_{q_R}^2 T .$$
(216)

Colour normalisation. The per–particle rates computed in this subsection are colour–summed: they include the factor N_c and thus correspond to a rate "per particle and per number of colours." In the diffusion network we track one fluid per flavour with colour already averaged, so the rate that must enter the transport equations in (76)-(79) is the colour–averaged one,

$$\widehat{\Gamma}_y = \frac{1}{N_c} \widehat{\Gamma}, \qquad N_c = 3. \tag{217}$$

This is why, in the final line, see (79), where the Higgs is considered, a factor 3 appears: it comes from explicitly summing over the three quark colours in the microscopic calculation. Consistently dividing by N_c removes this degeneracy when inserting $\widehat{\Gamma}_y$ into the fluid system.

D.1 Reconciliation with the literature for $\hat{\Gamma}_y$

There has been long-standing confusion in the literature regarding the Yukawa (mixing) relaxation rate $\hat{\Gamma}_y$. Below, we summarise the logic of the main estimates and place our result in that context, making all assumptions explicit.

Early estimates. The first quantitative estimates were given in Refs. [29, 30]. In those works, the fermion thermal mass appears only as an *infrared regulator* of the forward t-channel singularity in gluon exchange; equivalently, the kinematics are treated with massless external lines, and the collinear region is cut off by introducing the mass in the internal propagator. Reproducing that derivation in our conventions (see Eq. (216)), we emphasised that this choice underlies the numerical size of Γ_y and the logarithmic sensitivity to the regulator.

A subsequent estimate was quoted in [31] (their Eq. (3.18)) with minimal derivational detail. The logic appears to follow the same reasoning as [29, 30], but this time *both* the fermion and the boson are treated as massive throughout the computation. Repeating the calculation in that setup, we obtain

$$\widehat{\Gamma} = \frac{9 A_g y_q^2}{32\pi} \left(\frac{\zeta(3)}{\pi^2}\right)^2 T \left[\ln\left(\frac{4x_2 T^2}{M_q^2}\right) - 1 + \frac{1}{3\zeta(3)^2} \sum_{m=1}^{\infty} (-1)^{m+1} \eta_2(m) \sum_{n=1}^{\infty} \eta_2(n) \right], \tag{218}$$

$$\simeq 12 \alpha_s y_q^2 \left(\frac{\zeta(3)}{\pi^2}\right)^2 T \ln\left(\frac{4x_2 T^2}{M_q^2}\right),\tag{219}$$

where A_g is the standard colour factor as before, y_q is the Yukawa coupling, M_q denotes the mass scale regulating the forward singularity, and x_2 is a numerical constant from the phase–space integral. Matching normalisations to the transport equations used in EWBG, the prefactors imply

$$\hat{\Gamma}_{q_L} \simeq 0.6 \, \alpha_s \, y_{q_L}^2 \, T, \qquad \hat{\Gamma}_{q_R} \simeq 0.87 \, \alpha_s \, y_{q_R}^2 \, T,$$
 (220)

up to the logarithmic factor and mild scheme dependence encoded in x_2 and M_q .

Numerical values used in the literature. The value $\hat{\Gamma}_y = 4.2 \times 10^{-4} \, T$ was first quoted in [44] and subsequently adopted by several phenomenological studies [45–49, 51]. This number was later revised: [50] reported $\hat{\Gamma}_y \simeq 3 \times 10^{-2} \, T$, tracing the discrepancy to an improved treatment and to the separation of channels advocated in [70].

Modern viewpoint and channel decomposition. Following [70], it is useful to decompose

$$\widehat{\Gamma}_y = \widehat{\Gamma}_y^{(3)} + \widehat{\Gamma}_y^{(4)},\tag{221}$$

where $\widehat{\Gamma}_y^{(3)}$ arises from the trilinear interaction $h\,\bar{t}_L t_R$, while $\widehat{\Gamma}_y^{(4)}$ is induced by the gluon–assisted vertex $hg\,\bar{t}_L t_R$. In the kinematic regime relevant for electroweak baryogenesis, the *trilinear* contribution $\widehat{\Gamma}_y^{(3)}$ is strongly suppressed, so that the dominant piece is the *gluon–assisted* channel $\widehat{\Gamma}_y^{(4)}$. This perspective is consistent with the historical derivations [29, 30] and with the finite–temperature transport treatments of [77], as emphasised in [70].

Take-home message. Apparent discrepancies in $\widehat{\Gamma}_y$ across the literature can be traced to: (i) different infrared regulators (and whether it enters only the propagator or the full kinematics); (ii)

Box D.1: Thermal mass vs. Debye mass

Two distinct thermal scales are often called "thermal masses":

• **Debye mass** m_D : static electric screening of longitudinal gauge fields, defined from the longitudinal self-energy in the static soft limit $(k_0 = 0, |\vec{k}| \to 0)$. For SU(N),

$$m_D^2 = \frac{g^2 T^2}{3} \left(C_A + \frac{N_f}{2} \right).$$

Use: as the IR regulator in t-channel exchange when computing leading-log transport/diffusion (e.g. D^{-1}) and small-angle scattering kernels; it appears only inside the logarithm.

• Asymptotic mass m_{∞} : HTL correction to the dispersion of *propagating* hard modes $(k \sim T)$, entering the pole of retarded propagators. For gauge bosons

$$m_{\infty}^2 = \frac{g^2 C_A}{6} T^2 + \frac{g^2 N_f}{12} T^2,$$

and for fermions $m_{\infty,f}^2$ follows from their gauge Casimirs (plus Yukawa terms). *Use:* in quasiparticle energies $\omega = \sqrt{k^2 + m_\infty^2}$ within CTP/kinetic kernels (e.g. $\hat{\Gamma}_M$ for fermions and Higgs), together with thermal widths Γ ; see next section.

In short: m_D regulates static, longitudinal screening in exchanged propagators (inside logs); m_{∞} controls dynamic, transverse/fermionic propagation in the medium and is the relevant mass in relaxation rates used in EWBG.

inclusion or omission of the gluon–assisted 4-point channel and/or the 3-point channel; and (iii) distinct normalisation conventions in the transport equations. Equations (218)-(220) make these dependencies explicit and reconcile older and newer results once the same assumptions are imposed.

Using Eq. (216) together with the colour normalisation in Eq. (217), and inserting the updated numerical inputs, the colour–averaged per–particle t–channel Yukawa rate entering the diffusion network is

$$\widehat{\Gamma}_y^t = \frac{1}{N_c} \widehat{\Gamma}_{q_L}^t \simeq 10^{-2} T, \qquad N_c = 3.$$
 (222)

If one were to consider the approximations in (219) the results is $\hat{\Gamma}_y^t \simeq 2.5 \times 10^{-2} T$.

E Yukawa helicity flipping rate: $\hat{\Gamma}_M$

E.1 Fermionic case for $\hat{\Gamma}_m^q$

The purpose of this section is to follow the steps to derive, in a self-contained way, the expression for the mixing (Yukawa) relaxation rate $\widehat{\Gamma}_M$ that appears in electroweak transport. The derivation follows the real-time Schwinger-Keldysh (CTP) framework and the treatment of Refs. [70, 77], with thermal fermions described by hard-thermal-loop (HTL) quasiparticles. Consider a chiral fermion doublet (ψ_L, ψ_R) coupled to a slowly varying Higgs background, $\mathcal{L} \supset y_f \phi_b(z) \bar{\psi}_L \psi_R + \text{h.c.}$. The object that measures the loss of L-R coherence is the off-diagonal two-point function S_{LR} , whose equation of motion is a Kadanoff-Baym (KB) equation with a collision kernel determined by the imaginary parts of retarded self-energies. After Wigner transformation $S^{<,>}(X,k)$ and gradient expansion around the wall background ("VEV-insertion approximation"), the fermionic quasiparticle poles lie at complex energies $\varepsilon_i = \omega_i - i\Gamma_i$, with $\omega_i(k) = \sqrt{k^2 + m_{i,\text{th}}^2}$ the HTL asymptotic dispersion and Γ_i the single-particle damping rate. Linear response in the off-diagonal density amounts to keeping terms quadratic in the Yukawa insertion and evaluating the collision term with thermal propagators. The collision integral controlling the decay of S_{LR} can be written in CTP notation as

 $C_{LR}(X,k) = \frac{i}{2} \left[\sum_{LL}^{>} S_{LR}^{<} - \sum_{LL}^{<} S_{LR}^{>} - (L \leftrightarrow R) \right]$, and using KMS relations together with the spectral decomposition $S^{<,>} = \mp n_F(\pm k_0) A$ turns all statistical factors into derivatives of the Fermi function. Specifically, one encounters the combination $h(k_0) \equiv e^{k_0/T}/(e^{k_0/T}+1)^2 = -\partial n_F/\partial (k_0/T) = n_F(1-n_F)$, which plays the role of the thermal weight for fluctuations.

Carrying out the k_0 integration by closing the contour in the lower or upper half-plane selects the retarded/advanced poles at $k_0 = \varepsilon_L$ and $k_0 = \varepsilon_R$ (and their conjugates), and the KB commutator structure produces two distinct denominators: a difference $(\varepsilon_R^* - \varepsilon_L)^{-1}$ originating from the retarded-advanced subtraction and an energy sum $(\varepsilon_L + \varepsilon_R)^{-1}$ corresponding to particle-hole mixing. The Dirac trace over chiral projectors yields numerators proportional to $p \cdot p'$ with opposite signs in the two channels; in the isotropic plasma frame and after angular integration, this becomes the pair $(\varepsilon_L \varepsilon_R^* - k^2)$ and $(\varepsilon_L \varepsilon_R + k^2)$. The three-momentum phase space $\int d^3k/(2\pi)^3$ reduces to $(2\pi^2)^{-1} \int_0^\infty k^2 dk$, and summing over the colour of the fermion introduces N_c . Finally, when one matches the kinetic equation to the transport equations written for number densities or chemical potentials, the standard susceptibility of a relativistic fermion gas, $n_f = \chi_f \mu_f$ with $\chi_f = T^2/6$ per chiral degree of freedom, pulls out a universal conversion factor $6/T^2$ in front of the momentum integral. Putting all elements together, one finds

$$\widehat{\Gamma}_{M}^{\pm} = \frac{6}{T^{2}} \frac{N_{c}}{2\pi^{2}T} |f|^{2} \int_{0}^{\infty} \frac{k^{2} dk}{\omega_{L} \omega_{R}} \Im \left[-\frac{h(\varepsilon_{L}) \mp h(\varepsilon_{R}^{*})}{\varepsilon_{R}^{*} - \varepsilon_{L}} \left(\varepsilon_{L} \varepsilon_{R}^{*} - k^{2} \right) + \frac{h(\varepsilon_{L}) \mp h(\varepsilon_{R})}{\varepsilon_{L} + \varepsilon_{R}} \left(\varepsilon_{L} \varepsilon_{R} + k^{2} \right) \right], \tag{223}$$

with $\varepsilon_i = \omega_i - i\Gamma_i$ and $\omega_i = \sqrt{k^2 + m_{i,\text{th}}^2}$ the HTL quasiparticle energies for i = L, R, and $h(x) = e^x/(1+e^x)^2$. The prefactor $|f|^2$ is the squared Yukawa insertion; in the broken phase, one may identify $|f|^2 \to y_f^2 \phi_0^2 \equiv m_f^2$. For equal left– and right–handed thermal parameters $(m_{L,\text{th}} = m_{R,\text{th}})$ and $\Gamma_L = \Gamma_R$ the "+" combination vanishes by symmetry and one defines $\Gamma_M \equiv \Gamma_M^-$. It is convenient to extract the explicit mass dependence by introducing the dimensionless thermal parameters $\mu \equiv m_{\text{th}}/T$ and $\gamma \equiv \Gamma/T$, and to write the rate in the compact form

$$\widehat{\Gamma}_{M} = C(\mu, \gamma) \frac{m_{f}^{2}}{T},$$

$$C(\mu, \gamma) = \frac{6}{T^{2}} \frac{N_{c}}{2\pi^{2}T} \int_{0}^{\infty} \frac{k^{2} dk}{\omega_{L} \omega_{R}} \Im \left[-\frac{h(\varepsilon_{L}) + h(\varepsilon_{R}^{*})}{\varepsilon_{R}^{*} - \varepsilon_{L}} \left(\varepsilon_{L} \varepsilon_{R}^{*} - k^{2} \right) + \frac{h(\varepsilon_{L}) + h(\varepsilon_{R})}{\varepsilon_{L} + \varepsilon_{R}} \left(\varepsilon_{L} \varepsilon_{R} + k^{2} \right) \right],$$
(224)

where, in the last line, the minus-channel appropriate for equal L/R quasiparticles has been used. This is the master formula used in [70] and the earlier kinetic derivations summarised in [77].

Fermionic thermal rates (single–particle damping widths) are obtained from the imaginary part of the retarded self–energy evaluated on shell. At leading order and for light quasiparticles the dominant contribution arises from gauge scatterings with soft momentum exchange, yielding a width that is linear in the temperature and quadratic in the gauge coupling. A compact and practically accurate representation is

$$\Gamma_f \simeq \sum_{i \in \{SU(3), SU(2), U(1)_Y\}} a_i \frac{g_i^2 C_i(R_f)}{4\pi} T + \mathcal{O}(y_f^2 T),$$
(225)

where $C_i(R_f)$ is the quadratic Casimir (for $U(1)_Y$, replace $C_1 \to Y_f^2$), the $a_i = \mathcal{O}(1)$ coefficients encode the mild dependence on kinematics and on the precise HTL scheme, and the Yukawa piece is numerically negligible for all SM fermions except the top. This summary follows the detailed analysis of Ref. [78], which also discusses the variants for fermions at rest versus moving, the role of collinear logarithms in abelian sectors, and the modest differences between particle and plasmino branches. For phenomenology near the electroweak scale, one may evaluate Eq. (225) with $g_s \simeq 1.2$, $g \simeq 0.65$, $g' \simeq 0.36$, and use the asymptotic (HTL) masses for the dispersion. Summing the appropriate gauge contributions gives

$$\Gamma_{\text{quark}} \simeq \frac{g_s^2 C_F}{4\pi} T \approx 0.16 T,$$
(226)

$$\Gamma_{\ell_L} \simeq \left[\frac{3 g^2}{16\pi} + \frac{Y_L^2 g'^2}{4\pi} \right] T \approx 0.028 T,$$
(227)

$$\Gamma_{\ell_R} \simeq \frac{Y_R^2 g'^2}{4\pi} T \approx 0.01 T.$$
 (228)

The quark width is dominated by QCD with $C_F = 4/3$, while leptons are set by electroweak exchange. These widths enter the mixing rate Γ_M through the complex poles $\varepsilon = \omega - i\Gamma$ in the kinetic integral and, when expressed as $\gamma \equiv \Gamma/T$, provide the sole dynamical input alongside the HTL masses $m_{\rm th}$ in the dimensionless coefficient $C(\mu, \gamma)$. With these inputs, the integral yields

$$C_t \equiv C(N_c = 3, \ \mu_t = 0.591, \ \gamma = 0.157) = 0.777, \quad \Rightarrow \quad \widehat{\Gamma}_M^t \simeq 0.78 \frac{m_t^2}{T}$$
 (229)

$$C_{\tau_L} \equiv C(N_c = 1, \ \mu_{\tau_L} = 0.210, \ \gamma = 0.028) = 0.213, \quad \Rightarrow \quad \widehat{\Gamma}_M^{\tau_L} \simeq 0.21 \frac{m_{\tau}^2}{T}$$
 (230)

$$C_{\tau_R} \equiv C(N_c = 1, \ \mu_{\tau_R} = 0.126, \ \gamma = 0.010) = 0.220, \quad \Rightarrow \quad \hat{\Gamma}_M^{\tau_R} \simeq 0.22 \frac{m_{\tau}^2}{T}$$
 (231)

E.2 Reconciliation with the literature for $\hat{\Gamma}_M$

Early discussions treated the mixing (Yukawa) relaxation rate in a parametric, order-of-magnitude fashion. In [79], a schematic estimate of the form $\Gamma_M \sim y_t^2 \langle \phi(z)^2 \rangle / T$ was advocated, capturing the intuition that the damping of L-R coherence scales quadratically with the background Higgs field. A more concrete numerical estimate appeared in [31], where one finds $\Gamma_M = y_t^2 T/21$ under simplifying assumptions (massless kinematics, leading-order scatterings, and a single effective relaxation channel). In subsequent phenomenology this was commonly recast as

$$\widehat{\Gamma}_M = \frac{m_t(z, T)^2}{63 T}, \qquad (232)$$

which follows from substituting $m_t = y_t \phi$ and dividing the [31] coefficient by the number of QCD colours, $N_c = 3$, to match transport conventions that normalise the rate per colour/flavour channel. This normalisation, or closely related variants, was then adopted widely in electroweak baryogenesis studies [44–49, 51].

A more systematic derivation based on the real-time kinetic (Schwinger-Keldysh) framework, with HTL quasiparticles and an explicit collision kernel, was presented in [77] and refined in [70] (and summarised in [50]). In this approach, the rate arises from the imaginary part of the retarded self-energy controlling the decay of the off-diagonal correlator S_{LR} in a slowly varying Higgs background. Matching to transport normalisations yields to eq. (224). We have recomputed the integral numerically and obtained the values reported in Eq. (231). In particular, for the top quark we find $C_t \simeq 0.76$, corresponding to $\hat{\Gamma}_m^t \simeq 0.76 \, m_t^2/T$, which is parametrically consistent with the earlier $m_t^2/63 \, T$ estimate but quantitatively larger once realistic thermal masses and widths are used (see also [50]).

Using Eq. (224) together with the colour normalisation in Eq. (217), and inserting the updated numerical inputs, the colour–averaged per–particle rates entering the diffusion network is

$$\hat{\Gamma}_m^t = \frac{1}{N_c} \hat{\Gamma}_M^{t_L} \simeq 0.26 \frac{m_t^2}{T}, \qquad N_c = 3.$$
 (233)

E.3 Bosonic case for $\widehat{\Gamma}_{M}^{(h)}$

In addition to the fermionic channels, an important source of CP-conserving relaxation in the diffusion network arises from the Higgs (scalar) mode itself, whose coherence is damped by interactions with thermal gauge bosons. The computation parallels the fermionic case of Sec. E, but with Bose statistics in the loop and gauge-boson quasi-particles. In the real-time Schwinger-Keldysh formalism, the

relevant object is the imaginary part of the retarded Higgs self–energy induced by a W loop in the plasma. The thermal weight is

$$h_B(x) = \frac{e^x}{(e^x - 1)^2} = -\frac{\partial n_B(x)}{\partial x}, \qquad n_B(x) = \frac{1}{e^x - 1},$$

and the propagating degrees of freedom in the symmetric phase are the two transverse polarisations of W^{\pm} , each described by poles at

$$\varepsilon_T(k) = \omega_T(k) - i \Gamma_W, \qquad \omega_T(k) = \sqrt{k^2 + m_{\infty,W}^2},$$

with $m_{\infty,W}$ the asymptotic (HTL) mass of a hard SU(2) gauge boson and Γ_W its damping width. The loop carries an overall multiplicity $\mathcal{N}_{\text{pol}} = 4$ (two polarisations, two charge states). The Higgs background enters only through the local mass insertion

$$m_W^2(z) = \frac{g^2 \phi(z)^2}{4},$$

which factors out of the momentum integral. Collecting these ingredients, the mixing rate can be written as

$$\widehat{\Gamma}_M^{(h)} = C_h(\mu_T, \gamma_W) \frac{m_W^2}{T}, \qquad (234)$$

where $\mu_T \equiv m_{\infty,W}/T$, $\gamma_W \equiv \Gamma_W/T$, and the dimensionless coefficient is

$$C_h(\mu_T, \gamma_W) = \frac{6}{T^2} \frac{\mathcal{N}_{\text{pol}}}{2\pi^2 T} \int_0^\infty \frac{k^2 dk}{\omega_T^2} \Im \left[-\frac{h_B(\varepsilon_T^*) - h_B(\varepsilon_T)}{\varepsilon_T^* - \varepsilon_T} \left(\varepsilon_T \varepsilon_T^* + k^2 \right) + \frac{h_B(\varepsilon_T) - h_B(-\varepsilon_T)}{\varepsilon_T + \varepsilon_T} \left(\varepsilon_T^2 - k^2 \right) \right], \tag{235}$$

with $\varepsilon_T = \omega_T - i\Gamma_W$. Equation (235) is the bosonic analogue of the fermionic master formula (224); once μ_T and γ_W are specified, C_h is a pure number.

For hard transverse gauge bosons, the damping rate admits the simple parametric estimate

$$\frac{\Gamma_W}{T} \simeq \frac{g^2 C_A}{4\pi}, \qquad C_A = 2 \text{ for } SU(2)_L, \quad g \simeq 0.65 \quad \Rightarrow \quad \gamma_W \approx 0.07.$$
 (236)

This small value ($\gamma_W \ll 1$) justifies the narrow-width approximation below.

When $\gamma_W \ll 1$, the imaginary parts in (235) are dominated by the vicinity of the quasi-particle poles. One can therefore evaluate the k-integral in the NWA, replacing the Breit-Wigner structures by their delta-function limits and evaluating the smooth numerators at the on-shell energy $\omega_T(k)$. In our normalisation, this gives

$$C_h^{\text{NWA}}(\mu_T) = \frac{\mathcal{N}_{\text{pol}} 6}{2\pi^2} \int_0^\infty \frac{k^2 dk}{\omega_T^2} \mathcal{K}_B\left(\frac{\omega_T}{T}\right) = \frac{12}{\pi^2} \mathcal{I}_B(\mu_T), \qquad (237)$$

where \mathcal{K}_B is the resulting bosonic kernel (constructed from h_B and on–shell kinematics) that reads

$$K_B(x) = x h_B(x) = x \frac{e^x}{(e^x - 1)^2} = x n_B(x) (1 + n_B(x)), \qquad x \equiv \frac{\omega_T}{T}.$$

and $\mathcal{I}_B(\mu_T)$ is a dimensionless integral that depends only on the mass ratio $\mu_T = m_{\infty,W}/T$. For a the value $\mu_T \simeq 0.596$ and $\mathcal{N}_{\text{pol}} = 4$, one finds numerically

$$C_h^{
m NWA} \simeq 1.53$$
 . (238)

Inserting (238) into (234) yields

$$\widehat{\Gamma}_m^h \equiv \widehat{\Gamma}_M^{(h)} \simeq 1.5 \, \frac{m_W^2}{T} \,, \tag{239}$$

which is much larger than the commonly quoted parametrisation $\widehat{\Gamma}_M^{(h)} = m_W^2/(50\,T)$. The difference stems from (i) using an explicit HTL width $\gamma_W \simeq 0.07$ and (ii) evaluating the bosonic integral in the narrow-width limit, where the on-shell contribution is enhanced and the dimensionless coefficient is $\mathcal{O}(1)$ rather than at the few-percent level. This result makes transparent the scaling $\widehat{\Gamma}_M^{(h)} \propto m_W^2/T$ while capturing the correct bosonic thermal dynamics encoded in C_h .

F Weak and Strong Sphaleron rates

Sphaleron transitions in the weak and strong sectors play a crucial role in the evolution of baryon and chiral charges in the early Universe. In this section we summarise the existing estimates for their rates, highlighting the different conventions adopted in the literature and reconciling them with the expressions used in this work.

Note. It is important to make explicit the different conventions used in the literature when quoting sphaleron rates. In the diffusion convention, one refers to the topological charge diffusion rate per unit volume, which parametrically scales as $\Gamma \sim \kappa \, \alpha^n \, T^4$. In contrast, in the transport convention—used when inserting the rate into Boltzmann or fluid equations—the same symbol is often employed (with some abuse of notation) for a quantity that instead scales as $\Gamma \sim \kappa \, \alpha^n \, T$.

F.1 Reconciliation with the literature for Γ_{ss}

A variety of *conventions* for the strong sphaleron rate appear in the literature, which can obscure direct numerical comparisons. Two definitions are especially common:

1. Topological charge diffusion rate per unit volume (QCD Chern-Simons diffusion):

$$\Gamma_{ss}^{\text{diff}} \equiv \frac{d}{dt} \frac{\langle (N_{\text{CS}}(t) - N_{\text{CS}}(0))^2 \rangle}{V} = \kappa_{ss} \alpha_s^5 T^4, \qquad (240)$$

with κ_{ss} an $\mathcal{O}(10^2)$ coefficient capturing hard/soft matching and nonperturbative dynamics.

2. Transport rate entering EWBG Boltzmann/transport equations:

$$\Gamma_{ss} = c_{ss} \alpha_s^4 T, \qquad (241)$$

where $c_{ss} \sim O(10)$ and where it has been obtained from (240) after dividing by appropriate susceptibilities and colour/flavour factors.³⁶

Historical estimates and conventions. One of the earliest quantitative determinations is due to Moore [80], who quoted the diffusion form

$$\Gamma_{ss} \simeq 108 \,\alpha_s^5 \, T^4 \,. \tag{242}$$

This is of the form (240) with $\kappa_{ss} \simeq 108$. In subsequent phenomenology, a numeric value $\Gamma_{ss} = 4.9 \times 10^{-4} T$ was often adopted [44–46, 48], reflecting a particular choice of coupling and convention. Independently, Huet & Nelson [31] presented an estimate,

$$\Gamma_{ss} \simeq 16 \,\kappa' \,\alpha_s^4 \,T \,, \tag{243}$$

where κ' encodes additional normalisation choices. A refined transport–rate estimate due to Moore [81] gave

$$\Gamma_{ss} \simeq 14 \,\alpha_s^4 T \,, \tag{244}$$

which is the benchmark subsequently emphasised in several modern summaries [50, 51, 70]. (We note that some phenomenological works quoted fixed numbers such as $\Gamma_{ss} \simeq 8.7 \times 10^{-3} \, T$ in [50] or $2.7 \times 10^{-4} \, T$ in [51].)

Numerical benchmark at the electroweak scale. Adopting the transport form (244) and using the updated coupling at the electroweak scale, $\alpha_s(m_Z) \simeq 0.118$ one obtains

$$\Gamma_{ss} \simeq 14 \,\alpha_s^4 \, T \simeq 2.7 \times 10^{-3} \, T \,.$$
 (245)

³⁶The precise mapping between κ_{ss} and c_{ss} depends on N_c , N_f , and the definition of axial charge density used in the transport system. This is one source of differing normalisations across papers.

Nonperturbative input and extrapolation. A more recent lattice determination of the QCD sphaleron diffusion rate with $N_f = 2+1$ at the physical point was reported by Bonanno et al. [82] for temperatures up to ~ 570 MeV. Their continuum–extrapolated results at those temperatures correspond to Γ_{diff}/T^4 of order 10^{-1} near a few T_c , decreasing with T. While a first–principles determination at $T \sim 100$ GeV is not yet available, a perturbative extrapolation guided by the expected $\alpha_s^5 T^4$ scaling (with the running coupling) leads to a value at the electroweak scale compatible with the transport benchmark (245), i.e. an overall $\mathcal{O}(10^{-3})$ coefficient in front of the appropriate T-scaling. As emphasised above, differences of a factor $\mathcal{O}(1)$ between quoted numbers in the literature mostly reflect distinct conventions, choices for α_s and its scale, and normalisation in the mapping to axial–charge relaxation in transport equations.

F.2 Reconciliation with the literature for Γ_{ws}

As for the strong case, multiple *conventions* coexist for the weak (electroweak) sphaleron rate, which complicates direct numerical comparisons. The **diffusion** (per unit volume) rate of baryon+lepton number violation in the symmetric phase is

$$\Gamma_{ws}^{\text{diff}} = \kappa_{ws} \, \alpha_w^5 \, T^4 \,. \tag{246}$$

Historical estimates. Huet & Nelson [15] provided one of the first parametric forms, $\Gamma_{ws} \sim 6 \kappa \alpha_w^4 T^4$, with $\kappa = \mathcal{O}(1)$. A refined determination by Moore and collaborators [83, 84] established the now-standard α_w^5 scaling with a calibrated coefficient, widely adopted in subsequent works [44–49] with the numerical value of $\Gamma_{ws} = 10^{-6} T$. Modern summaries [70, 77] present a slightly different convention, writing $\Gamma_{ws} = 6\kappa \alpha_w^5 T^4$, while [50], even though quoting [84], they use the numerical value $\Gamma_{ws} = 6.3 \times 10^{-6} T$.

State-of-the-art result. The most precise nonperturbative determination across the electroweak crossover (for the physical Higgs mass) is due to D'Onofrio, Rummukainen and Tranberg [85] and used in subsequent phenomenological applications (see, e.g., [51]). In the *symmetric* phase, they find

$$\Gamma_{ws} = (18 \pm 3) \,\alpha_w^5 \, T \simeq 8 \times 10^{-7} \, T$$
, (247)

where at the electroweak scale we have $\alpha_w \equiv g^2/(4\pi) \simeq 0.0338$.

G Numerical Implementation of the Fluid Equations

In this section, we detail how Lagrange multipliers are implemented when solving the diffusion network in (52) and in its compact representation (131). We introduce one multiplier per constraint (e.g., asymptotic boundary conditions, charge—neutrality, and matching conditions across the wall), couple them linearly to the state vector so that the constraints are enforced exactly at the continuous level, and augment the first—order system with algebraic equations for the multipliers.

The fluid equations constitute a boundary value problem (BVP), as the perturbations are required to vanish far from the bubble wall. Specifically, the boundary conditions are

$$\mu_i(\pm \infty) = 0, \quad v_i(\pm \infty) = 0. \tag{248}$$

To handle this numerically, the differential equations are integrated over a finite interval $z \in [-\tilde{z}_{\max}L_w, \tilde{z}_{\max}L_w]$, where $\tilde{z}_{\max} = 10^4$, ensuring sufficient coverage of the physical domain. The fluid equation network involves solving a system of N_{PERT} equations for each species tracked, encompassing $2N_{\text{PERT}}$ boundary conditions for each species. To ensure the numerical stability of solutions and to enforce these boundary conditions, Lagrange multipliers are introduced.

G.1 The role of Lagrange Multipliers

Lagrange multipliers are a powerful tool for incorporating constraints into optimisation or boundary value problems. Consider a functional

$$S[\varphi] = \int_{\Omega} L(\varphi, \nabla \varphi) \, d\Omega, \tag{249}$$

subject to a boundary condition $\varphi(x) = \varphi_0(x)$ on the boundary $\partial\Omega$. To enforce this constraint, we introduce a Lagrange multiplier function $\lambda(x)$ and modify the functional:

$$S'[\varphi,\lambda] = \int_{\Omega} L(\varphi,\nabla\varphi) \,d\Omega + \int_{\partial\Omega} \lambda(x)(\varphi(x) - \varphi_0(x)) \,dx. \tag{250}$$

The Lagrange multiplier $\lambda(x)$ ensures that the constraint $\varphi(x) = \varphi_0(x)$ is satisfied when $S'[\varphi, \lambda]$ is extremised with respect to both φ and λ .

The nature of the boundary conditions depends on the specific problem:

- Dirichlet boundary conditions: Specify the value of the function φ on the boundary.
- Neumann boundary conditions: Specify the derivative of the function φ on the boundary.
- Mixed boundary conditions: Combine Dirichlet and Neumann conditions.

For example, Dirichlet boundary conditions of the form

$$\varphi(a) = \alpha, \quad \varphi(b) = \beta$$
 (251)

can be enforced by adding terms to the functional

$$\lambda_1(\varphi(a) - \alpha) + \lambda_2(\varphi(b) - \beta). \tag{252}$$

The resulting variational equations ensure the constraints are satisfied. For the fluid equations, we impose the boundary conditions

$$\mu^{a}(\pm \tilde{z}_{\max} L_{w}) = 0, \quad u^{a}_{\ell}(\pm \tilde{z}_{\max} L_{w}) = 0. \tag{253}$$

To incorporate the boundary conditions numerically, we add Lagrange multiplier terms to the equations

$$\partial_{\tilde{z}}\tilde{\mu}_i = \dots + \lambda_{\mu_i}(\tilde{z} + N\tilde{L}_w), \tag{254}$$

$$\partial_{\tilde{z}} v_i = \dots + \lambda_{v_i} (\tilde{z} - N \tilde{L}_w), \tag{255}$$

$$\partial_{\tilde{z}}\lambda_{u_i} = 0, \tag{256}$$

$$\partial_{\tilde{z}}\lambda_{v_i} = 0, \tag{257}$$

where $\tilde{x} = x/T$. Here, the negative sign in Eq. (255) has been introduced for numerical stability.

Introducing Lagrange multipliers ensures the numerical stability of the solution and satisfies all boundary conditions simultaneously. The computed solutions for the perturbations, subject to these conditions, are illustrated in Fig. 3. These solutions demonstrate the effectiveness of the chosen boundary conditions and numerical implementation in capturing the dynamics of the fluid equations in the presence of a bubble wall.

H Chemical vs. kinetic equilibrium

In transport and cosmological systems, as emphasized in [86], two distinct notions of equilibrium must be distinguished: chemical equilibrium, which governs number densities, and kinetic equilibrium, which governs the momentum shapes of the distributions. Each species i is described by a phase–space density $f_i(p, z)$ with moments such as number and energy densities. The two types of equilibration involve different microscopic processes and can occur on different timescales.

Chemical equilibrium. Consider a reaction network $\sum_{j} \nu_{aj} X_{j} \leftrightarrow 0$. Chemical equilibrium enforces $\sum_{j} \nu_{aj} \mu_{j} = 0$ for each active process a. Let Γ_{chem} denote the slowest number–changing rate controlling abundances—for example, from annihilations, decays, or $3 \rightarrow 2$ reactions. Equilibrium holds when

$$\Gamma_{\text{chem}} \gg \tau_{\text{wall}}^{-1}, \qquad \tau_{\text{wall}} \equiv \frac{L_w}{\gamma_w v_w},$$
(258)

where L_w is the wall thickness and $\gamma_w v_w/L_w$ the relevant macroscopic rate. When this is satisfied, the corresponding relations among the chemical potentials $\mu_i(z)$ can be imposed rather than solved dynamically. Examples include fast weak interactions tying μ_{t_L} and μ_{b_L} , or strong sphalerons enforcing relations among quark chiralities.

Kinetic equilibrium. Kinetic equilibrium requires rapid momentum exchange so that $f_i(p, z)$ retains a thermal shape with local $T_i(z)$ and $\mu_i(z)$. The relevant rate is the momentum–transfer rate

$$\gamma_p \simeq n_t \langle \sigma_{\rm mt} v \rangle \frac{T_t}{m_i}, \qquad \sigma_{\rm mt}(s) = \int d\Omega \left(1 - \cos\theta\right) \frac{d\sigma}{d\Omega},$$
 (259)

for a species *i* scattering elastically on relativistic targets *t*. Kinetic equilibrium holds when $\gamma_p \gg \tau_{\text{wall}}^{-1}$, equivalently when the mean free path $\ell_{\text{mfp}} \sim \langle v \rangle / \gamma_p$ is much shorter than L_w . If this condition is only marginal, high–momentum modes typically depart first, and a single–temperature closure can bias the computation of sources and washout.

H.1 From cosmology to EWBG timescales

In early—universe cosmology, reaction rates are compared to the Hubble parameter H(T). In EWBG, the relevant clock is the wall passage: diffusion and advection compete with reactions across a distance L_w . Thus, "fast" processes in EWBG satisfy

$$\Gamma, \ \gamma_p \gg \tau_{\text{wall}}^{-1} = \frac{\gamma_w v_w}{L_w},$$
 (260)

which determines when chemical relations can be imposed and when a fluid closure is justified.

A particle i should be treated as an independent fluid (with its own μ_i and velocity perturbation) whenever chemical or kinetic equilibration is not fast, or when it appears directly in CP-violating sources that influence η_B . Conversely, if both Γ^i_{chem} and γ^i_p are much larger than τ^{-1}_{wall} , the species can be integrated out using chemical constraints and a local thermal ansatz, reducing the stiffness of the system without loss of accuracy.

"Thermal equilibrium" is often used loosely to mean kinetic equilibrium. Strictly, global thermal equilibrium—uniform temperature and vanishing thermodynamic forces—is not realised across a moving wall. EWBG instead assumes local thermal equilibrium of the bath, with slowly varying T(z) and small departures encoded in $\mu_i(z)$ and fluid velocities. This is valid when elastic scattering is rapid $(\ell_{\rm mfp} \ll L_w)$ and gradients are mild; otherwise, one should include higher moments or solve for $f_i(p,z)$ explicitly.

In practice, one computes Γ_{chem} and γ_p for the relevant processes and compares them to τ_{wall}^{-1} . If both are large, impose chemical relations and assume a single T. If either is marginal, evolve the species explicitly or use a more refined closure (e.g. two-temperature or Fokker-Planck treatment). This provides a consistent criterion for deciding which degrees of freedom belong in the fluid network and which can be thermally integrated out.

References

- [1] A. D. Sakharov *Pisma Zh. Eksp. Teor. Fiz.* 5 (1967) 32–35. [Usp. Fiz. Nauk161,no.5,61(1991)].
- [2] V. Kuzmin, V. Rubakov, and M. Shaposhnikov *Physics Letters B* **155** (1985), no. 1 36–42.

- [3] M. Shaposhnikov JETP Lett. 44 (1986) 465–468.
- [4] M. Shaposhnikov Nuclear Physics B **287** (1987) 757–775.
- [5] A. G. Cohen, D. B. Kaplan, and A. E. Nelson *Physics Letters B* **245** (1990), no. 3 561–564.
- [6] A. G. Cohen, D. B. Kaplan, and A. E. Nelson Ann. Rev. Nucl. Part. Sci. 43 (1993) 27–70, [hep-ph/9302210].
- [7] K. Kajantie, M. Laine, K. Rummukainen, and M. E. Shaposhnikov *Nucl. Phys. B* **466** (1996) 189–258, [hep-lat/9510020].
- [8] K. Kajantie, M. Laine, K. Rummukainen, and M. E. Shaposhnikov *Phys. Rev. Lett.* 77 (1996) 2887–2890, [hep-ph/9605288].
- [9] K. Kajantie, M. Laine, K. Rummukainen, and M. E. Shaposhnikov Nucl. Phys. B 493 (1997) 413–438, [hep-lat/9612006].
- [10] M. Gurtler, E.-M. Ilgenfritz, and A. Schiller Phys. Rev. D 56 (1997) 3888–3895, [hep-lat/9704013].
- [11] F. Csikor, Z. Fodor, and J. Heitger Phys. Rev. Lett. 82 (1999) 21–24, [hep-ph/9809291].
- [12] M. Laine and K. Rummukainen Nucl. Phys. B 535 (1998) 423–457, [hep-lat/9804019].
- [13] Y. Aoki, F. Csikor, Z. Fodor, and A. Ukawa Phys. Rev. D 60 (1999) 013001, [hep-lat/9901021].
- [14] M. B. Gavela, P. Hernandez, J. Orloff, O. Pene, and C. Quimbay Nucl. Phys. B 430 (1994) 382–426, [hep-ph/9406289].
- [15] P. Huet and E. Sather Phys. Rev. D 51 (1995) 379–394, [hep-ph/9404302].
- [16] J. I. Kapusta and C. Gale, Finite-Temperature Field Theory: Principles and Applications, 2nd edition. Cambridge University Press, 2007.
- [17] M. Carena, M. Quiros, and C. E. M. Wagner Phys. Lett. B 380 (1996) 81–91, [hep-ph/9603420].
- [18] M. Carena, M. Quiros, A. Riotto, I. Vilja, and C. E. M. Wagner Nucl. Phys. B 503 (1997) 387–404, [hep-ph/9702409].
- [19] J. M. Cline and G. D. Moore *Phys. Rev. Lett.* **81** (1998) 3315–3318, [hep-ph/9806354].
- [20] S. Profumo, M. J. Ramsey-Musolf, and G. Shaughnessy JHEP 08 (2007) 010, [arXiv:0705.2425].
- [21] S. Bruggisser, B. Von Harling, O. Matsedonskyi, and G. Servant Phys. Rev. Lett. 121 (2018), no. 13 131801, [arXiv:1803.08546].
- [22] S. Bruggisser, T. Konstandin, and G. Servant JCAP 11 (2017) 034, [arXiv:1706.08534].
- [23] L. Kadanoff and G. Baym, Quantum Statistical Mechanics: Green's Function Methods in Equilibrium and Nonequilibrium Problems. Frontiers in Physics: Lecture note and reprint series, A. W.A. Benjamin, 1962.
- [24] J. Schwinger Journal of Mathematical Physics 2 (05, 1961) 407-432, [https://pubs.aip.org/aip/jmp/article-pdf/2/3/407/19046507/407_1_online.pdf].
- [25] L. V. Keldysh Sov. Phys. JETP **20** (1965) 1018–1026.
- [26] T. Prokopec, M. G. Schmidt, and S. Weinstock Annals Phys. 314 (2004) 208–265, [hep-ph/0312110].
- [27] T. Prokopec, M. G. Schmidt, and S. Weinstock Annals Phys. 314 (2004) 267–320, [hep-ph/0406140].

- [28] T. Konstandin, T. Prokopec, M. G. Schmidt, and M. Seco Nucl. Phys. B 738 (2006) 1–22, [hep-ph/0505103].
- [29] M. Joyce, T. Prokopec, and N. Turok Phys. Rev. D 53 (1996) 2930–2957, [hep-ph/9410281].
- [30] M. Joyce, T. Prokopec, and N. Turok Phys. Rev. D 53 (1996) 2958–2980, [hep-ph/9410282].
- [31] P. Huet and A. E. Nelson *Phys. Rev. D* **53** (1996) 4578–4597, [hep-ph/9506477].
- [32] K. Funakubo *Prog. Theor. Phys.* **96** (1996) 475–520, [hep-ph/9608358].
- [33] H. Davoudiasl, K. Rajagopal, and E. Westphal *Nucl. Phys. B* **515** (1998) 384–412, [hep-ph/9707540].
- [34] J. M. Cline, M. Joyce, and K. Kainulainen JHEP 07 (2000) 018, [hep-ph/0006119].
- [35] C. Lee, V. Cirigliano, and M. J. Ramsey-Musolf Phys. Rev. D 71 (2005) 075010, [hep-ph/0412354].
- [36] V. Cirigliano, C. Lee, M. J. Ramsey-Musolf, and S. Tulin *Phys. Rev. D* 81 (2010) 103503, [arXiv:0912.3523].
- [37] V. Cirigliano, C. Lee, and S. Tulin Phys. Rev. D 84 (2011) 056006, [arXiv:1106.0747].
- [38] M. Herranen, K. Kainulainen, and P. M. Rahkila *Nucl. Phys. B* **810** (2009) 389–426, [arXiv:0807.1415].
- [39] M. Herranen, K. Kainulainen, and P. M. Rahkila JHEP 09 (2008) 032, [arXiv:0807.1435].
- [40] M. Herranen, K. Kainulainen, and P. M. Rahkila JHEP 05 (2009) 119, [arXiv:0812.4029].
- [41] M. Herranen, K. Kainulainen, and P. M. Rahkila JHEP 12 (2010) 072, [arXiv:1006.1929].
- [42] C. Balazs, M. Carena, A. Menon, D. E. Morrissey, and C. E. M. Wagner Phys. Rev. D 71 (2005) 075002, [hep-ph/0412264].
- [43] M. Joyce, T. Prokopec, and N. Turok Phys. Rev. Lett. 75 (1995) 1695–1698, [hep-ph/9408339].
 [Erratum: Phys.Rev.Lett. 75, 3375 (1995)].
- [44] D. Bodeker, L. Fromme, S. J. Huber, and M. Seniuch JHEP 02 (2005) 026, [hep-ph/0412366].
- [45] L. Fromme and S. J. Huber JHEP 03 (2007) 049, [hep-ph/0604159].
- [46] L. Fromme, S. J. Huber, and M. Seniuch JHEP 11 (2006) 038, [hep-ph/0605242].
- [47] J. R. Espinosa, B. Gripaios, T. Konstandin, and F. Riva JCAP 01 (2012) 012, [arXiv:1110.2876].
- [48] T. Konstandin Phys. Usp. **56** (2013) 747–771, [arXiv:1302.6713].
- [49] J. M. Cline and K. Kainulainen *Phys. Rev. D* 101 (2020), no. 6 063525, [arXiv:2001.00568].
- [50] J. M. Cline and B. Laurent Phys. Rev. D 104 (2021), no. 8 083507, [arXiv:2108.04249].
- [51] K. Kainulainen and N. Venkatesan JCAP 08 (2024) 058, [arXiv:2407.13639].
- [52] M. Trodden Rev. Mod. Phys. **71** (1999) 1463–1500, [hep-ph/9803479].
- [53] A. Riotto, Theories of baryogenesis, in ICTP Summer School in High-Energy Physics and Cosmology, 7, 1998. hep-ph/9807454.
- [54] A. Riotto and M. Trodden Ann. Rev. Nucl. Part. Sci. 49 (1999) 35-75, [hep-ph/9901362].

- [55] M. Dine and A. Kusenko Rev. Mod. Phys. **76** (2003) 1, [hep-ph/0303065].
- [56] J. M. Cline, Baryogenesis, in Les Houches Summer School Session 86: Particle Physics and Cosmology: The Fabric of Spacetime, 9, 2006. hep-ph/0609145.
- [57] D. E. Morrissey and M. J. Ramsey-Musolf New J. Phys. 14 (2012) 125003, [arXiv:1206.2942].
- [58] G. A. White, A Pedagogical Introduction to Electroweak Baryogenesis. 2053-2571. Morgan & Claypool Publishers, 2016.
- [59] B. Garbrecht Prog. Part. Nucl. Phys. 110 (2020) 103727, [arXiv:1812.02651].
- [60] D. Bodeker and W. Buchmuller arXiv:2009.07294.
- [61] J. van de Vis, J. de Vries, and M. Postma arXiv:2508.09989.
- [62] G. C. Dorsch, S. J. Huber, and T. Konstandin arXiv:2112.12548.
- [63] G. C. Dorsch, T. Konstandin, E. Perboni, and D. A. Pinto JCAP 04 (2025) 033, [arXiv:2412.09266].
- [64] B. Laurent and J. M. Cline Phys. Rev. D 102 (2020), no. 6 063516, [arXiv:2007.10935].
- [65] S. De Curtis, L. D. Rose, A. Guiggiani, A. G. Muyor, and G. Panico arXiv:2201.08220.
- [66] S. De Curtis, L. Delle Rose, A. Guiggiani, A. Gil Muyor, and G. Panico arXiv:2303.05846.
- [67] S. De Curtis, L. Delle Rose, A. Guiggiani, Á. Gil Muyor, and G. Panico JHEP 05 (2024) 009, [arXiv:2401.13522].
- [68] G. 't Hooft Phys. Rev. Lett. 37 (Jul, 1976) 8–11.
- [69] S. shen Chern Annals of Mathematics 47 (1946), no. 1 85–121.
- [70] J. de Vries, M. Postma, J. van de Vis, and G. White JHEP 01 (2018) 089, [arXiv:1710.04061].
- [71] J. De Vries, M. Postma, and J. van de Vis JHEP 04 (2019) 024, [arXiv:1811.11104].
- [72] F. Klinkhamer and N. Manton, A saddle-point solution in the weinberg-salam theory, in The Standard Model Higgs Boson (M. EINHORN, ed.), vol. 8 of Current Physics-Sources and Comments, pp. 245–253. Elsevier, 1991.
- [73] Planck Collaboration, P. A. R. Ade et al. Astron. Astrophys. 594 (2016) A13, [arXiv:1502.01589].
- [74] Y.-Z. Li, M. J. Ramsey-Musolf, and J.-H. Yu arXiv: 2404.19197.
- [75] B. Laurent and J. M. Cline Phys. Rev. D 106 (2022), no. 2 023501, [arXiv:2204.13120].
- [76] J. M. Cline, M. Joyce, and K. Kainulainen hep-ph/0110031.
- [77] V. Cirigliano, M. J. Ramsey-Musolf, S. Tulin, and C. Lee Phys. Rev. D 73 (2006) 115009, [hep-ph/0603058].
- [78] P. Elmfors, K. Enqvist, A. Riotto, and I. Vilja Phys. Lett. B 452 (1999) 279–286, [hep-ph/9809529].
- [79] A. G. Cohen, D. B. Kaplan, and A. E. Nelson *Phys. Lett. B* **336** (1994) 41–47, [hep-ph/9406345].
- [80] G. D. Moore Phys. Lett. B 412 (1997) 359-370, [hep-ph/9705248].
- [81] G. D. Moore and M. Tassler JHEP 02 (2011) 105, [arXiv:1011.1167].

- [82] C. Bonanno, F. D'Angelo, M. D'Elia, L. Maio, and M. Naviglio *Phys. Rev. Lett.* **132** (2024), no. 5 051903, [arXiv:2308.01287].
- [83] G. D. Moore Phys. Rev. D 62 (2000) 085011, [hep-ph/0001216].
- [84] D. Bodeker, G. D. Moore, and K. Rummukainen Phys. Rev. D 61 (2000) 056003, [hep-ph/9907545].
- [85] M. D'Onofrio, K. Rummukainen, and A. Tranberg Phys. Rev. Lett. 113 (2014), no. 14 141602, [arXiv:1404.3565].
- [86] S. Profumo arXiv:2508.20988.